Study of converged 60 GHz radio over fiber with WDM-PON access networks

Tong Shao

UNIVERSITÉ DE GRENOBLE

THÈSE

Pour obtenir le grade de

DOCTEUR DE L'UNIVERSITÉ DE GRENOBLE

Spécialité : **Optique et Radio Fréquence**

Arrêté ministériel :

Présentée par

Tong SHAO

Thèse dirigée par **Béatrice CABON, Ghislaine MAURY** et **Yannis LE GUENNEC**

préparée au sein du **Laboratoire IMEP-LAHC**
dans **l'École Doctorale EEATS**

Study of Converged 60 GHz Radio over Fiber with WDM-PON Access Networks

Thèse soutenue publiquement le **25 Juin 2012**,
devant le jury composé de :

M. Georges ALQUIE
PR Université Pierre et Marie Curie, Président
Mme. Christelle AUPETIT-BERTHELEMOT
PR Université de Limoges, Rapporteur
M. Jean-Pierre VILCOT
DR CNRS, Rapporteur
Mme. Ghislaine MAURY
MCF INP Grenoble, Co-directeur de thèse
M. Yannis LE GUENNEC
MCF INP Grenoble, Co-directeur de thèse
Mme. Béatrice CABON
PR INP Grenoble, Directeur de thèse

Study of Converged 60 GHz Radio over Fiber with WDM-PON Access Networks

by Tong SHAO

Ph.D thesis prepared at IMEP-LAHC Laboratory, INP-Grenoble, France

Supervisor: Béatrice Cabon

Co-Supervisors: Ghislaine Maury and Yannis Le Guennec

Acknowledgment

I appreciate my supervisor Professor Béatrice Cabon and my co-supervisors Dr. Ghislaine Maury and Dr. Yannis Le Guennec for their great help and ongoing support during my Ph.D research and life in France.

I would appreciate the engineer in our lab Mr. Nicolas Carroa for his strong support during the experiments.

I would appreciate Dr. Julien Poette for the helpful discussion during the research.

I would say thanks to my kind colleges in Microwave and Photonics group Ms. Flora Parésys, Mr. Vincent Dobremez, Ms. Friederike Brendel, Mr. Zine Bouhamri, Dr. Hoang Giang Nguyen and Mr. Habeb Rzaigui for their collaborations.

I appreciate Professor Gang Feng for his great help during my Ph.D application.

I am grateful for all my dear friends in France, Dr. Yong Xu, Mr. Pierre Bousseaud, Dr. Ke Li, Mr. Jing Wan, Ms. Yan Fu, Ms. Xiaolan Tang, Ms. Chuan-lun Hsu, Ms. Cuiqin Xu, Mr. Tekfour Lim, Mr. Fanyu Liu, Mr. Tapas Dutta, Mr. Amer Diab, Mr. Léonce Mutwewingabo, Dr. Lin You, Mr. Ji-Hoon Choi, Dr. Hai Yu, Mr. Zuheng Ming, Dr. Wenbin Yang, Mr. Zhongyang Li, Ms. Guanghan Song, Mr. Hao Gong, Mr. Weiyuan Ni, Ms. Longyu Jiang, Dr. Hao Shen and so on.

In the end I appreciate my parents and my wife for their love and encourage over my life.

The over two-year study in the IMEP-LAHC Laboratory with my supervisors is an extremely enjoyable experience for me. Research, experimental discoveries and sparks from creative thinkings make me feel fulfilling and open minded. It is my great pleasure to do my Ph.D research in IMEP-LAHC. I appreciate my supervisors once again and I hope that I will have opportunity to work with them in the future.

Contents

Acronyms

AMP	Amplifier
ASE	Amplified Spontaneous Emission
AWG	Arbitrary Waveform Generator / Array Waveguide Grating
BER	Bit Error Rate
BERT	Bit Error Rate Tester
BPSK	Binary Phase Shift Keying
BS	Base Station
CL	Conversion Loss
CS	Central Station
DEMUX	Demultiplexer
DSB	Double Sideband
DSB-SC	Double Sideband Suppressed Carrier
DSO	Digital Storage Oscilloscope
DFB	Distributed Feedback
EAM	Electro Absorption Modulator
ECMA	European association for standardizing information and communication systems.
EDFA	Erbium Doped Fiber Amplifier
EOM	Electro Optical Modulator
ESA	Electrical Spectrum Analyzer
EVM	Error Vector Magnitude
FBG	Fiber Bragg Grating
FTTH	Fiber-to-the-Home
GMSK	Gaussian Minimum Shift Keying
ISI	Intersymbol Interference
IF	Intermediate Frequency
IL	Insertion Loss
IM	Intensity Modulation
LD	Laser Diode
LPF	Low Pass Filter
LNA	Low Noise Amplifier
MLLD	Mode Locked Laser Diode
mmW	Millimeter Wave
MZM	Mach-Zhender Modulator
OFDM	Orthogonal Frequency Division Multiplexing
OLT	Optical Line Terminal
ONU	Optical Network Unit
OOK	On-Off Keying
PAPR	Peak to Averge Power Ratio
PD	Photodiode

PON	Passive Optical Network
PPG	Pulse Patern Generator
PSG	PSG Vector Generator
QAM	Quadrature Amplitude Modulation
RAN	Remote Access Node
RF	Radio Frequency
RoF	Radio over Fiber
RSOA	Reflected Semiconductor Optical Amplifier
SMF	Single Mode Fiber
SNR	Signal to Noise Ratio
UWB	Ultra Wide Band
VSA	Vector Signal Analyzer
WDM	Wavelength Division Multiplexing

List of figures and tables

List of figures:

List of Tables:

Introduction

Recently, convergence of 60 GHz radio over fiber (RoF) technique with wavelength division multiplexing (WDM) passive optical networks (PON) has raised great interests because it provides the possibility for simultaneous broadband 60 GHz signal generation and multi-gigabit per second wireline transmission. The objective of the thesis is to study the solutions for converged 60 GHz RoF and WDM-PON technique.

The first chapter describes the contexts of WDM-PON and main technologies of RoF: the basic architecture of WDM-PON, different techniques for mmW generation, requirement for the 60 GHz signal transmission, and the current solutions for converged 60 GHz RoF and WDM-PON found in literature. This chapter figures out the issues of WDM-RoF networks to investigate.

The second chapter is focused on the concept of 60 GHz RoF system using WDM demultiplexer. The complete phase noise, which includes the optical phase to intensity noise conversion and the phase noise contribution from the electrical signal source for optical frequency conversion, is theoretically and experimentally investigated. Finally, the optical millimeter wave (mmW) up-conversion of broadband digital signal, which is compliant with the ECMA 387 standard, is experimentally demonstrated.

The third chapter presents our proposed converged RoF technique with WDM-PON, which supports broadband mmW generation and multi-gigabit per second wireline transmission. In order to lower the cost of the infrastructure, the multiband modulation technique with parallel phase modulation by using a single Mach-Zehnder modulator (MZM) is deeply investigated. The comparison of different multiband modulation techniques with a single optical modulator is theoretically inquired. Furthermore, the interference between multi-band modulations with a single MZM is theoretically investigated and experimentally demonstrated.

In the last chapter, a bidirectional RoF system, which is compliant with the WDM-PON requirements, is implemented by using optoelectronic mixing technique for the frequency down-conversion in up-link transmission. The optoelectronic mixing

technique with non-linear p-i-n photodiode for mmW down-conversion is experimentally demonstrated. The down-link scheme uses typical optical heterodyning scheme for mmW generation and the impact of the non-linear PD on down-link performances is investigated in this chapter.

Key words: Radio over Fiber, WDM-PON, ECMA 387, mmW, Multiband modulation.

Chapter 1

State of the art on 60 GHz radio over fiber and WDM-PON

1.1 Introduction

For wireless networks, the millimeter wave (mmW) band has attracted much attention due to the opening of an unlicensed 7 GHz band around 60 GHz in most of the countries, which is comparable with the unlicensed bandwidth allocated for ultra-wideband (UWB) from 3.1 GHz to 10.6 GHz. Compared with the UWB band, the 60 GHz bandwidth is less restricted in terms of emitted power limits due to the fact that propagation loss at 60 GHz is dramatically increased compared with the 10 GHz frequency band. The huge bandwidth around 60 GHz represents great feasibility for multi-gigabit per second wireless communications, which is physically constrained at low frequency because of the scarcity of frequency spectrum. Many indoor applications at 60 GHz band are proposed [1].

(i) cable replacement or uncompressed high definition (HD) video streaming that enables users to wirelessly display content to a remote screen with wired equivalent quality/experience.

(ii) ‘sync and go’ file transfer that enables gigabytes of file transfer in a few seconds.

(iii) wireless docking stations that allow multiple peripherals (including an external monitor) to be connected without the need for frequent plugging and unplugging.

(iv) wireless gigabit Ethernet that permits bidirectional multi-gigabit Ethernet traffic.

(v) wireless gaming that ensures high-quality performance.

Nevertheless, because of the high attenuation of mmW signals during the radio

propagation, many radio base stations (BSs) are required in the 60 GHz network infrastructure. Radio over Fiber (RoF) technology has raised great interest in the last decade to provide optical transmission of radio signals to numerous simplified BS [2]. Another main advantage of RoF technology relies on the possibility to centralize broadband optical signal processing functions such as optical mmW generation, with the objective of limiting the use of expensive broadband electronics in the BSs.

For wireline access networks, fiber to the home (FTTH) technology is being deployed in many countries because of its large bandwidth of the signal transmission compared to ADSL. As it is widely accepted, FTTH is the only future-proof technology that will be able to support the upcoming interactive multimedia services, and nowadays operators are planning to substitute the existing telephone-line-based systems (Asymmetric Digital Subscriber Line ADSL, Plain Old Telephone Service POTS) or cable systems (Cable Television CATV) per optical fibre. Recently, the more advanced point-to-multipoint Passive Optical Networks (PON) are being deployed to implement FTTH in Asia and USA mainly. The first generations of PONs (Broadband PON, Gigabit PON, Ethernet PON) have been recently standardized, offering Gigabit/s bandwidth typically shared among few tens of users. Research activities are focusing on possible extensions of current GPON and EPON since these systems may suffer bandwidth limitations in the future, and they do not make use of the full optical bandwidth. Among the numerous approaches proposed for FTTH, Wavelength Division Multiplexing (WDM) technology straightforwardly offers a new dimension for this upgrade. WDM-PON attracts much attention as the next generation PON, which is required as

(i) High splitting ratio (>64)

(ii) High speed (>1 Gbps)

(iii) Bidirectional transmission, symmetrical data rate, single fibre access

(iv) Long reach (>20 km)

(v) Passive

(vi) Simple upgradeability

(vii) Centralized management

(viii) Dynamic resource allocation

(ix) Basic protection incorporated

The remarkable potentials of the WDM-PON networks and 60 GHz RoF technique are driving the research towards convergence of 60 GHz RoF and WDM-PON very recently, which is the single most important point of this thesis report. All the theoretical and experimental investigations are implemented towards this target.

1.2 Overview of 60 GHz RoF technique

RoF technique is attractive in the application of mmW wireless transmission due to the possibility of the generation of 60 GHz mmW with very low phase noise by optical heterodyning technique. In the downlink transmission, it is possible to centralize the optical signal process and simplify the BSs to lessen the cost of the infrastructure. In the uplink transmission, due to the high cost of optical modulator and receiver in mmW band, it is necessary to implement frequency down-conversion before optical transmission from BS to central station (CS). RoF systems have been actually developed around these two issues in the last decade. The focus of the thesis is on the solution of downlink transmission. In this section, different approaches for mmW generation in the RoF system are emphatically introduced with the comments of the advantages and disadvantages. Moreover, different frequency down-conversion techniques for uplink transmission are subsequently summarized.

1.2.1 Overview of the 60 GHz RoF system

1.2.1.1 mmW frequency band for wireless transmission

60 GHz technology offers various advantages over current or existing communications systems. One major reason for the recent interest in 60 GHz technology is the huge unlicensed bandwidth. As shown in Fig. 1.1 [1], at least 5 GHz of continuous bandwidth is available in many countries worldwide.

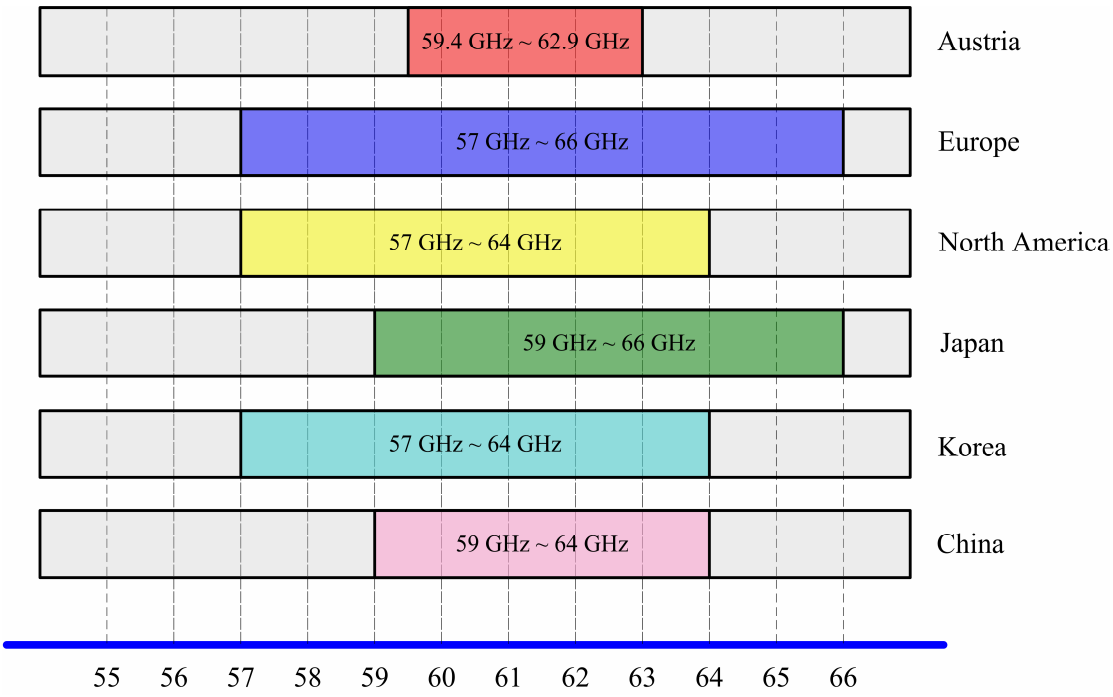

Fig. 1.1. Worldwide unlicensed band allocation for 60GHz band

Higher emitted power is necessary to overcome the higher path loss at 60 GHz compared to the 10 GHz frequency band. While the high path loss seems to be a disadvantage at 60GHz, it confines the 60GHz operation to within a room in an indoor environment. Hence, the effective interference levels and inter symbol interference (ISI) due to the channel fading, for 60GHz are less severe than those systems located in the congested 2.0 GHz to 2.5GHz and 5.0 GHz to 5.8 GHz region.

Interest in 60GHz wireless transmission has motivated the growth of multiple international mmW standardization groups and industry alliances in last few years. In March 2005, the IEEE 802.15.3c [3] Task Group (TG3c) was formed to develop a mmW based alternative physical layer (PHY) for the existing IEEE 802.15.3 WPAN standard 802.15.3-2003. In August 2006, ECMA TC-48 (formerly known as TC32-TG20) began an effort to standardize medium access control (MAC) and PHY for high-speed, short-range communications using the 60 GHz unlicensed frequency band for bulk data applications and for multi media streaming applications. In December, 2008, the first edition of ECMA 387 standard [3] was ratified. In October 2006, the formation of the Wireless HD consortium was announced with a number of key consumer electronics companies to deliver a specification for high-speed,

high-quality uncompressed audio/video (A/V) streaming using 60 GHz technology. In January 2008, the WirelessHD 1.0 specification was released. Unlike the IEEE 802.15.3c, the WirelessHD 1.0 only uses orthogonal frequency division multiplexing (OFDM) modulation with small number of subcarriers. The Wireless Gigabit Alliance (WiGig) was formed in May 2009 to establish a unified specification for 60 GHz wireless technology in order to create a truly global ecosystem of interoperable products for a diverse range of applications. The WGA specification [4] was released in May 2010. Besides these new standards which have been particularly developed for 60 GHz band wireless transmission, IEEE 802.11ad was formed in January 2009 as an amendment of the existing IEEE 802.11-2007. This amendment intended to define a standard for very high throughput operation in 60 GHz band, and is supposed to be complete very soon.

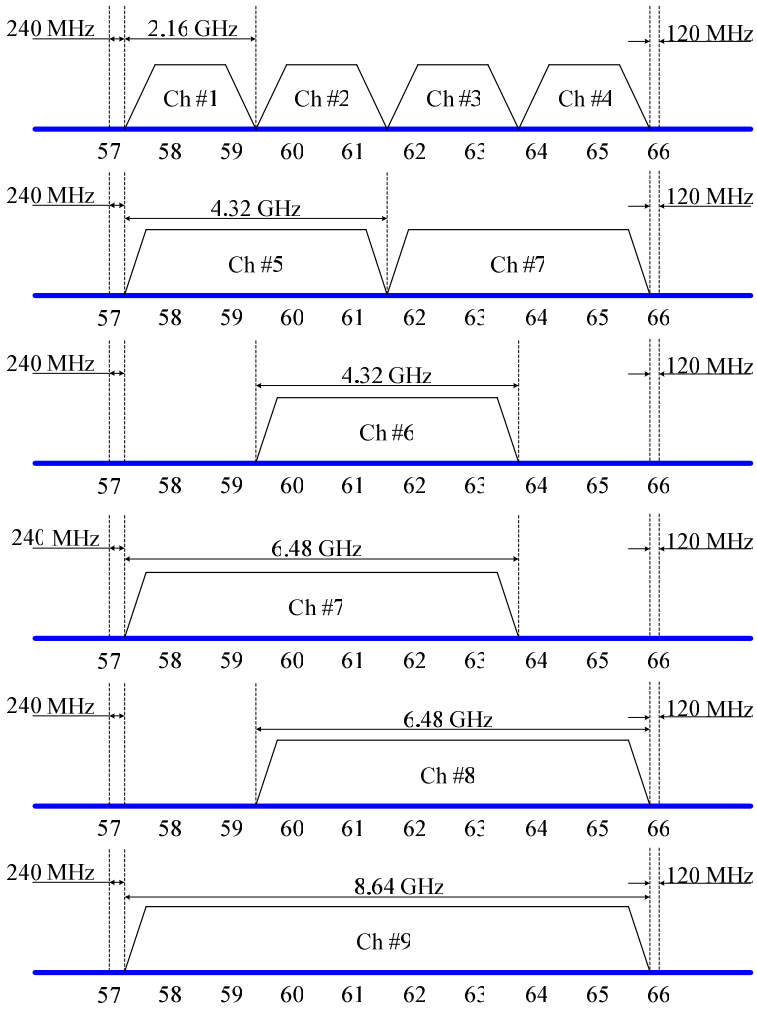

Fig. 1.2. channels allocated from 57 GHz to 66 GHz according to ECMA 387 [5]

In this thesis, a RoF system is proposed to be compliant with ECMA 387 standard. According to the ECMA 387 standard, there are four channels allocated from 57 GHz to 66 GHz. In addition, every neighboring channels can be bonded. The definition of the channels according to ECMA 387 standard are shown in Fig. 1.2. The 60 GHz RoF system compliant with ECMA 387 standard should support different modulation formats, such as BPSK, QPSK, 16-QAM, NS 8-QAM and OFDM.

1.2.1.2 Radio over fiber technique in 60 GHz wireless transmission

As the release of different standards for wireless transmission in 60 GHz band, different technical approaches are proposed. The key technique of 60 GHz wireless transmission relies on the broadband 60 GHz signal generation. Although many RF devices for 60 GHz have been developed, the high cost of the mmW signal source still restrains the growth of 60 GHz wireless transmission application. Since mmW can be simply generated by optical heterodyning, optical wireless networks based on the RoF technique came into play and emerged as an alternative solution with great potential.

As it is said before, due to the short range of the 60 GHz wireless transmission, numerous access nodes are required and connected with a single central office (CO). Optical wireless networks based on the RoF system provides a low cost optical connection between the CS with multiple BSs. Furthermore, the RoF technique provides the possibility to centralize broadband optical signal processing functions such as optical mmW generation, in order to simplify the architecture of the BS. Fig. 1.3 shows the architecture of a RoF system.

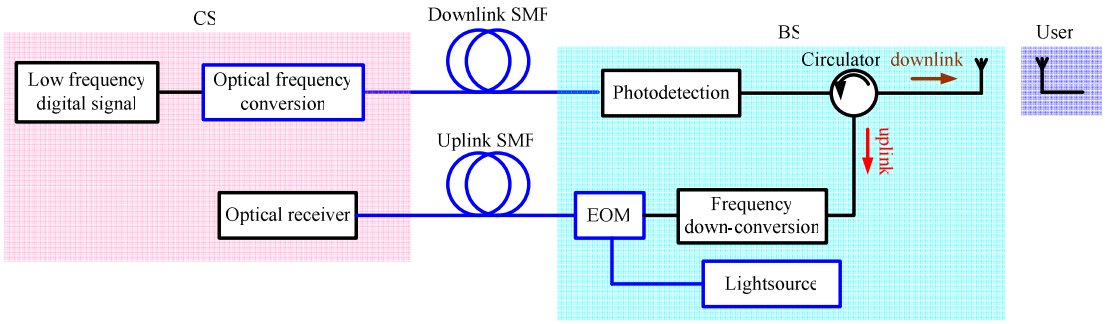

Fig. 1.3. Architecture of the 60 GHz RoF system. CS: central station, BS: base station, EOM: electro optic modulator, SMF: single mode fiber

In CS, the digital signal for the downlink from the central office to the user is

optically transmitted to the BS, and optically frequency converted through optical mmW generation. In each BS, the digital mmW is generated by the photodetection and send to the user by the wireless link. In the other hand, the uplink signal from the user to the central office is firstly received by the BS. In BS, received uplink signal at 60 GHz band is frequency down-converted to low frequency band to avoid using the mmW band optical modulator in each BS and broadband optical receiver in CS. The frequency down-converted uplink signal can modulate an optical carrier using any electro optical modulator (EOM) with CW laser source and transmitted to the CS by the optical link. In CS, since the uplink signal is already frequency down-converted to low frequency band, low-cost optical receiver can be used to recover the uplink signal.

It can be concluded that the key technology of the RoF downlink system is the mmW generation by using optical frequency conversion and photodetection. Regarding the uplink system, the solution of the frequency down-conversion is the critical technique which determines the cost of the total system.

1.2.2 Optical mmW generation

Generally speaking, photonic generation of microwave or mmW signals relies on the optical heterodyning technique. The mmW signal is issued from the beating of two optical tones with a mmW given interval frequency. From this point of view, the photonic generation of mmW can be divided into three categories. In the first category, two laser beams from two independent laser sources are applied to a photodetector (PD). In the second category, microwave signals are generated based on external modulation technique. The third category of optical mmW generation relies on a single laser source, which emits two coherent optical tones.

1.2.2.1 Optical heterodyning of two free laser sources

Fig. 1.4 shows the configuration of mmW generated by optical heterodyning of two incoherent optical tones, which are emitted by two free laser diodes (LDs) respectively. The RF signal with the frequency equivalent to the frequency interval of the two light sources is generated by the photodiode (PD).

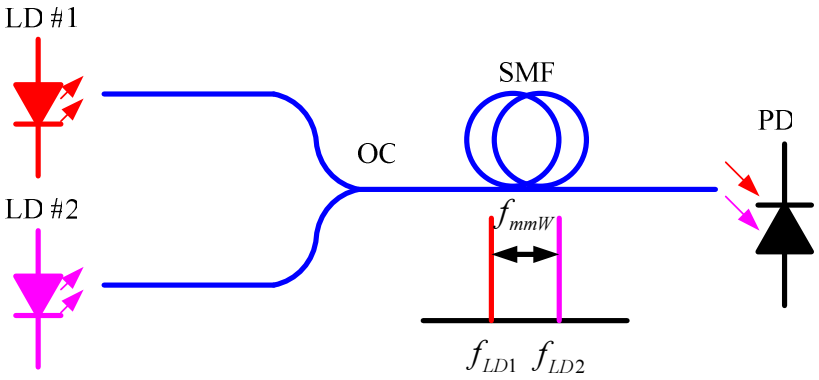

Fig. 1.4. Optical mmW generation by two free laser source

Since the two LDs are independent, the phases of the two optical tones are independant. To generate low phase noise RF signal, the phases of the two light sources are usually locked by implementing optical injection locking [6, 7] or by an optical phase-locked loop (OPLL) [8-12]. As in [11], The optical microwave carrier output is generated from the beating between the two lasers, which is detected by the photodiode. The resulting microwave signal is amplified and mixed with the reference signal from the local oscillator (LO) by a RF mixer. The resulting phase error signal is used to feed back to tune the frequency of the slave laser, forcing it to track the master laser with a frequency offset equal to the desired RF frequency (Fig. 1.5).

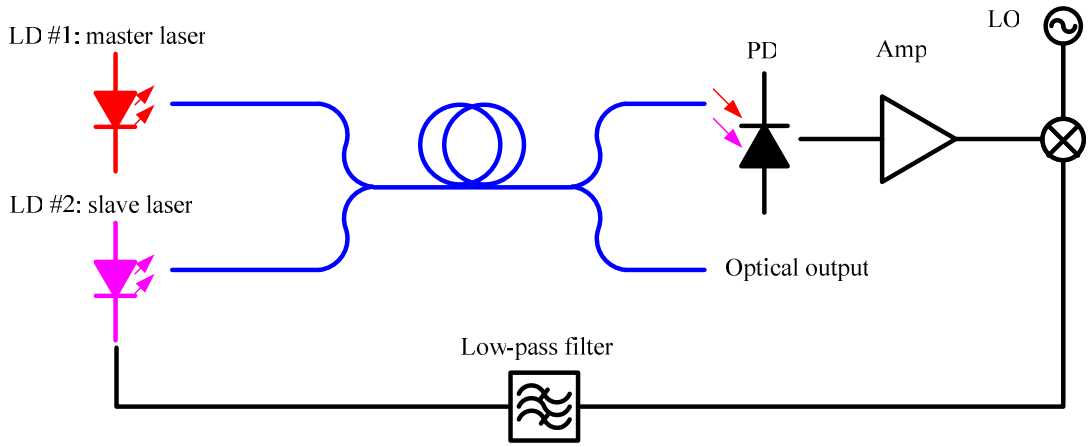

Fig. 1.5. Optical mmW generation with optical phase locked loop [11]

The phase noise can be significantly reduced by using the optical PLL. However, this technique requires pure LO signal at the receiver. In order to avoid the application of PLL, another technique has been proposed recently for optical beating of two free optical tones for mmW generation [13]. The experimental setup is shown in Fig. 1.6.

The CS with a simple architecture, which is composed of a LD (LD #1) and an optical modulator, emits a continuous wave (CW) optical carrier at f_{OP1} and a digital modulated optical sideband with a frequency interval of f_{IF} using an EOM. In each BS, another CW optical signal with the central frequency f_{OP2} , which is emitted by LD #2, is combined with the optical signal from the CS and fed into the PD for mmW generation. Resulting from the photodetection, a CW signal at f_{OP2} - f_{OP1}, and a digital signal at f_{OP2} -f_{OP1} -f_{IF}, are simultaneously issued and transmitted to the user. A self-heterodyne mixer is employed for the electrical down-conversion from mmW to intermediate frequency (IF) band. Since the two RF signals at f_{OP2} - f_{OP1} and f_{OP2} - f_{OP1} - f_{IF} suffer from the same phase noise due to the beating of the two free LDs, the phase noise of the down-converted IF signal is cancelled by the self-heterodyne mixing of the two RF signals. This technique does not require any high frequency device and any optical PLL in CS. Nevertheless this technique requires simultaneous wireless transmission of a CW mmW and the desired digital mmW, which will degrade the link budget and distance of the wireless transmission.

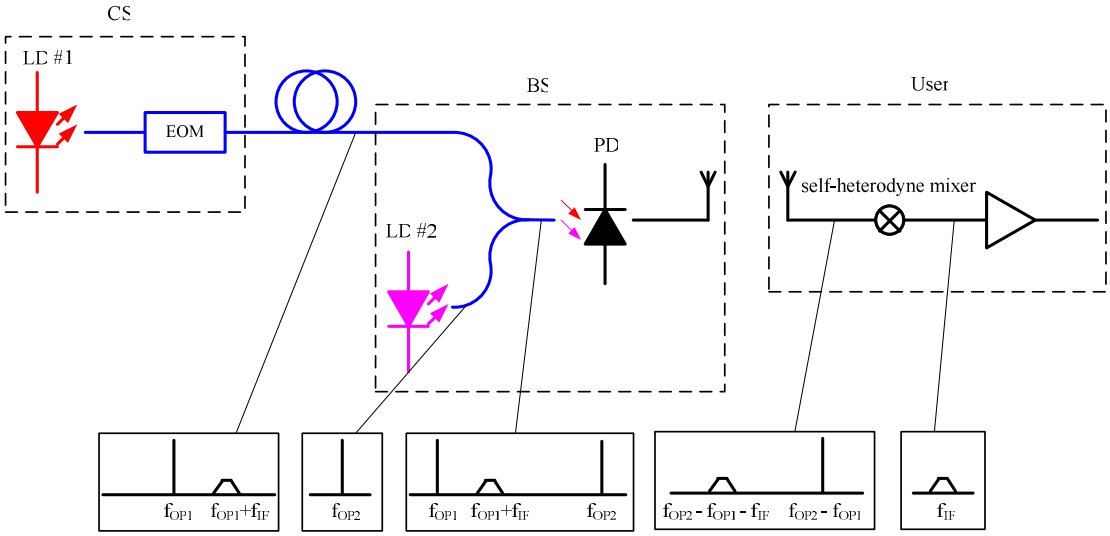

Fig. 1.6. Principle of self-heterodyne wireless transmission technique [13]

1.2.2.2 Optical heterodyning with external modulation technique

To minimize the phase noise impact due to the optical to electrical conversion, it is necessary to generate two optical tones with the same optical phase fluctuation. For that purpose, coherent optical wavelength generation is used. This technique is based on the optical heterodyning. The optical carrier from the laser source is modulated

with a LO signal with low phase noise contribution from an electrical generator, resulting in double sideband (DSB) modulation. Therefore, the output optical field contains optical carrier and optical sidebands which are coherent each other and can be used for optical heterodyning for low phase noise mmW generation. From the viewpoint of optical modulation technique, there are two categories. One is direct modulation technique, and the other is the external modulation technique, which are shown in Fig.1.7 (a) and (b) respectively.

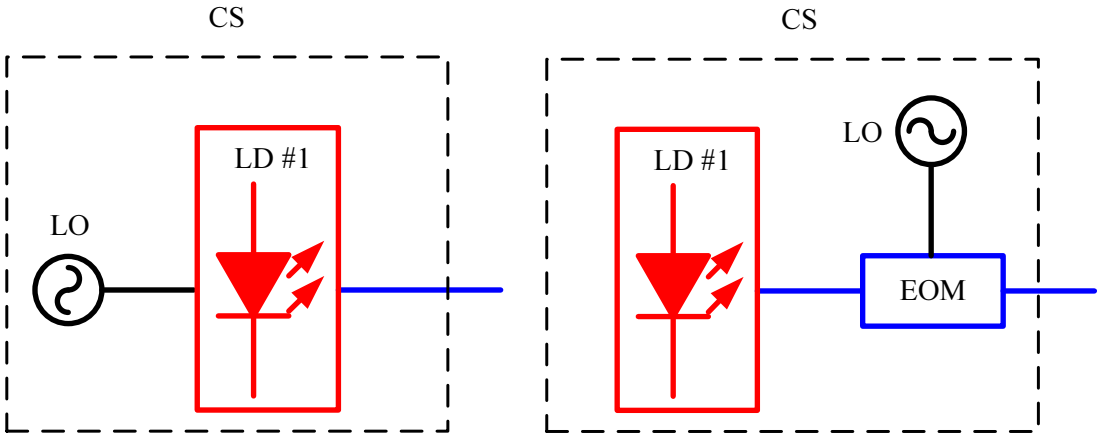

(a) direct modulation technique (b) external modulation technique

Fig. 1.7. Principle of coherent optical tones generation using optical modulation technique

Regarding the direct modulation, the current driving the LD is modulated by the RF signal. Therefore, the optical wave is intensity modulated by the RF signal. Direct modulation technique is widely used in baseband optical transmission benefiting from the simple configuration. Nevertheless, the bandwidth of the direct modulation is limited to 10 GHz, which is not enough for mmW generation. Consequently, the external modulation technique is widely used for mmW generation. An external EOM, which is driven by the CW LO signal at f_{LO}, is employed for optical frequency up-conversion. The optical tones are either intensity modulated or phase modulated by the EOM. The resulting optical field contains two optical sidebands with the interval frequency of $2f_{LO}$, which carry the same phase noise.

The optical mmW generation with the external modulation technique is usually implemented by cascaded EOMs [14-16]. As in [15] shown in Fig. 1.8, a Mach-Zehnder modulator (MZM) driven by 30 GHz LO signal is employed for optical frequency conversion. The two optical sidebands are modulated with the

digital signal by the second MZM driven by the baseband data stream. The 60 GHz broadband signal is generated by the photodetecion of the two digitally modulated optical tones. However, this technique only supports OOK 60 GHz signal due to the beating of two digitally modulated optical tones.

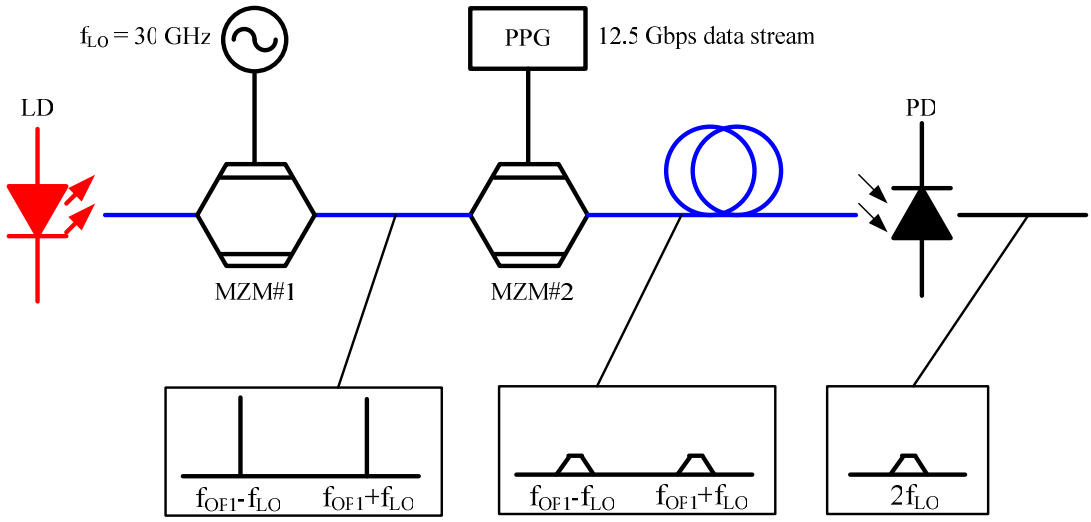

Fig. 1.8. Configuration of 12.5 Gbps mmW generation with two cascaded MZMs [15]

The 60 GHz wireless signal is supposed to support different modulation formats, such as quadrature phase shifting keying (QPSK), 16 quadrature amplitude modulation (16-QAM), and even orthogonal frequency division multiplexing (OFDM) [5]. For this reason, digital signal at IF band instead of baseband signal is applied to the MZM. Therefore, the mmW is issued from the beating of one digitally modulated optical tone with a CW optical signal. As in [16] shown in Fig. 1.9, the OFDM signal at f_{IF} = 3.342 GHz is applied to the first MZM. The second MZM, driven by the 30 GHz LO signal, is employed for the optical frequency up-conversion. As a result of the photodetection, the OFDM mmW at $2f_{LO}$ - f_{IF} = 56.658 GHz , the CW signal at $2f_{LO}$ = 60GHz and the OFDM signal at $2f_{LO}$ + f_{IF} = 63.342 GHz are generated. Here we need to mention that the OFDM mmW is issued from two pairs of beating between a digitally modulated optical tone with a CW optical tone, which will be sensitive to the optical chromatic dispersion impact [17-23].

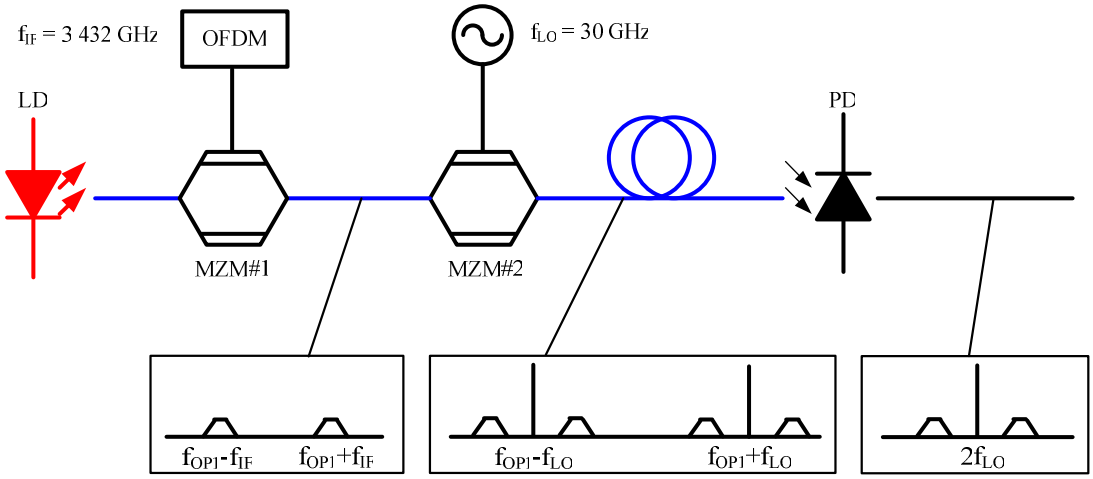

Fig. 1.9. Configuration of 60GHz OFDM signal generation with two cascaded MZMs [16]

To avoid the chromatic dispersion impact, the optical filter, such as fiber bragg grate (FBG), is employed to filter out one optical sideband [24, 25].

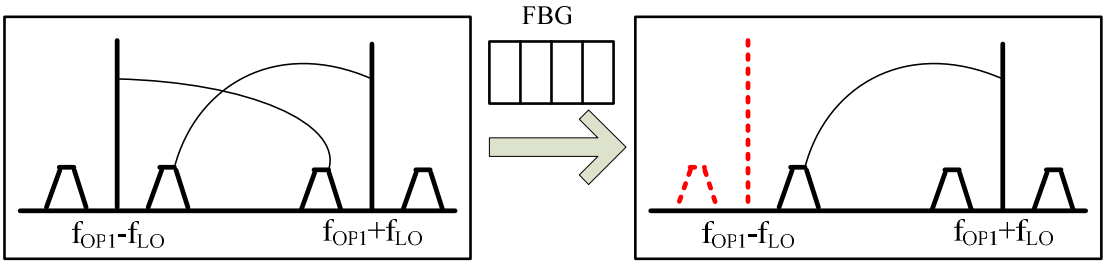

Fig. 1.10. optical spectrum of 60 GHz RoF system with cascaded MZM and FBG[16]

Fig. 1.10 shows the optical spectrum of the 60 GHz RoF system with cascaded MZM and the FBG. One optical sideband is suppressed by using the FBG. Therefore the desired mmW signal is generated with a single beating between a digitally modulated optical tone and a CW optical signal (Fig. 1.10).

1.2.2.3 Optical heterodyning with multi-wavelength laser source

To avoid using a RF signal generator and simplify the optical source for multi-wavelength emission, the idea of using a single light source emitting multi-wavelength has raised great interest [26, 27]. To obtain a beat signal at the output of PD, the light source should have at least two longitude modes. Since the two longitude modes emitted by a single laser source are independent, a PLL is required to reduce the phase noise of the mmW issued from the beating of the two longitude modes [28].

In 60 GHz RoF system, many systems are proposed based on the

dual-wavelength laser. In [29], a 60 GHz photonic upconversion system using dual-wavelength laser is proposed.

Very recently, multi-wavelength laser source, which can emit over 30 optical wavelength simultaneously, has been employed in a RoF system. The phase noise measurement has proved that this mode-locked laser diode (MLLD) laser shows high frequency stability and can support low phase noise mmW generation [30]. A mmW generation system based on this MLLD, which can emit over 30 longitude modes simultaneously, has been reported recently [31]. In [31], the 60 GHz mmW is generated by the photodetection of each neighboring modes emitted by the MLLD. However due to the chromatic dispersion, the length of the optical link is limited as it is shown in Fig. 1.11 (b), where $L_{CRITICAL}$ is defined as fiber length inducing a power drop-off is >3dB.

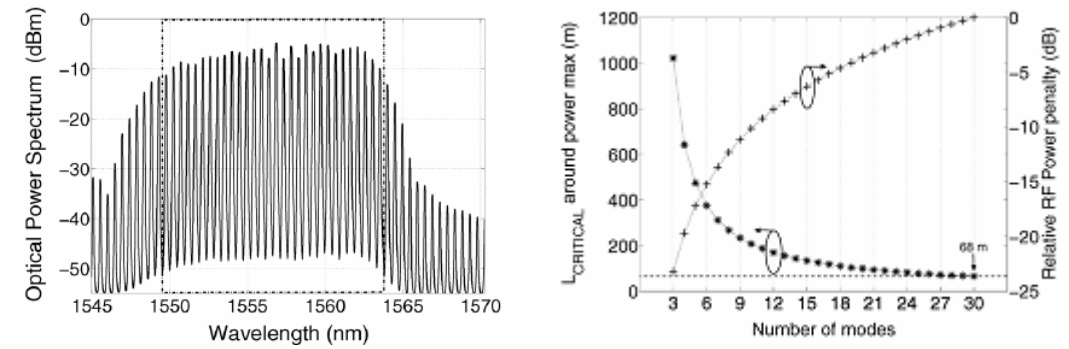

(a) optical spectrum of MLLD (b) the power penalty of the mmW as a function of number of modes

Fig. 1.11. The optical spectrum of MLLD and the power penalty of the mmW as a function of number of mode [31]

To overcome the chromatic dispersion and to meet the requirement of multi-user connection, the wavelength division multiplexing (WDM) technique is applied with the multi-wavelength laser source. As in [32], a super continuum (SC) light source has been developed for multi-wavelength light source. The proposed RoF system [32] is shown in Fig. 1.12. A WDM demultiplexer (DEMUX) is employed to extract each optical sub-carrier into a dedicated DEMUX output channel. As a result, in each BS, the mmW is generated by a single beating of a pair of optical sub-carriers.

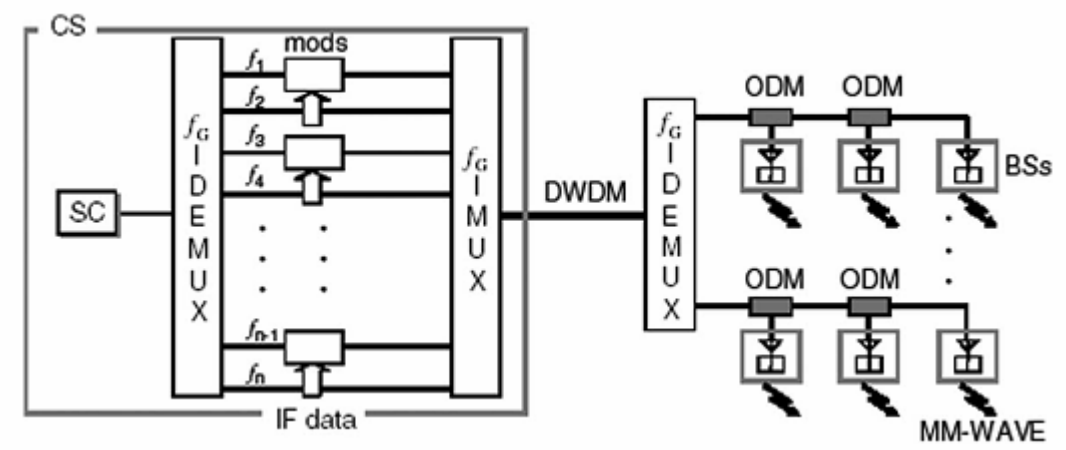

Fig. 1.12. Experimental setup of the mmW generation with SC light source and WDM DEMUX [32], ODM: optical drop multiplexer, mod: modulator

Although this SC light source can provide multi optical sub-carriers with the same optical phase jitter, which is reported in [30], special attention still need to be paid to the optical phase to intensity noise conversion due to different optical path induced by the WDM DEMUX [33]. Although the optical phase to intensity noise conversion is theoretically and experimentally demonstrated in many publications [34-38], there is no complete investigation which integrates the phase noise of the mmW due to the optical phase to intensity conversion and the phase noise contribution due to the electrical signal source in the RoF system. Moreover most of the research works focus on the phase noise of the pure CW mmW generation. There is no investigation which gives the solution to quantify the impact of the phase noise to the digitally modulated mmW signal.

1.2.3 Overview of the technology for the RoF uplink

As it has been discussed before, the key technology of the uplink is frequency down-conversion from mmW band to IF band before optical transmission from BS to CS to avoid using large band optical modulator in each BS and numerous expensive mmW band optical receiver in CS.

The simplest solution is to use external electrical mixer for frequency down-conversion. This technique requires a reference CW signal at 60 GHz to drive the mixer, which induces additional cost. To lower the cost of the infrastructure, the wireless uplink data can be down-converted by a remote recovered mmW carrier from

the downlink. As in [39], a bidirectional TDM RoF system is proposed, in which 1.25 Gbps downlink and 1.25 Gbps uplink are experimentally demonstrated. Very recently, another BS architecture based on the mmW self-homodyning technique has been proposed for the frequency down-conversion of the uplink signal [40]. As it is shown in Fig. 1.13, an electrical mixer is employed for the self-homodyne process. The uplink signal is divided in two parts, which are applied to the LO port and RF port of the external mixer respectively. Due to square-law characteristics, self-homodyning technique produces sum and difference frequencies of uplink RF signal which results in recovering baseband data. A low bandwidth MZM is employed for the frequency down-converted uplink signal modulation. In CS, a PD with a few GHz bandwidth is employed to recover the uplink signal. Nevertheless, since the frequency down-converted signal by self-homodyning technique only keeps the amplitude information from the original signal, this technique only supports pure amplitude modulated uplink signal, which is not enough corresponding to the standard of the wireless signal transmission at 60 GHz, as ECMA 387 [5] and IEEE 802.15.3c [3].

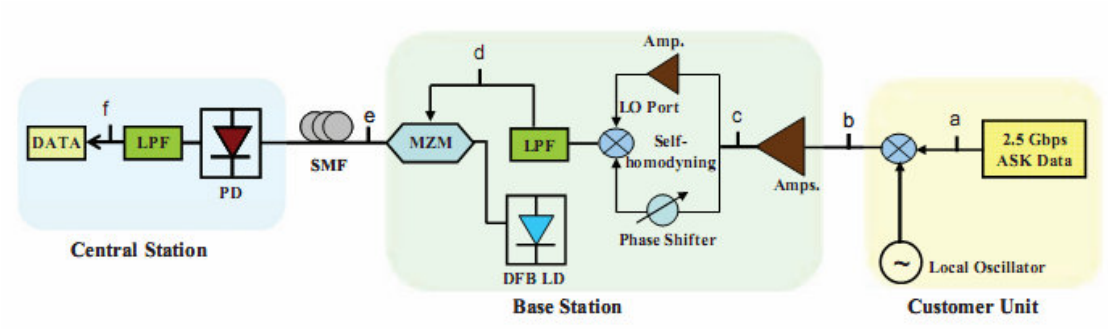

Fig. 1.13. Experimental setup of mmW frequency down-conversion with self-homodyning technique for RoF uplink [40]

To support all the modulation formats and simplify the BS, another frequency down-conversion technique using the optical electro-absorption modulator (EAM) has been proposed recently. As in [41], an uplink system based on the frequency down-conversion by using EAM is proposed and simulated. Fig. 1.14 shows the configuration for frequency down-conversion.

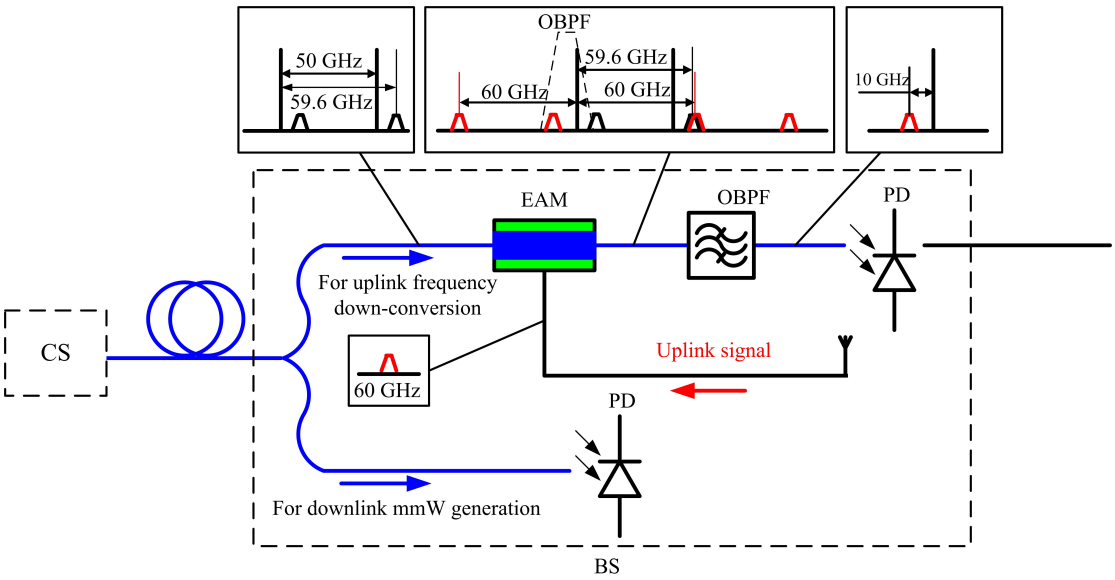

Fig. 1.14. Experimental setup of mmW frequency down-conversion by using EAM [41]. OBPF: optical band-pass filter, EAM: electro absorption modulator

The optical signal from the CS carries two CW optical tones with the frequency interval of 50 GHz, and a digitally modulated sideband for downlink transmission. The optical signal is applied to the EAM, which is fed by the uplink signal at 60 GHz band. As a result, the optical signal is actually modulated with the uplink signal and photodetected by a PD to generate 10 GHz uplink signal. However each BS requires a 60 GHz EAM, a 10 GHz PD for frequency down-conversion and a 60 GHz PD for downlink mmW generation.

To reduce the number of receivers in the BS, a single device, which can be used for photodetction and frequency down-conversion has raised great interest. A reflective electro absorption modulator (REAM) is proposed to replace the EAM plus the PD [42]. As in [42], for downlink, the REAM works as a photodetector and it is used as a EAM plus a PD for the frequency down-conversion of the uplink signal. However, it is necessary to change the bias of the REAM to use it either as a photodiode or a modulator, which would not be compatible with the necessary low latency of a high data rate bidirectional mmW over fiber system.

Another original solution is to use optoelectronic mixers for the uplink. Phototransistors based on InP material systems are regarded as one attractive solution for this remote up/down conversion. As in [43], a bidirectional RoF link based on an InP-InGaAs heterojunction photo transistor (HPT) optoelectronic mixer is proposed.

The uplink signal will be mixed with the remote LO signal delivered by the downlink system by the HPT behaving like an optoelectronic mixer. Similarly, the common p-i-n photodiode, which is biased in non-linear regime can be used as optoelectronic mixer [44]. The bidirectional RoF system for 10 GHz band RF transmission with the non-linear p-i-n PD has been investigated in our research group [45].

1.3 Future optical networks

1.3.1 Overview of the next generation of optical networks with WDM technique

Optical fiber access to the user, the so-called fibre-to-the-home (FTTH), is becoming a mature concept. PONs are deployed to implement FTTH in many areas, such as Japan, USA and Europe. A key issue to reach a highly scalable Passive Optical Network (PON) with very high splitting ratio is the high multiplexing level required to handle all individual signals (individual data flows) that travel along shared fibers. The available fiber bandwidth and current high-speed electronics allow high splitting ratios together with high bandwidth per user assignments. An objective in a next generation PON (ngPON) is to perform the multiplexing with limited complexity. Any of the basic independent dimensions of multiplexing can be used in optical communications. The multiplexing can be classified in three categories:

- Time domain: optical and electrical time division multiplexing (OTDM, ETDM), where each user (optical network unit, ONU) has access to individually assigned time slots.
- Electrical frequency domain: subcarriers multiplexing (SCM), in which the baseband signal to a particular user is modulated with a unique specific RF signal and subsequently modulates the optical wave.
- Optical frequency domain: wavelength division multiplexing (WDM), with the possible different densities (Coarse-WDM CWDM, Dense WDM DWDM), where each user is served by a particular optical wavelength.

Since each user is served by a particular optical wavelength, the WDM-PON can offer the highest data rate compared to any other multiplexing technique. The huge optical spectrum can be exploited by using WDM technique to provide each user a virtual unlimited bandwidth. Moreover, this technique creates a virtual point-to-point connection, which increases the security during the optical transmission. Hence, WDM-PON has attracted much interest as a promising next generation PONs for FTTH.

Fig. 1.15 shows the basic architecture of the WDM-PON. Optical line termination (OLT) is composed of numerous optical transmitters operating in different wavelength. All the optical signals are transmitted by a single optical fiber. In the remote node (RN), a passive WDM demultiplexer (DEMUX) is applied to select different optical signal to the dedicated optical network unit (ONU) placed at each end user. Since one optical link of the typical PON is shared by 32 or more users, the WDM-PON system is typically proposed to feed 32 or more ONUs.

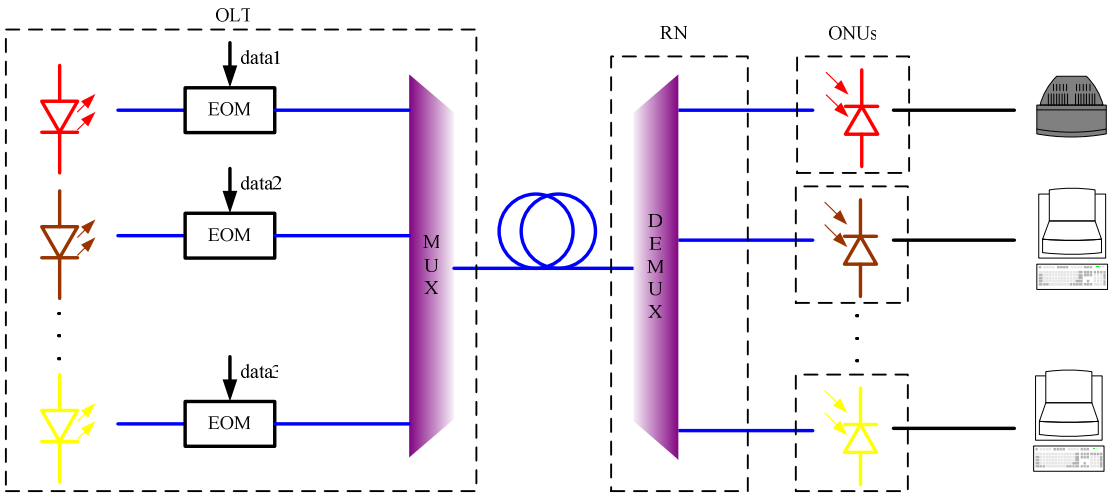

Fig. 1.15. Typical architecture of WDM-PON

The WDM-PON can be divided in coarse WDM-PON (CWDM-PON) and dense WDN-PON (DWDM-PON) corresponding to different possible wavelength densities. CWDM is emerging as a robust and economical solution. Typical CWDM spacing is 20 nm (ITU-T G.694.2 grid, International Telecommunication Union) and does not require a temperature control to build sufficiently stable wavelength sources.

The WDM extension DWDM operates with channel spacing as small as 0.8 nm

(100 GHz), 0.4 nm (50 GHz) or even 0.2 nm (25 GHz), for higher capacity applications compared to CWDM technique. Another main advantage relies on the fact that it is easy to implement optical wireless network into the DWDM-PON due to the requirement of multi-band transmission in future optical networks, which has raised great interest recently.

The main challenge with WDM-PON is cost. Since each subscriber is assigned his own wavelength, the OLT must transmit 32 (or more) different wavelengths versus one shared wavelength as found in traditional PON architecture. Likewise, each ONU operates at a dedicated wavelength which suggests that every ONU requires an expensive tunable laser. This would be very cost prohibitive. To avoid using tunable laser in each ONU, most WDM-PON systems now rely on reflective semiconductor optical amplifier (RSOA) [46-48]. The RSOA based WDM-PON is usually configured in loop-back architecture for colorless operation of ONU. The wavelength of the emitted signal from ROSA is locked by the seed wavelength coming from the OLT.

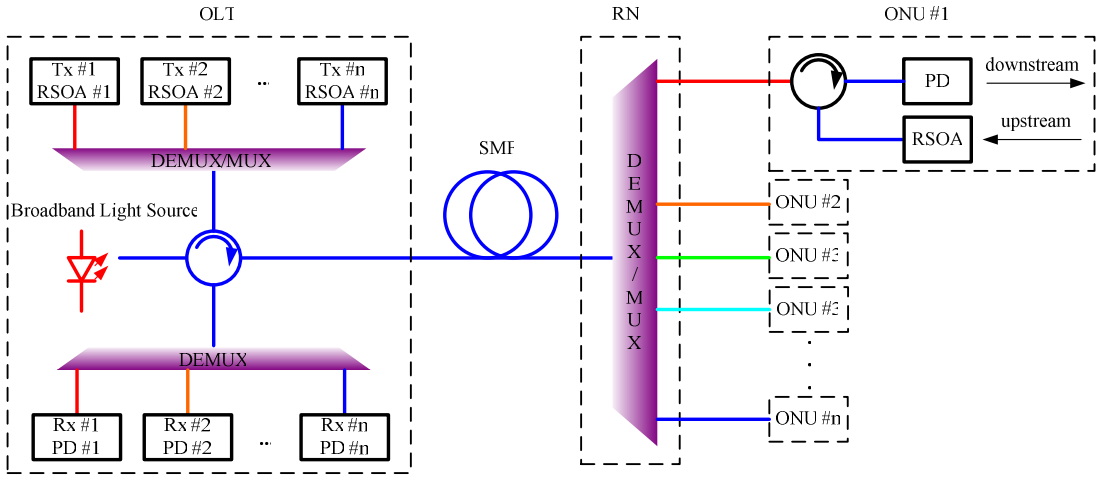

Fig. 1.16. RSOA based WDM-PON[47]

Fig. 1.16 shows a configuration of RSOA based WDM-PON networks reported in [47]. The OLT includes a broadband light source that passes through a 32-channel DEMUX. Each of DEMUX channel is connected to a RSOA, which is directly modulated by 1.25 Gbps signal. Each RSOA is allocated to a particular ONU. Each ONU is composed of a PD performing as receiver for downstream and a RSOA performing as transmitter for upstream. The emitted wavelength of the RSOA is

locked by the seed wavelength from the OLT and DEMUX from the RN. As a result, there is no need to stock an inventory of ONUs at different wavelengths. All ONUs in the WDM-PON networks by this configuration are identical.

1.3.2 Simultaneous wired and wireless transmission

Future access networks should provide broadband connectivity to end users, both in wireless and wired transmission media. Fig. 1.17 shows a optical network supporting multi-band signal transmissions using DWDM technique [49]. Different signals for wired and wireless transmissions are operated in CS and transmitted to the remote access nodes (RAN). A DWDM DEMUX is employed to select different optical wavelengths to the dedicate access point (AP).

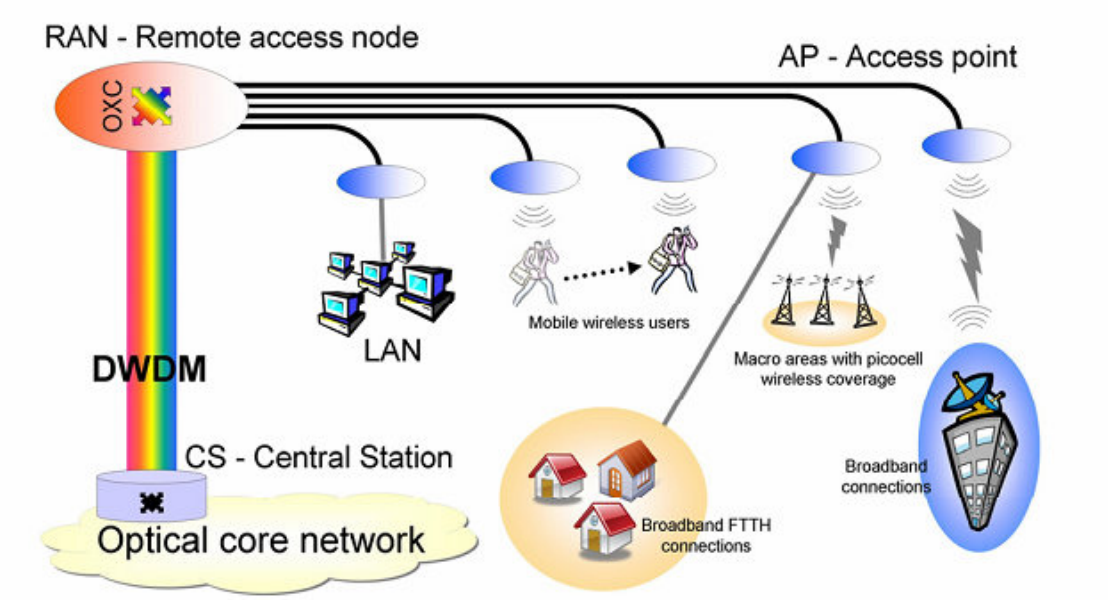

Fig. 1.17. Propose futuristic optical networks supporting different communication services [49]

In [50, 51], a WDM-PON system compatible for wired transmission and UWB transmission from 3.1 GHz to 10.6 GHz band has been introduced. As in [51], a WDM-PON system with simultaneous wired and wireless signal transmission is demonstrated. The schematic is shown in Fig. 1.18. The digital signal modulates a directly modulated laser (DML). A Mach-Zehnder modulator (MZM), which is driven by a clock signal from the pulse pattern generator (PPG), is employed for optical frequency conversion. The system is compatible with the WDM-PON. The low bandwidth optical modulator (MZM) used for the optical frequency conversion is a

low-cost device and can be shared by numerous users. However, the wired and wireless signals provided by this system are issued from the same data stream.

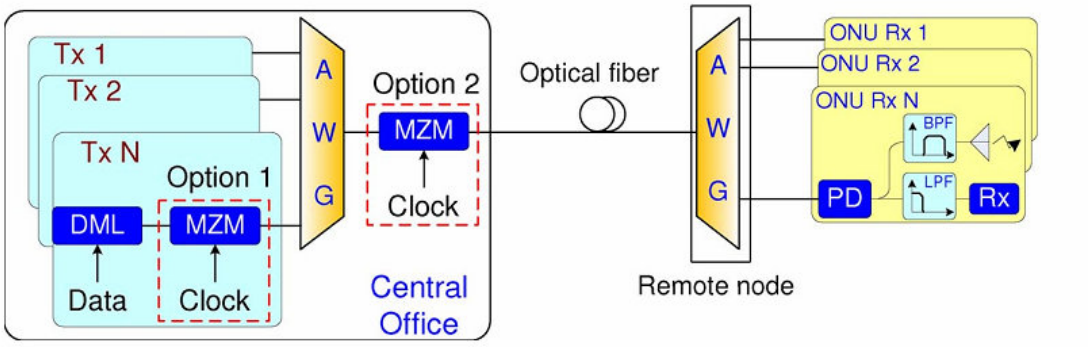

Fig. 1.18. A proposed WDM-PON system compatible with UWB transmission [51]. Rx: receiver, ONU: optical network unit

The 60 GHz RoF compatible system for wired and wireless transmission has been raising great interest for the last 5 years. A WDM-RoF supporting simultaneous transmission of mmW band and baseband has been demonstrated in the experiment [39, 52]. As in [39] (Fig. 1.19), the experiment is performed by a tunable laser source (TLS) cascaded with a MZM, which is employed to generate two optical wavelengths with a electrical CW signal modulation. A WDM DEMUX is applied to select the two sidebands to feed all the end-user ONU. In one channel, a RSOA is employed to realize the baseband digital modulation. The other optical channel is set to be free. The two optical channels are combined by a 3 dB coupler and transmitted by the optical link to the dedicated BS. In BS, another 3 dB coupler is used to separate the optical signal to baseband or 60 GHz band receivers. The wired and broadband mmW with the same information are generated in this configuration.

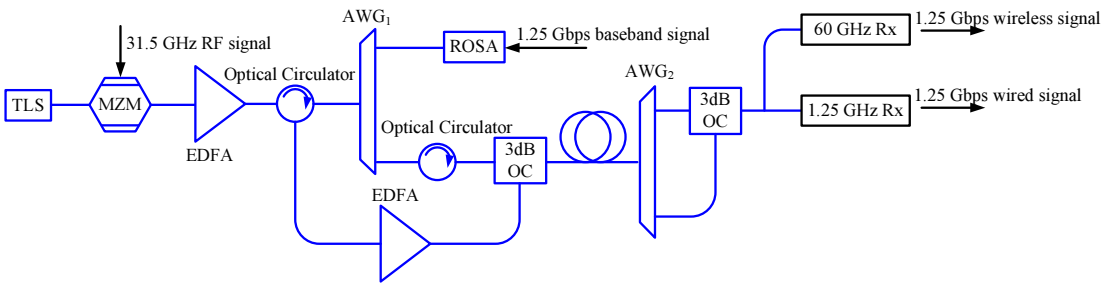

Fig. 1.19. Schematic of full colorless WDM-RoF access network supporting the simultaneous transmission of gigabit wired and wireless data [39]. AWG: Arrayed Waveguide Grating

Another similar approach has been introduced in [53]. Experiment is performed by a Super Continuum (SC) light source, which emits multi coherent wavelengths with the

frequency interval of 25 GHz. Compared to [39], the difference lies in the baseband modulation. The baseband signal is modulated in every optical sub-carrier with 50 GHz spacing. Between every two baseband modulated optical sub-carriers, the broadband signal at IF modulation is implemented, which is shown in Fig. 1.20.

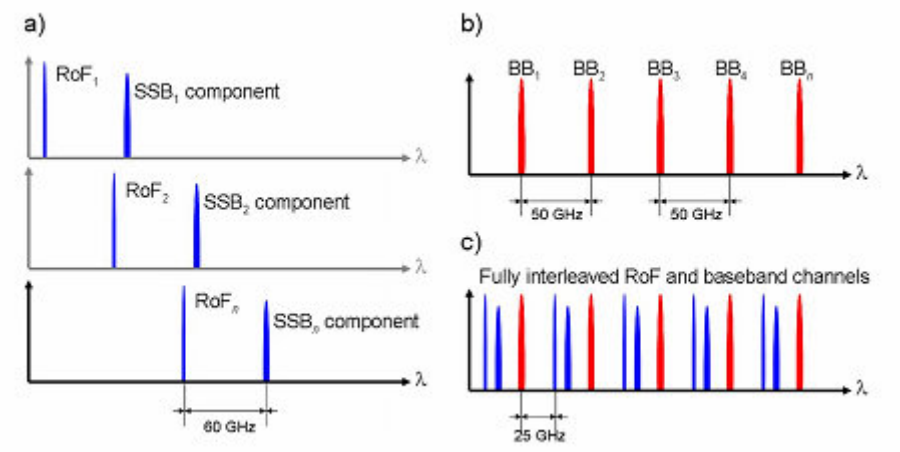

Fig. 1.20. Optical spectra design in [53]. (a)The RoF signals are interleaved to take advantage of the photonic up conversion technique, (b)where as the base band signals are 50-GHz spaced, (c)All the signals are finally fully interleaved.

In [54], another integration of RoF and WDM-PON system, which supports 112 Gbps baseband and 10 Gbps 60 GHz wireless signal, is proposed. The configuration of the system is shown in Fig. 1.21.

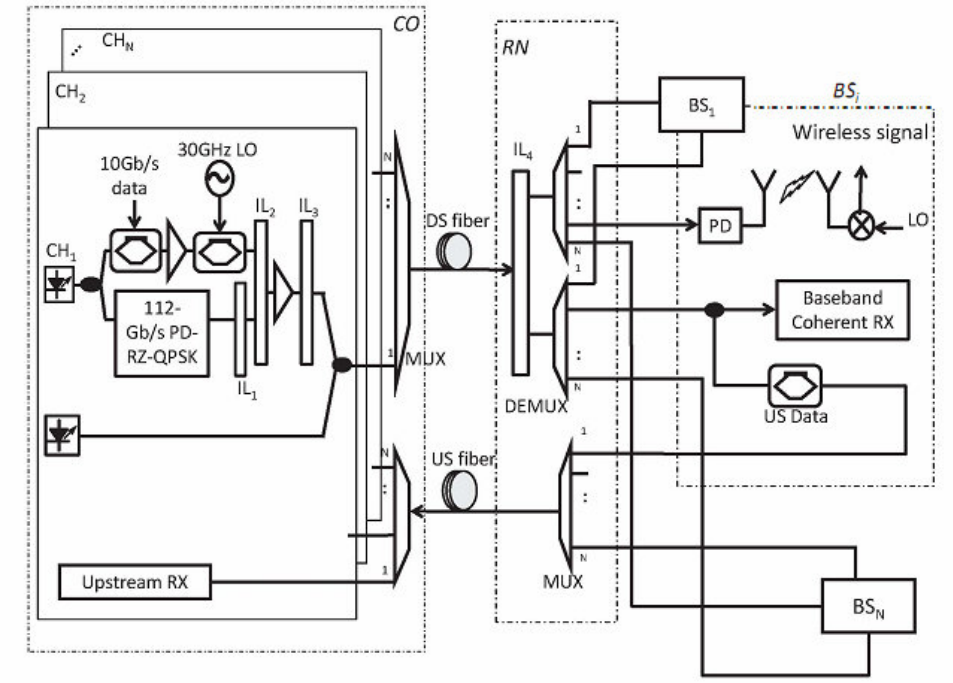

Fig. 1.21. Proposed inter integration of RoF and WDM-PON system [54]

Both of the systems presented in [53] and in [54] need an optical channel for baseband transmission, two optical channels for mmW generation. In order to increase the system capacity and reduce the number of optical modulators to make the infrastructure cheaper, another technique for modulating both baseband and RF signals with a unique optical modulator has attracted great interest recently. As in [55, 56] a single electroabsorption modulator (EAM) is employed to realize the baseband and passband modulation simultaneously as shown in Fig. 1.22. The device needs to be properly operated by finding its optimal operation points and paying special attention to the distortion produced by the nonlinearity of the EAM, which is the weak point of this configuration.

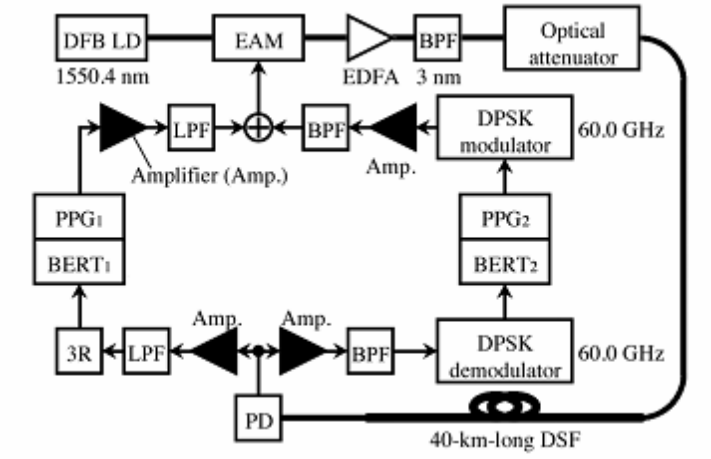

(a) Experimental setup

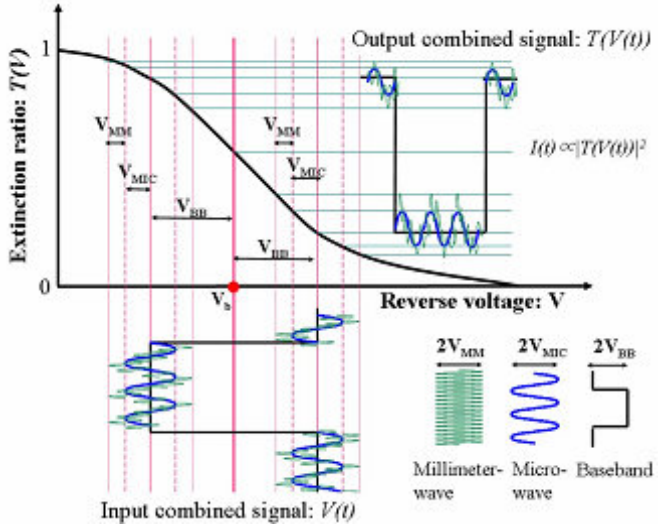

(b) Multiband modulation with EAM

Fig. 1.22. Configuration for simultaneous baseband and mmW transmission

Furthermore, the multi-band modulation technique with different optical

modulators has been experimentally demonstrated. In [57], a single MZM is employed for both digital modulation and continuous wave (CW) signal modulation, and a 60 GHz signal and a 20 GHz signal with the same data stream are generated simultaneously. The convergence of RoF and WDM-PON system needs the simultaneous wired and wireless transmission. In [58], an optical I/Q modulator is used for both baseband and broadband 60 GHz signal generation. However the optical I/Q modulator is actually composed of two integrated intensity modulators. In [59], a single MZM is used to generate independent wireline and 40 GHz wireless signals, which is shown in Fig. 1.23.

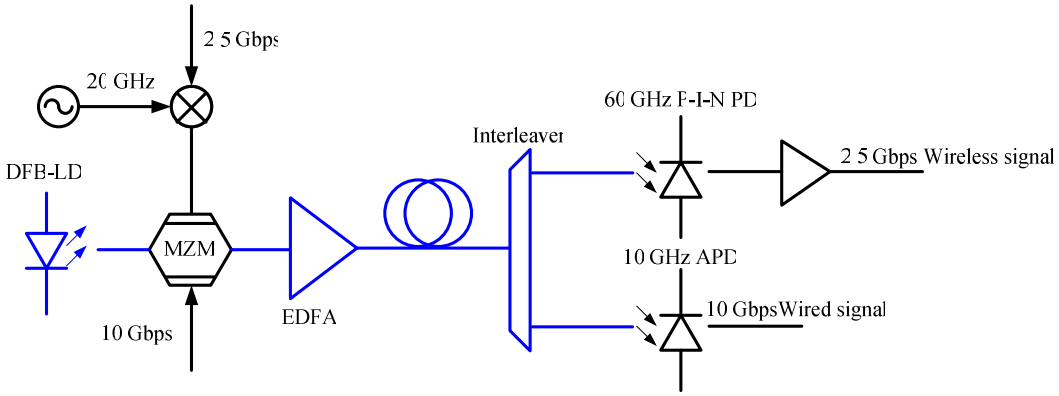

Fig. 1.23. Simultaneous baseband and mmW signal generation by multi-band modulation with single MZM [59]

In [59], a single dual-arm MZM is employed for both baseband modulation and RF modulation. The baseband signal and RF signal are applied to two different electrodes of the MZM respectively. Since the optical mmW is generated by the beating of the two optical sidebands, only OOK modulation format is supported by this configuration.

Based on the multi-band modulation technique, a few approaches for the convergence of 60 GHz optical generation and WDM-PON for baseband transmission have been proposed recently. The system compatible for wired and wireless signal transmission with multi-band modulation with single optical modulator attract much interest and drives the research about RoF and WDM-PON towards mergence. The multi-band modulation with different optical modulators, such as MZM, EAM, have been experimentally investigated. Nevertheless, among the numerous approaches,

there is no deep investigation on the interference between modulation bands to our best knowledge.

1.4 Investigated issues on WDM-RoF networks

In this thesis, a converged RoF and WDM-PON system is proposed, in which 60 GHz signal generation and multi-gigabit baseband signal transmission are simultaneously operated.

In RoF system, the 60 GHz mmW with low phase noise is generated by photodetecion of two optical tones with the same phase jitter. With WDM technique, the two optical tones are selected in different optical channels and the optical phase to intensity noise conversion is induced due to the different optical length. How to quantify the impact due to the phase to intensity noise conversion becomes an important issue for RoF technique using WDM technique. Furthermore, the electrical generators are widely applied in RoF system for frequency up-conversion. The phase noise of the mmW should include the contribution of these electrical sources. Our objective is to provide modeling of phase to intensity noise conversion to quantify the impact on system performance. This model will be relevant to define laser specifications to limit the impact of phase to intensity noise conversion.

To make it effective the convergence of wireless and wireline networks, a main objective of this work is also to integrate the optical mmW generation technique into a typical WDM-PON infrastructure, meeting the requirements for ECMA 387 radio standard and FTTH. Our aim is to provide experimental demonstration of a mutualized infrastructure, addressing multi-users.

To lessen the cost of this mutualized infrastructure, we have already mentioned that multi-band modulation technique with a single optical modulator becomes the key issue of the system with simultaneous transmission of wireless and wired signals. However, few articles discussed the interference between different modulation bands. Furthermore, although many approaches have been proposed for multi-band modulation with a single optical modulator, to our best knowledge, there is no

comparison of these multi-band modulation techniques with different optical modulators. Our objective is to make a comparison between the different modulation techniques to achieve high performance and high simplicity. A comprehensive study on the multi-band modulation needs to be carried out to find out the optimum modulator choice and the best operating conditions.

As discussed in section 1.2.3, many approaches focused on the RoF downlink transmission. Up-link transmission is of critical importance regarding the cost of broadband E/O transceivers. Our extensive investigations on the RoF WDM-PON downlink have been combined with the research work of Flora PARESYS (PhD at IMEP-LAHC), working on RoF mmW up-link to provide the demonstration of a bi-directional mmW over fiber system. This bi-directional system takes benefit of the remotely delivered local oscillator from our RoF WDM-PON technique to realize frequency down-conversion for the up-link scheme.

The manuscript is organized as follows.

In chapter 2, the complete phase noise of the optically generated mmW signal, which includes optical phase to intensity noise conversion and the phase noise contribution of the electrical generator, will be theoretically and experimentally investigated. A theoretical model for quantification of phase noise impact to digital signal will be built. Moreover, a RoF downlink system using WDM technique, which is compliant with ECMA 387 standard is experimentally demonstrated. Multi-gigabit mmW signal is generated by photonic generation.

In chapter 3, the convergence of RoF technique and WDM-PON is proposed. Simultaneous transmission of 60 GHz signal compliant with ECMA 387 standard and multi-gigabit baseband signal is demonstrated experimentally. Particularly, multi-band modulation with a single MZM as parallel phase modulators is deeply investigated. The interference between baseband modulation and RF modulation is inquired based on the multi-band modulation model. Furthermore, multi-band modulation techniques with different optical modulators are compared, which makes sense not only for converged 60 GHz RoF and WDM-PON system but also for different multi-band transmission system, such as simultaneous baseband and UWB band transmission

system.

In chapter 4, the bidirectional RoF system using photonic mixing and WDM technique is proposed. The photonic mixing with non-linear biased PD is experimentally investigated. The downlink system which suffers from the power reduction induced by the non-linear biased PD is inquired.

References of chapter 1

[1] P. X. a. A. V. Su-Khiong Yong, "60 GHz Technology for Gbps WLAN and WPAN: From Theory to Practice," *John Wiley & Sons, Ltd,* 2011.

[2] Z. Jia, *et al.*, "Key enabling technologies for optical-wireless networks: Optical millimeter-wave generation, wavelength reuse, and architecture," *Journal of Lightwave Technology,* vol. 25, pp. 3452-3471, Nov 2007.

[3] IEEE, "IEEE Standard for Information technology - Telecommunications and information exchange between systems - Local and metropolitan area networks - Specific requirements. Part 15.3: Wireless Medium Access Control (MAC) and Physical Layer (PHY) Specifications for High Rate Wireless Personal Area Networks (WPANs) Amendment 2: Millimeter-wave-based Alternative Physical Layer Extension," *IEEE Std 802.15.3c-2009 (Amendment to IEEE Std 802.15.3-2003),* pp. c1-187, 2009.

[4] Wigig, "http://wirelessgigabitalliance.org/specifications/."

[5] ECMA387. *http://www.ecma-international.org/publications/standards/Ecma-387.htm*.

[6] J. Genest, *et al.*, "Microwave signals generated by optical heterodyne between injection-locked semiconductor lasers," *Quantum Electronics, IEEE Journal of,* vol. 33, pp. 989-998, 1997.

[7] L. Goldberg, *et al.*, "Microwave signal generation with injection-locked laser diodes," *Electronics Letters,* vol. 19, pp. 491-493, 1983.

[8] Z. C. F. Fan and M. Dagenais, "Optical generation of a megahertz-linewidth microwave signal using semiconductor lasers and a discriminator-aided phase-locked loop," *Ieee Transactions on Microwave Theory and Techniques,* vol. 45, pp. 1296-1300, Aug 1997.

[9] K. J. Williams, *et al.*, "6-34 GHz offset phase-locking of Nd:YAG 1319 nm nonplanar ring lasers," *Electronics Letters,* vol. 25, pp. 1242-1243, 1989.

[10] J. J. O'Reilly, *et al.*, "Optical generation of very narrow linewidth millimetre wave signals," *Electronics Letters,* vol. 28, pp. 2309-2311, 1992.

[11] L. N. Langley, *et al.*, "Optical phase locked loop (OPLL) module for use as a 9 GHz source in phased array communications antennas," in *Microwave Photonics, 1998. MWP '98. International Topical Meeting on*, 1998, pp. 141-142.

[12] S. Takasaka, *et al.*, "External Synchronization of 160-GHz Optical Beat Signal by Optical Phase-Locked Loop Technique," *Photonics Technology Letters, IEEE,* vol. 18, pp. 2457-2459, 2006.

[13] C. Chang-Soon, *et al.*, "Millimeter-Wave Fiber-Fed Wireless Access Systems Based on Dense Wavelength-Division-Multiplexing Networks," *Microwave Theory and Techniques, IEEE Transactions on,* vol. 56, pp. 232-241, 2008.

[14] Z. Ye, *et al.*, "Photonic Generation of M-QAM/M-ASK Signals at Microwave/Millimeter-Wave Band Using Dual-Drive Mach–Zehnder Modulators With Unequal Amplitudes," *Lightwave Technology, Journal of,* vol. 26, pp. 2604-2610, 2008.

[15] M. Weiss, *et al.*, "60GHz radio-over-fibre wireless system for bridging 10Gb/s

ethernet links," in *Optical Communication, 2008. ECOC 2008. 34th European Conference on*, 2008, pp. 1-2.

[16] G. H. Nguyen, *et al.*, "Generation of 60-GHz MB-OFDM Signal-Over-Fiber by Up-Conversion Using Cascaded External Modulators," *Journal of Lightwave Technology,* vol. 27, pp. 1496-1502, Jun 2009.

[17] G. H. Smith, *et al.*, "Overcoming chromatic-dispersion effects in fiber-wireless systems incorporating external modulators," *Microwave Theory and Techniques, IEEE Transactions on,* vol. 45, pp. 1410-1415, 1997.

[18] Y. Le Guennec, *et al.*, "Improvement of dispersion resistance in analog radio-on-fiber upconversion links," in *Microwave Photonics, 2003. MWP 2003 Proceedings. International Topical Meeting on*, 2003, pp. 303-306.

[19] N. Giang Hoang, *et al.*, "Importance of Chirp Effect in Millimeter Wave Optical Upconversion Systems," *Lightwave Technology, Journal of,* vol. 29, pp. 1753-1758, 2011.

[20] U. Gliese, *et al.*, "Chromatic dispersion in fiber-optic microwave and millimeter-wave links," *Microwave Theory and Techniques, IEEE Transactions on,* vol. 44, pp. 1716-1724, 1996.

[21] A. F. Elrefaie, *et al.*, "Chromatic dispersion limitations in coherent lightwave transmission systems," *Lightwave Technology, Journal of,* vol. 6, pp. 704-709, 1988.

[22] G. H. Smith, *et al.*, "Technique for optical SSB generation to overcome dispersion penalties in fibre-radio systems," *Electronics Letters,* vol. 33, pp. 74-75, 1997.

[23] J. N. Maran, *et al.*, "Chromatic dispersion measurement using a multiwavelength frequency-shifted feedback fiber laser," *Instrumentation and Measurement, IEEE Transactions on,* vol. 53, pp. 67-71, 2004.

[24] G. H. Nguyen, *et al.*, "Optical Techniques for Up-Conversion of MB-OFDM Signals in 60 Ghz Band Using Fiber Bragg Grating," in *Communications, 2009. ICC '09. IEEE International Conference on*, 2009, pp. 1-5.

[25] H. G. Nguyen, *et al.*, "All optical up-conversion of WLAN signal in 60 GHz range with side-band suppression," in *Radio and Wireless Symposium, 2009. RWS '09. IEEE*, 2009, pp. 590-593.

[26] M. Hyodo, *et al.*, "Generation of millimetre-wave radiation using a dual-longitudinal-mode microchip laser," *Electronics Letters,* vol. 32, pp. 1589-1591, Aug 1996.

[27] C. Xiangfei, *et al.*, "Photonic generation of microwave signal using a dual-wavelength single-longitudinal-mode fiber ring laser," *Microwave Theory and Techniques, IEEE Transactions on,* vol. 54, pp. 804-809, 2006.

[28] D. Wake, *et al.*, "Optical generation of millimeter-wave signals for fiber-radio systems using a dual-mode DFB semiconductor laser," *Microwave Theory and Techniques, IEEE Transactions on,* vol. 43, pp. 2270-2276, 1995.

[29] M. L. Dennis, *et al.*, "Photonic upconversion of 60 GHz IEEE 802.15.3c standard compliant data signals using a dual-wavelength laser," in *IEEE Photonics Society, 2010 23rd Annual Meeting of the*, 2010, pp. 383-384.

[30] T. Kuri, *et al.*, "Characterizations of supercontinuum light source for WDM millimeter-wave-band radio-on-fiber systems," *Photonics Technology Letters, IEEE,* vol. 17, pp. 1274-1276, 2005.

[31] F. Brendel, *et al.*, "Chromatic Dispersion in 60 GHz Radio-Over-Fiber Networks Based on Mode-Locked Lasers," *Lightwave Technology, Journal of,* vol. 29, pp. 3810-3816, 2011.

[32] T. Nakasyotani, *et al.*, "Wavelength-division-multiplexed millimeter-waveband radio-on-fiber system using a supercontinuum light source," *Journal of Lightwave Technology,* vol. 24, pp. 404-410, Jan 2006.

[33] A. Hirata, *et al.*, "Low-phase noise photonic millimeter-wave generator using an AWG integrated with a 3-dB combiner," in *Microwave Photonics, 2004. MWP'04. 2004 IEEE International Topical Meeting on*, 2004, pp. 209-212.

[34] M. R. Salehi, *et al.*, "Influence of the chirp effect of DFB laser in phase-to-intensity noise conversion in RF-modulated optical links," in *Microwave Symposium Digest, 2003 IEEE MTT-S International*, 2003, pp. 1371-1374 vol.2.

[35] P. Gallion and G. Debarge, "Quantum Phase Noise and Field Correlation in Single Frequency Semiconductor Laser Systems," *Quantum Electronics, IEEE Journal of,* vol. 20, pp. 343-349, 1984.

[36] M. R. Salehi and B. Cabon, "Theoretical and experimental analysis of influence of phase-to-intensity noise conversion in interferometric systems," *Journal of Lightwave Technology,* vol. 22, pp. 1510-1518, 2004.

[37] M. Poulin, *et al.*, "Effect of laser decorrelation on the phase noise of RF signals generated by optical mixing of modulation sidebands," in *Microwave Photonics (MWP), 2010 IEEE Topical Meeting on*, 2010, pp. 253-256.

[38] M. M. Rad and J. A. Salehi, "Phase-induced intensity noise in digital incoherent all-optical tapped-delay line systems," *Lightwave Technology, Journal of,* vol. 24, pp. 3059-3072, 2006.

[39] W. Yong-Yuk, *et al.*, "Full Colorless WDM-Radio Over Fiber Access Network Supporting Simultaneous Transmission of Millimeter-Wave Band and Baseband Gigabit Signals by Sideband Routing," *Journal of Lightwave Technology,* vol. 28, pp. 2213-2218, 2010.

[40] A. H. M. Razibul Islam, *et al.*, "Simplification of base station and uplink optical transport in millimeter-wave radio-over-fiber system employing RF self-homodyning," in *Microwave Photonics, 2011 International Topical Meeting on & Microwave Photonics Conference, 2011 Asia-Pacific, MWP/APMP*, 2011, pp. 17-20.

[41] Y. Takahashi, *et al.*, "An Effect of Downlink Optical Sideband Suppression on Uplink Transmission in Full-Duplex DWDM Millimeter-Wave-Band Radio-over-Fiber," in *Microwave Photonics, 2007 IEEE International Topical Meeting on*, 2007, pp. 112-115.

[42] B. Charbonnier, *et al.*, "Ultra-wideband radio-over-fiber techniques and networks," in *Optical Fiber Communication (OFC), collocated National Fiber Optic Engineers Conference, 2010 Conference on (OFC/NFOEC)*, 2010, pp.

1-3.

[43] C. Chang-Soon, *et al.*, "60-GHz bidirectional radio-on-fiber links based on InP-InGaAs HPT optoelectronic mixers," *Photonics Technology Letters, IEEE,* vol. 17, pp. 2721-2723, 2005.

[44] S. A. Malyshev and A. L. Chizh, "p-i-n Photodiodes for Frequency Mixing in Radio-Over-Fiber Systems," *Lightwave Technology, Journal of,* vol. 25, pp. 3236-3243, 2007.

[45] F. Paresys, *et al.*, "Low cost bidirectionnal QPSK transmission with optical frequency conversion," in *Microwave Photonics, 2009. MWP '09. International Topical Meeting on*, 2009, pp. 1-4.

[46] Y. C. Chung, "Recent advancement in WDM PON technology," in *2011 European Conference and Exhibition on Optical Communication*, Geneva, 2011, pp. 1-3.

[47] M. Pearson, "A Viable Alternative for Next Generation FTTP," *FTTH Prisim Magazine,* 2010.

[48] C. Chow, *et al.*, "13 Gbit/s WDM-OFDM PON using RSOA-based colourless ONU with seeding light source in local exchange," *Electronics Letters,* vol. 47, pp. 1235-1236, 2011.

[49] J. J. V. Olmos, *et al.*, "Fully-interleaved WDM reconfigurable baseband (2.5-Gbit/s) and 60-GHz (155-Mbit/s) millimeter-wave-band radio-over-fiber access network," in *Optical Communication, 2008. ECOC 2008. 34th European Conference on*, 2008, pp. 1-2.

[50] K. Prince, *et al.*, "Converged Wireline and Wireless Access Over a 78-km Deployed Fiber Long-Reach WDM PON," *Ieee Photonics Technology Letters,* vol. 21, pp. 1274-1276, Sep 2009.

[51] P. Tien-Thang, *et al.*, "A WDM-PON-Compatible System for Simultaneous Distribution of Gigabit Baseband and Wireless Ultrawideband Services With Flexible Bandwidth Allocation," *Photonics Journal, IEEE,* vol. 3, pp. 13-19, 2011.

[52] K. Hyun-Seung, *et al.*, "Simultaneous Wired and Wireless 1.25-Gb/s Bidirectional WDM-RoF Transmission Using Multiple Optical Carrier Suppression in FP LD," *Lightwave Technology, Journal of,* vol. 27, pp. 2744-2750, 2009.

[53] J. J. Vegas Olmos, *et al.*, "Reconfigurable 2.5-Gb/s Baseband and 60-GHz (155-Mb/s) Millimeter-Waveband Radio-Over-Fiber (Interleaving) Access Network," *Lightwave Technology, Journal of,* vol. 26, pp. 2506-2512, 2008.

[54] H. Ming-Fang, *et al.*, "Integration of RoF with WDM-PON for lightwave centralized access networks," in *OptoeElectronics and Communications Conference (OECC), 2011 16th*, 2011, pp. 387-388.

[55] T. Kuri, *et al.*, "Radio over fiber: DWDM-based analog/digital access networking and its enabling technologies," in *Radio and Wireless Symposium, 2008 IEEE*, 2008, pp. 137-140.

[56] J. J. Vegas Olmos, *et al.*, "Reconfigurable Radio-Over-Fiber Networks: Multiple-Access Functionality Directly Over the Optical Layer," *Microwave*

Theory and Techniques, IEEE Transactions on, vol. 58, pp. 3001-3010, 2010.

[57] Y. T. Hsueh*, et al.*, "A novel bidirectional 60-GHz radio-over-fiber scheme with multiband signal generation using a single intensity modulator," *Photonics Technology Letters, IEEE,* vol. 21, pp. 1338-1340, 2009.

[58] J. Yu*, et al.*, "Broadband convergence of 60-GHZ ROF and WDM-PON systems with a single modulator for bidirectional access networks," in *ECOC*, 2009, pp. 1-2.

[59] J. Zhensheng*, et al.*, "Simultaneous Generation of Independent Wired and Wireless Services Using a Single Modulator in Millimeter-Wave-Band Radio-Over-Fiber Systems," *Photonics Technology Letters, IEEE,* vol. 19, pp. 1691-1693, 2007.

Chapter 2

Investigation of the phase noise impact in optical heterodyning system using WDM Demultiplexer

2.1 Introduction

As we said in Chapter 1, WDM-RoF networks are proposed to perform mmW transmission into WDM-PON infrastructure. In WDM-PON architecture, a commercial WDM demultiplexer (DEMUX) is used to select each optical tone to a dedicated optical channel. From the viewpoint of coherent heterodyning technique, each BS needs to be addressed with the 2 coherent optical tones. Synthesizing these two techniques, it is a natural design for WDM-RoF that each BS is addressed with 2 optical tones in two different optical channels in purpose of coherent heterodyning. As in [1], the experiment has been conducted using super continuum (SC) light source, with a frequency interval between the optical spectral lines of 25 GHz. The WDM device has been employed to select two optical subcarriers with 50 GHz frequency interval to address the dedicated BS.

The phase noise issue leads to significant impact to digital signals [2]. Particularly, phase noise issue becomes the primal impairment for high spectral efficiency systems, such as OFDM systems [3]. According to different 60 GHz wireless standards, such as IEEE 802.15.3c, ECMA 387, WiGig, the OFDM modulation is supported without any exception. Hence, phase noise becomes the key issue in the 60 GHz RoF technique.

To avoid the phase noise induced from the optic to electric conversion, the optical tones which are used for photodetection should possess the same phase jitter. For example, the SC light source emits multi optical sub-carrier, which are coherent. Phase noise measurements have shown that optical self-heterodyning could provide low noise mmW [1, 4]. Nevertheless, a particular attention has to be paid to the coherent heterodyning system using WDM DEMUX because of the coherent nature of this

experiment scheme in [1, 5-7] due to the different optical paths between optical filter and coupler [8]. Indeed, the difference between the paths carrying the 2 beating optical tones may cause parasitic optical phase to intensity noise conversion, which may lead to significant increase of mmW phase noise [9]. Although this phase noise impact on the optically generated continuous wave (CW) RF signal induced by the optical paths mismatch has been presented before [8, 10, 11], no theoretical investigations on quantification of digitally modulated mmW phase noise degradation by optical self-heterodyning scheme and related impact on the digital signal error vector magnitude (EVM) have ever been carried out.

In this chapter, we propose, for the first time to our knowledge, a comprehensive study of phase noise degradation in optical self-heterodyning system using WDM DEMUX and related impact on digital signal EVM. The chapter is organized as follows. In section 2.2, theoretical approach for laser phase to intensity noise conversion is presented. In addition, the phase noise induced by the electrical generator employed to generate DSB-SC lightwave has been included in the theoretical model. Furthermore, a theoretical approach to quantify EVM degradation of digital mmW as a function of the optically generated phase noise is performed based on the study of optical phase to intensity conversion. In section 2.3, phase noise measurements of the optically generated mmW signal have been performed and compared with the theoretical results.

2.2 Theoretical analysis of the optical mmW phase noise

2.2.1 Investigation of the optical phase to intensity noise conversion

Fig. 2.1 shows the principle of the optical mmW generation based on optical self-heterodyning. In the central station (CS), a dual-arm Mach-Zehnder modulator (MZM #1), which is biased at minimum transmission and driven by a CW signal with the frequency f_{LO} from an electrical local oscillator (LO), is employed to generate two optical tones with the interval frequency of $2f_{LO}$. The modulated optical wave is then amplified by the Erbium Doped Fiber Amplifier (EDFA) and sent into the DEMUX, which is employed to select the specific spectral line to each optical channel. Therefore

the two optical tones, separated by $2f_{LO}$, are divided in two optical links. One optical tone (Channel #1) is modulated with another CW signal at intermediate frequency (IF) f_{IF} from IF generator using a MZM (MZM#2). The two optical channels are combined and transmitted to the BS for photodetection.

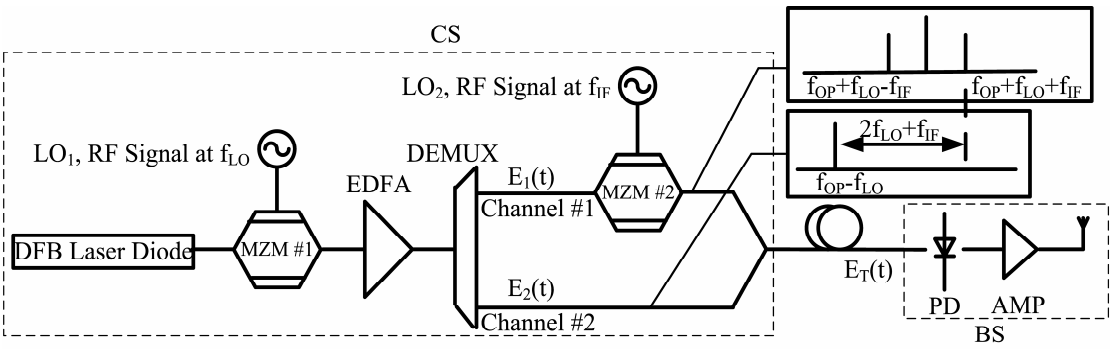

Fig. 2.1. Principle of the optical self-heterodyning mmW generation

2.2.1.1 Optical frequency conversion

We suppose that the optical field at the output of the DFB laser diode $E_{LD}(t)$ is modeled as a quasi-monochromatic amplitude-stabilized field with a phase fluctuation. The optical field of the laser is expressed as

$$E_{LD}(t) = E_{OP} \exp\left[j\left(2\pi f_{OP} t + \phi_{OP}(t)\right)\right] \tag{2.1}$$

where E_{OP} is the amplitude of the optical wave, f_{OP} is the central frequency of the optical carrier corresponding to 1550 nm central wavelength, $\phi_{OP}(t)$ is the optical phase jitter.

We suppose that the LO and IF generators deliver voltages expressed as

$$\begin{aligned} V_{LO}(t) &= V_{LO} \cos\left(2\pi f_{LO} t + \phi_{LO}(t)\right) \\ V_{IF}(t) &= V_{IF} \cos\left(2\pi f_{IF} t + \phi_{IF}(t)\right) \end{aligned} \tag{2.2}$$

where V_{LO} and V_{IF} are the voltage amplitude of LO and IF respectively, $\phi_{LO}(t)$ $\phi_{IF}(t)$ are the phase jitter of LO and IF respectively. By using (2.1) and (2.2), the output optical field of the dual-arm MZM (MZM #1) is expressed as :

$$\begin{aligned} E_{MZM\#1}(t) &= \frac{1}{2} E_{LD}(t) \times \left\{ \exp\left(j\pi \frac{V_{DC} + V_{LO}(t)}{2V_\pi} \right) + \exp\left(-j\pi \frac{V_{DC} + V_{LO}(t)}{2V_\pi} \right) \right\} \\ &= E_{OP} \exp\left[j\left(2\pi f_{OP} t + \phi_{OP}(t)\right)\right] \cos\left(\pi \frac{V_{DC} + V_{LO} \cos\left(2\pi f_{LO} t + \phi_{LO}(t)\right)}{2V_\pi} \right) \end{aligned} \tag{2.3}$$

where $E_{MZM\#1}(t)$ is the output optical field of MZM #1 (Fig. 2.1), V_π is the half-wave voltage of the MZM #1, V_{DC} is the biased voltage applied to MZM #1.

Since MZM #1 is biased at minimum of transmission ($V_{DC} = V_\pi$), equation (2.3) is derived as

$$E_{MZM\#1}(t) = -E_{OP}\exp\left[j\left(2\pi f_{OP}t + \phi_{OP}(t)\right)\right]\sin\left(\pi\frac{V_{LO}\cos\left(2\pi f_{LO}t + \phi_{LO}(t)\right)}{2V_\pi}\right) \quad (2.4)$$

Here the half wave voltage of the MZM #1 (V_π) is around 5V. The amplitude voltage of LO (V_{LO}) is 0.9 V, which corresponds to 12dBm output power of LO. Since the RF signal from LO is small signal compared to the half wave voltage of MZM #1, equation (2.4) can be derived as

$$\begin{aligned}
&E_{MZM\#1}(t) \approx -\pi\frac{V_{LO}}{2V_\pi}E_{OP}\exp\left[j\left(2\pi f_{OP}t + \phi_{OP}(t)\right)\right]\cos\left(2\pi f_{LO}t + \phi_{LO}(t)\right)\\
&= -\pi\frac{V_{LO}}{4V_\pi}E_{OP}\exp\left[j\left(2\pi f_{OP}t + \phi_{OP}(t)\right)\right]\bullet\\
&\left\{\exp\left[j\left(2\pi f_{LO}t + \phi_{LO}(t)\right)\right] + \exp\left[j\left(-2\pi f_{LO}t - \phi_{LO}(t)\right)\right]\right\} \quad (2.5)\\
&= -\pi\frac{V_{LO}}{4V_\pi}E_{OP}\left\{\exp\left[j\left(2\pi\left(f_{OP} + f_{LO}\right)t + \phi_{OP}(t) + \phi_{LO}(t)\right)\right] + \right.\\
&\left.\exp\left[j\left(2\pi\left(f_{OP} - f_{LO}\right)t + \phi_{OP}(t) - \phi_{LO}(t)\right)\right]\right\}
\end{aligned}$$

2.2.1.2 mmW generation

Equation (2.5) shows that the output lightwave of MZM #1 contains two spectral lines with the frequency interval of $2f_{LO}$, which are selected by different WDM channels using the DEMUX (Fig. 1). The optical wave in one channel is modulated by another dual-arm MZM (MZM #2), which is biased in linear regime ($V_{DC} = 0.5V_\pi$). In the BS, the received optical field contains mainly four spectral lines at the frequencies of f_{OP} - f_{LO}, f_{OP} + f_{LO}, f_{OP} + f_{LO} + f_{IF} and f_{OP} + f_{LO} - f_{IF}. There is a time delay τ_d, which corresponds to the optical path difference ΔL between channels #1 and #2 before recombination, where $\Delta L = c\tau_d/n$ (c is light velocity in vacuum, n is the effective index in the optical fiber). Here we only consider the beating of the two spectral lines at frequencies f_{OP} - f_{LO} and f_{OP} + f_{LO} + f_{IF} for the desired mmW generation. The two optical tones are expressed as

$$
\begin{aligned}
E_1(t) &= E_1 \exp\Big[j\big(2\pi\big(f_{OP}+f_{LO}+f_{IF}\big)\big(t+\tau_d\big)+ \\
&\phi_{OP}\big(t+\tau_d\big)+\phi_{LO}\big(t+\tau_d\big)+\phi_{IF}\big(t+\tau_d\big)\big)\Big] \\
E_2(t) &= E_2 \exp\Big[j\big(2\pi\big(f_{OP}-f_{LO}\big)t+\phi_{OP}(t)-\phi_{LO}(t)\big)\Big]
\end{aligned}
\tag{2.6}
$$

where E_1 and E_2 are the amplitudes of the two optical spectral lines respectively. Since the coherence time of the LO generator is much longer than the one of the DFB laser, the impact of delay τ_d on the RF signals can be ignored ($\phi_{LO}(t+\tau_d)= \phi_{LO}(t)$, $\phi_{IF}(t+\tau_d)= \phi_{IF}(t)$).

The photocurrent at the PD output ($I(t)$) can be calculated as

$$
\begin{aligned}
&I(t) = R\big(E_1(t)+E_2(t)\big)\big(E_1(t)+E_2(t)\big)^* \\
&= R\Big(E_1^2+E_2^2+2E_1E_2\cos\big(2\pi\big(2f_{LO}+f_{IF}\big)t+2\pi\big(f_{LO}+f_{IF}+f_{OP}\big)\tau_d+\phi_{mmW}(t)\big)\Big)
\end{aligned}
$$

with

$$
\phi_{mmW}(t) = \Delta\phi_{OP}(t,\tau_d)+\phi_{RF}(t)
$$

where

$$
\begin{aligned}
\Delta\phi_{OP}(t,\tau_d) &= \phi_{OP}\big(t+\tau_d\big)-\phi_{OP}(t) \\
\phi_{RF}(t) &= \phi_{IF}\big(t+\tau_d\big)+\phi_{LO}\big(t+\tau_d\big)+\phi_{LO}(t) \approx 2\phi_{LO}(t)+\phi_{IF}(t)
\end{aligned}
\tag{2.7}
$$

where R represents the responsivity of the PD. $\phi_{mmW}(t)$ is the total phase jitter of the photocurrent, which includes the electrical phase jitter induced by the two electrical generators and $\Delta\phi_{op}(t,\tau)$ which represents the random optical phase change between t and $t+\tau_d$. $2\pi(f_{OP}+f_{LO}+f_{IF})\tau_d$ represents a constant phase shift, which can be discarded. Since we only focus on the mmW, the DC component, which is represented in the first term of (2.7), is discarded during the following theoretical analysis. The mmW is expressed as:

$$
I_{mmW}(t) = 2E_1E_2\cos\big(2\pi\big(2f_{LO}+f_{IF}\big)t+2\pi\big(f_{LO}+f_{IF}+f_{OP}\big)\tau_d+\phi_{mmW}(t)\big) \tag{2.8}
$$

2.2.1.3 autocorrelation function of the mmW

To theoretically analyze the mmW, it is necessary to calculate the power spectrum density (PSD), which can be obtained by using the Fourier Transform of its autocorrelation function.

The autocorrelation function of the mmW ($R_{mmW}(\tau)$) in (2.8) is expressed as

$$
\begin{aligned}
&R_{mmW}(\tau) = \left\langle I_{mmW}(t) I^{*}_{mmW}(t+\tau) \right\rangle \\
&= R^2 (E_1 E_2)^2 \left(CC + CC^{*} \right) \\
&CC = \exp\left(j2\pi (2 f_{LO} + f_{IF}) \tau \right) \times \left\langle \exp j\Delta\phi_{mmW}(t,\tau) \right\rangle \\
&\Delta\phi_{mmW}(t,\tau) = \phi_{mmW}(t+\tau) - \phi_{mmW}(t)
\end{aligned}
\tag{2.9}
$$

where $\Delta\phi_{mmW}(t,\tau)$ represents the random phase change between t and $t+\tau$. $\langle\cdot\rangle$ in (2.9) can be represented by the mean value over infinite time (stationary ergodic process)

$$
\left\langle f(x) \right\rangle = \lim_{T\to\infty} \frac{1}{T} \int_{-\infty}^{+\infty} f(x)\, dx \tag{2.10}
$$

Since the random phase change of the mmW includes the optical phase noise and electrical phase noise, which are totally uncorrelated, $\langle exp(j\Delta\phi_{mmW}(t,\tau)) \rangle$ in the CC term (2.9) of the mmW autocorrelation function (2.9) can be developed as

$$
\begin{aligned}
&\left\langle \exp j\left(\Delta\phi_{mmW}(t,\tau) \right) \right\rangle = \left\langle \exp j\left(2\Delta\phi_{LO}(t,\tau) \right) \right\rangle \times \\
&\left\langle \exp j\left(\Delta\phi_{IF}(t,\tau) \right) \right\rangle \times \left\langle \exp j\left(\Delta\phi_{OP}(t+\tau,\tau_d) - \Delta\phi_{OP}(t,\tau_d) \right) \right\rangle
\end{aligned}
$$

where

$$
\begin{aligned}
&\Delta\phi_{LO}(t,\tau) = \phi_{LO}(t+\tau) - \phi_{LO}(t) \\
&\Delta\phi_{IF}(t,\tau) = \phi_{IF}(t+\tau) - \phi_{IF}(t)
\end{aligned}
\tag{2.11}
$$

The random phase changes $\Delta\phi_{OP}(t,\tau_d)$, $\Delta\phi_{OP}(t+\tau,\tau_d)$, $\Delta\phi_{LO}(t,\tau)$ and $\Delta\phi_{IF}(t,\tau)$ in (2.11) contain white noise components and 1/f components. The white noise components are commonly assumed to be zero-mean stationary Gaussian random processes [12, 13]. The 1/f components of these phase jitters are also stationary and exhibit Gaussian statistics even though the phase and frequency jitter $\phi_{OP}(t)$, $\phi_{LO}(t)$ and $\phi_{IF}(t)$ due to 1/f component are not stationary [12]. As a consequence, the random phase change of the mmW $\Delta\phi_{mmW}(t,\tau)$ is assumed to be a zero-mean stationary Gaussian random process respectively, the probability density function $W(\Delta\phi_{mmW}(t,\tau))$ of which is defined as

$$
\begin{aligned}
&\Delta\phi_{mmW}(\tau) = \Delta\phi_{mmW}(t,\tau) = \phi_{mmW}(t+\tau) - \phi_{mmW}(t) \\
&W\left(\Delta\phi_{mmW}(\tau) \right) = \frac{1}{\sqrt{2\pi\sigma^2_{\Delta\phi_{mmW}}(\tau)}} \exp\left[-\frac{\Delta\phi^2_{mmW}(\tau)}{2\sigma^2_{\Delta\phi_{mmW}}(\tau)} \right]
\end{aligned}
\tag{2.12}
$$

Since $\Delta\phi_{mmW}(t,\tau)$ follows Gaussian distribution, there is the following well known relation:

$$\left\langle \exp\left[\pm j\Delta\phi_{mmW}(t,\tau)\right]\right\rangle = \exp\left[-\frac{1}{2}\sigma^2_{\Delta\phi_{mmW}}(\tau)\right] \tag{2.13}$$

Using (2.13), the autocorrelation function of the mmW can be derived as

$$R_{mmW}(\tau) = 2R^2E_1^2E_2^2\cos\left(2\pi\left(2f_{LO}+f_{IF}\right)\tau\right)\exp\left[-\frac{1}{2}\sigma^2_{\Delta\phi_{mmW}}(\tau)\right] \tag{2.14}$$

where $\sigma^2_{\Delta\phi mmW}(\tau)$ is the variance of the random mmW phase change between t and $t+\tau$. The variance of the phase change $\sigma^2_{\Delta\phi mmW}(\tau)$ could be derived as

$$\begin{aligned}
&\sigma^2_{\Delta\phi_{mmW}}(\tau) = E\left[\left(\Delta\phi_{mmW}(\tau) - E\left(\Delta\phi_{mmW}(\tau)\right)\right)^2\right] \\
&= E\left[\left(\Delta\phi_{mmW}(\tau)\right)^2\right] \\
&= E\left[\left(2\Delta\phi_{LO}(t,\tau) + \Delta\phi_{IF}(t,\tau) + \Delta\phi_{OP}(t+\tau,\tau_d) - \Delta\phi_{OP}(t,\tau_d)\right)^2\right] \\
&= E\left[4\Delta\phi^2_{LO}(t,\tau) + \Delta\phi^2_{IF}(t,\tau) + \left(\Delta\phi_{OP}(t+\tau,\tau_d) - \Delta\phi_{OP}(t,\tau_d)\right)^2 + 4\Delta\phi_{LO}(t,\tau)\Delta\phi_{IF}(t,\tau) + \right. \\
&\left. 4\Delta\phi_{LO}(t,\tau)\left(\Delta\phi_{OP}(t+\tau,\tau_d) - \Delta\phi_{OP}(t,\tau_d)\right) + 2\Delta\phi_{IF}(t,\tau)\left(\Delta\phi_{OP}(t+\tau,\tau_d) - \Delta\phi_{OP}(t,\tau_d)\right)\right]
\end{aligned} \tag{2.15}$$

where $E(\cdot)$ is the mathematical expectation.

Since the random mmW phase change between t and $t+\tau$ contains optical phase change contribution and RF signal phase change contribution, which are totally independent, the variance of $\Delta\phi_{mmW}(t,\tau)$ in (2.14) can be developed as

$$\begin{aligned}
&\sigma^2_{\Delta\phi_{mmW}}(\tau) = 4E\left[\Delta\phi^2_{LO}(t,\tau)\right] + E\left[\Delta\phi^2_{IF}(t,\tau)\right] + E\left[\left(\Delta\phi_{OP}(t+\tau,\tau_d) - \Delta\phi_{OP}(t,\tau_d)\right)^2\right] + \\
&4E\left[\Delta\phi_{LO}(t,\tau)\right]E\left[\Delta\phi_{IF}(t,\tau)\right] + 4E\left[\Delta\phi_{LO}(t,\tau)\right]E\left[\left(\Delta\phi_{OP}(t+\tau,\tau_d) - \Delta\phi_{OP}(t,\tau_d)\right)\right] + \\
&2E\left[\Delta\phi_{IF}(t,\tau)\right]E\left[\left(\Delta\phi_{OP}(t+\tau,\tau_d) - \Delta\phi_{OP}(t,\tau_d)\right)\right] \\
&= 4E\left(\Delta\phi^2_{LO}(t,\tau)\right) + E\left(\Delta\phi^2_{IF}(t,\tau)\right) + E\left[\left(\Delta\phi_{OP}(t+\tau,\tau_d) - \Delta\phi_{OP}(t,\tau_d)\right)^2\right]
\end{aligned} \tag{2.16}$$

From (2.16), it is obvious that the variance of the mmW phase change $\sigma^2_{\Delta\phi mmW}(\tau)$ is composed of three parts: variance of the RF signal phase change from LO, variance of the IF signal phase change and optical phase change contribution. The first and second term in (2.16) are exactly the variance of the phase jitter for RF and IF signal ($\sigma^2_{\Delta\phi LO}(\tau)$ and $\sigma^2_{\Delta\phi IF}(\tau)$) respectively. The last term in (2.16) could be derived as follows.

$$
\begin{aligned}
&E\left[\left(\Delta\phi_{OP}\left(t+\tau,\tau_d\right)-\Delta\phi_{OP}\left(t,\tau_d\right)\right)^2\right] \\
&=E\left[\Delta\phi_{OP}^2\left(t+\tau,\tau_d\right)+\Delta\phi_{OP}^2\left(t,\tau_d\right)-2\Delta\phi_{OP}\left(t+\tau,\tau_d\right)\Delta\phi_{OP}\left(t,\tau_d\right)\right] \\
&=\sigma_{\Delta\phi_{OP}}^2\left(\tau_d\right)+\sigma_{\Delta\phi_{OP}}^2\left(\tau_d\right)-2E\left[\Delta\phi_{OP}\left(t+\tau,\tau_d\right)\Delta\phi_{OP}\left(t,\tau_d\right)\right] \\
&=2\sigma_{\Delta\phi_{OP}}^2\left(\tau_d\right)-2E\left[\left(\phi_{OP}\left(t+\tau+\tau_d\right)-\phi_{OP}\left(t+\tau\right)\right)\left(\phi_{OP}\left(t+\tau_d\right)-\phi_{OP}\left(t\right)\right)\right] \\
&=2\sigma_{\Delta\varphi_{OP}}^2\left(\tau_d\right)-2E\left[\phi_{OP}\left(t+\tau+\tau_d\right)\phi_{OP}\left(t+\tau_d\right)-\phi_{OP}\left(t+\tau+\tau_d\right)\phi_{OP}\left(t\right)-\right. \\
&\left.\phi_{OP}\left(t+\tau\right)\phi_{OP}\left(t+\tau_d\right)+\phi_{OP}\left(t+\tau\right)\phi_{OP}\left(t\right)\right] \\
&=2\sigma_{\Delta\varphi_{OP}}^2\left(\tau_d\right)-2E\left[-\frac{1}{2}\left(\phi_{OP}\left(t+\tau+\tau_d\right)-\phi_{OP}\left(t+\tau_d\right)\right)^2+\frac{1}{2}\left(\phi_{OP}\left(t+\tau+\tau_d\right)-\phi_{OP}\left(t\right)\right)^2+\right. \\
&\left.\frac{1}{2}\left(\phi_{OP}\left(t+\tau\right)-\phi_{OP}\left(t+\tau_d\right)\right)^2-\frac{1}{2}\left(\phi_{OP}\left(t+\tau\right)-\phi_{OP}\left(t\right)\right)^2\right] \\
&=2\sigma_{\Delta\phi_{OP}}^2\left(\tau_d\right)+2\sigma_{\Delta\phi_{OP}}^2\left(\tau\right)-\sigma_{\Delta\phi_{OP}}^2\left(\tau+\tau_d\right)-\sigma_{\Delta\phi_{OP}}^2\left(\tau-\tau_d\right)
\end{aligned}
\tag{2.17}
$$

Substituting (2.17) into (2.16), the variance of the mmW phase change could be expressed as

$$
\sigma_{\Delta\phi_{mmW}}^2\left(\tau\right)=4\sigma_{\Delta\phi_{LO}}^2\left(\tau\right)+\sigma_{\Delta\phi_{IF}}^2\left(\tau\right)+2\sigma_{\Delta\phi_{OP}}^2\left(\tau_d\right)+2\sigma_{\Delta\phi_{OP}}^2\left(\tau\right)-\sigma_{\Delta\phi_{OP}}^2\left(\tau+\tau_d\right)-\sigma_{\Delta\phi_{OP}}^2\left(\tau-\tau_d\right) \tag{2.18}
$$

Hence, the autocorrelation function of the mmW is

$$
\begin{aligned}
&R_{mmW}\left(\tau\right)=2R^2E_1^2E_2^2\cos\left(2\pi\left(2f_{LO}+f_{IF}\right)\tau\right)\bullet \\
&\exp\left[-2\sigma_{\Delta\phi_{LO}}^2\left(\tau\right)-\frac{1}{2}\sigma_{\Delta\phi_{IF}}^2\left(\tau\right)-\sigma_{\Delta\phi_{OP}}^2\left(\tau_d\right)-\sigma_{\Delta\phi_{OP}}^2\left(\tau\right)+\frac{\sigma_{\Delta\phi_{OP}}^2\left(\tau-\tau_d\right)}{2}+\frac{\sigma_{\Delta\phi_{OP}}^2\left(\tau+\tau_d\right)}{2}\right]
\end{aligned}
\tag{2.19}
$$

Similarly, the autocorrelation function of the RF signal from LO and IF signal can be calculated as:

$$
\begin{aligned}
&R_{LO}(\tau)=\left\langle V_{LO}(t)V_{LO}^{*}(t+\tau)\right\rangle \\
&=\left\langle V_{LO}^{2}\cos\left(2\pi f_{LO}t+\phi_{LO}(t)\right)\cos\left(2\pi f_{LO}(t+\tau)+\phi_{LO}(t+\tau)\right)\right\rangle \\
&=\frac{1}{2}V_{LO}^{2}\left\langle\cos\left(2\pi f_{LO}\tau+\phi_{LO}(t+\tau)-\phi_{LO}(t)\right)+\cos\left(4\pi f_{LO}t+2\pi f_{LO}\tau+\phi_{LO}(t)+\phi_{LO}(t+\tau)\right)\right\rangle \\
&=\frac{1}{2}V_{LO}^{2}\left\{\left\langle\cos\left(2\pi f_{LO}\tau+\phi_{LO}(t+\tau)-\phi_{LO}(t)\right)\right\rangle+\left\langle\cos\left(4\pi f_{LO}t+2\pi f_{LO}\tau+\phi_{LO}(t)+\phi_{LO}(t+\tau)\right)\right\rangle\right\} \\
&=\frac{1}{2}V_{LO}^{2}\left\langle\cos\left(2\pi f_{LO}\tau+\Delta\phi_{LO}(t,\tau)\right)\right\rangle+0 \\
&=\frac{1}{4}V_{LO}^{2}\left\langle\exp\left(j\left(2\pi f_{LO}\tau+\Delta\phi_{LO}(t,\tau)\right)\right)+\exp\left(-j\left(2\pi f_{LO}\tau+\Delta\phi_{LO}(t,\tau)\right)\right)\right\rangle \\
&=\frac{1}{4}V_{LO}^{2}\left\{\exp\left(j2\pi f_{LO}\tau\right)\left\langle\exp\left(j\Delta\phi_{LO}(t,\tau)\right)\right\rangle+\exp\left(-j2\pi f_{LO}\tau\right)\left\langle\exp\left(-j\Delta\phi_{LO}(t,\tau)\right)\right\rangle\right\} \\
&=\frac{1}{4}V_{LO}^{2}\left\{\exp\left(j2\pi f_{LO}\tau\right)\exp\left[-\frac{1}{2}\sigma_{\Delta\phi_{LO}}^{2}(\tau)\right]+\exp\left(-j2\pi f_{LO}\tau\right)\exp\left[-\frac{1}{2}\sigma_{\Delta\phi_{LO}}^{2}(\tau)\right]\right\} \\
&=\frac{1}{2}V_{LO}^{2}\cos\left(2\pi f_{LO}\tau\right)\exp\left[-\frac{1}{2}\sigma_{\Delta\phi_{LO}}^{2}(\tau)\right] \\
&R_{IF}(\tau)=\frac{1}{2}V_{IF}^{2}\cos\left(2\pi f_{IF}\tau\right)\exp\left[-\frac{1}{2}\sigma_{\Delta\phi_{IF}}^{2}(\tau)\right]
\end{aligned}
\tag{2.20}
$$

Generally, the variance of the random phase change could be expressed as the following equation by the definition of variance [14].

$$
\begin{aligned}
&\sigma_{\Delta\phi}^{2}(\tau)=E\left(\left(\phi(t+\tau)-\phi(t)\right)^{2}\right) \\
&=E\left(\phi^{2}(t+\tau)\right)+E\left(\phi^{2}(t)\right)-2E\left(\phi(t+\tau)\phi(t)\right) \\
&=\left\langle\phi(t+\tau)\phi(t+\tau)\right\rangle+\left\langle\phi(t)\phi(t)\right\rangle-2\left\langle\phi(t)\phi(t+\tau)\right\rangle \\
&=R_{\phi}(0)+R_{\phi}(0)-2R_{\phi}(\tau) \\
&=2R_{\phi}(0)-2R_{\phi}(\tau)
\end{aligned}
\tag{2.21}
$$

where $R_{\phi}(\tau)$ is the autocorrelation function of a signal phase jitter $\phi(t)$. The power spectrum density (PSD) of the phase jitter $\phi(t)$ is expressed as the Fourier Transform of the autocorrelation function of the phase jitter:

$$
\begin{aligned}
&R_{\phi}(\tau)=\frac{1}{2\pi}\int_{-\infty}^{+\infty}S_{\phi}(\omega)\exp\left(j\omega\tau\right)d\omega \\
&=\frac{1}{2\pi}\int_{-\infty}^{+\infty}S_{\phi}(\omega)\cos\left(\omega\tau\right)d\omega \qquad\qquad S_{\phi}(\omega)\text{ and }R_{\phi}(\tau)\text{ are real function}
\end{aligned}
\tag{2.22}
$$

where $S_{\phi}(\omega)$ is the PSD of the signal phase jitter. From the original definition, frequency

fluctuation $f(t)$ is the derivate of the phase jitter $\phi(t)$. Derivate in time domain corresponds to multiplication by $j\omega$ in frequency domain. As consequence the Fournier Transform of the phase jitter is expressed as.

$$F_f(\omega) = j\omega F_\phi(\omega) \tag{2.23}$$

where $F_f(\omega)$ and $F_\phi(\omega)$ are the Fournier Transform of frequency fluctuation and phase jitter respectively.

Hence, the relationship between PSD of phase jitter and PSD of frequency fluctuation is [14]

$$\begin{aligned} S_\phi(\omega) &= \left|F_\phi(\omega)\right|^2 = \frac{\left|F_f(\omega)\right|^2}{\omega^2} \\ &= \frac{S_f(\omega)}{\omega^2} \end{aligned} \tag{2.24}$$

where $S_f(\omega)$ and $S_\phi(\omega)$ are the PSD of phase jitter and PSD of frequency fluctuation respectively.

The variance of the random phase change ($\sigma_{\Delta\phi}^2(\tau)$) between t and $t+\tau$ is related to the power spectral density (PSD) of the instantaneous angular frequency fluctuation $S_f(\omega)$ as the following equation by substituting (2.22) and (2.24) into (2.21)

$$\sigma_{\Delta\phi}^2(\tau) = \frac{\tau^2}{2\pi}\int_{-\infty}^{+\infty}\left(\frac{\sin\left(\frac{\omega\tau}{2}\right)}{\frac{\omega\tau}{2}}\right)^2 S_f(\omega)\,d\omega \tag{2.25}$$

Here we would like to insist on the fact that all the equations up to here are derived under the general cases. The conclusions validate both for phase jitter due to the white noise component and phase jitter induced by 1/f noise component. In order to derive the autocorrelation function of the optical mmW and further probe the PSD of the optical mmW, we need some additional assumptions.

As it is discussed above, the random phase change between t and $t+\tau$ ($\Delta\phi(\tau)$) is due to white frequency noise and 1/f frequency noise [12]. The PSD of the signal is found by Fourier Transform of the autocorrelation function. Therefore, the resulting PSD is the convolution of the PSD due to the white frequency noise contribution and PSD associated with the 1/f frequency noise contribution [12]. In normal case ($\tau_d \neq 0$) the

dominant phase noise is induced by the optical phase to intensity noise conversion. In other words, the optical phase to intensity noise conversion is much higher than the phase noise induced by the electrical generator in normal case ($|\tau_d| \neq 0$). Therefore the 1/f noise from the electrical generator is not very important to take into account. Regarding the optical phase to intensity noise conversion, in [12], it is indicated that 1/f noise contribution in the final linewidth measurement (taking into account 1/f noise and white noise) is negligible for short delay, low power heterodyning systems (Fig. 6 and Fig. 8 and first paragraph of section VII from [12]). It is also shown in [12] that *1/f* noise can have significant impact for high power laser applications, which is not the case in our system. Synthesizing these two reasons, we simply ignored the *1/f* noise contribution in the theoretical analysis before investigating its impact in the experimental analysis. The instantaneous frequency fluctuation here is considered as white noise for both laser source and electrical generators, which means that the PSD of the frequency fluctuation for laser source or electrical generator is a constant ($S_f(\omega)=C$), the variance of the random phase change between τ delay ($\sigma_{\Delta\phi}^2(\tau)$) in (2.24) is derived as

$$\begin{aligned}\sigma_{\Delta\phi}^2(\tau) &= \frac{\tau^2}{2\pi}\int_{-\infty}^{+\infty}\left(\frac{\sin\left(\frac{\omega\tau}{2}\right)}{\frac{\omega\tau}{2}}\right)^2 S_f(\omega)\,d\omega \\ &= \frac{\tau^2 C}{2\pi}\int_{-\infty}^{+\infty}\left(\frac{\sin\left(\frac{\omega\tau}{2}\right)}{\frac{\omega\tau}{2}}\right)^2 d\omega\end{aligned} \tag{2.26}$$

$F(\omega) = \sin(\omega\tau/2)/(\omega\tau/2)$ is the Fourier transform of the Rectangle function shown in Fig. 2.2.

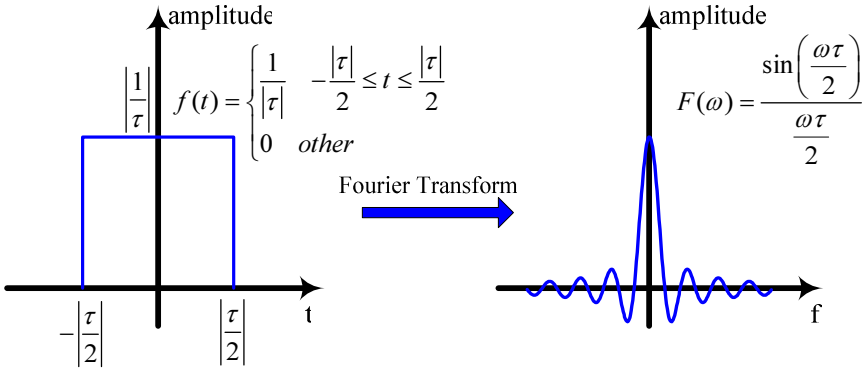

Fig. 2.2. Fourier transform of the rectangle function

The integral in (2.25) can be derived by using Parseval's equation.

$$\int_{-\infty}^{+\infty}\left(\frac{\sin\left(\frac{\omega\tau}{2}\right)}{\frac{\omega\tau}{2}}\right)^2 d\omega = 2\pi\int_{-\frac{|\tau|}{2}}^{+\frac{|\tau|}{2}}\left(\frac{1}{|\tau|}\right)^2 dt = \frac{2\pi}{|\tau|} \tag{2.27}$$

Substitute (2.27) into (2.26), the variance of the phase jitter is derived as

$$\begin{aligned}\sigma_{\Delta\phi}^2(\tau) &= \frac{\tau^2 C}{2\pi}\frac{2\pi}{|\tau|} = 2\gamma|\tau| \\ 2\gamma &= \frac{1}{\tau_c}\end{aligned} \tag{2.28}$$

where 2γ is the angular full linewidth at half maximum (FWHM) of the signal (laser source or pure RF signal) spectrum, τ_c is the coherence time of the source.

Therefore, the variances of the random phase changes of the LO signal and IF signal are expressed as

$$\begin{aligned}\sigma_{\Delta\phi_{LO}}^2(\tau) &= 2\gamma_{LO}|\tau| \\ \sigma_{\Delta\phi_{IF}}^2(\tau) &= 2\gamma_{IF}|\tau|\end{aligned} \tag{2.29}$$

where $2\gamma_{LO}$ and $2\gamma_{IF}$ are the linewidth at half maximum of the LO signal and IF signal respectively. Moreover, mmW between t and $t+\tau$ are expressed as follows by using (2.28) and (2.18).

$$\sigma^2_{\Delta\phi_{mmW}}(\tau) = 4\sigma^2_{\Delta\phi_{LO}}(\tau) + \sigma^2_{\Delta\phi_{IF}}(\tau) + 2\sigma^2_{\Delta\phi_{OP}}(\tau_d) + 2\sigma^2_{\Delta\phi_{OP}}(\tau) - \sigma^2_{\Delta\phi_{OP}}(\tau+\tau_d) - \sigma^2_{\Delta\phi_{OP}}(\tau-\tau_d)$$
$$= 4\sigma^2_{\Delta\phi_{LO}}(\tau) + \sigma^2_{\Delta\phi_{IF}}(\tau) + 4\gamma_{OP}|\tau_d| + 4\gamma_{OP}|\tau| - 2\gamma_{OP}|\tau+\tau_d| - 2\gamma_{OP}|\tau-\tau_d|$$
$$= \begin{cases} 2(4\gamma_{LO}+\gamma_{IF})|\tau| + 4\gamma_{OP}|\tau| & |\tau| \le |\tau_d| \\ 2(4\gamma_{LO}+\gamma_{IF})|\tau| + 4\gamma_{OP}|\tau_d| & |\tau| > |\tau_d| \end{cases}$$
$$2\gamma_{OP} = \frac{1}{\tau_{cOP}}$$

(2.30)

where $2\gamma_{OP}$ is the linewidth at half maximum of the laser source, τ_{cOP} is the coherence time of the laser source. The autocorrelation function of the mmW, LO signal and IF signal are derived by substituting (2.29) and (2.30) into (2.19) and (2.20).

$$R_{mmW}(\tau) = \begin{cases} 2R^2E_1^2E_2^2\cos(2\pi(2f_{LO}+f_{IF})\tau)\exp(-2\gamma_{OP}|\tau| - (4\gamma_{LO}+\gamma_{IF})|\tau|) & |\tau| \le |\tau_d| \\ 2R^2E_1^2E_2^2\cos(2\pi(2f_{LO}+f_{IF})\tau)\exp(-2\gamma_{OP}|\tau_d| - (4\gamma_{LO}+\gamma_{IF})|\tau|) & |\tau| > |\tau_d| \end{cases}$$
$$R_{LO}(\tau) = \frac{V_{LO}^2}{2}\cos(2\pi f_{LO}\tau)\exp[-\gamma_{LO}|\tau|]$$
$$R_{IF}(\tau) = \frac{V_{IF}^2}{2}\cos(2\pi f_{IF}\tau)\exp[-\gamma_{IF}|\tau|]$$

(2.31)

2.2.1.4 PSD of the mmW

The PSD of the mmW is derived by implementing the Fourier Transform of the mmW autocorrelation function shown in (2.31). The first term (cosine function) of the autocorrelation function of the mmW in (2.31) will transfer the PSD from baseband to the frequency $2f_{LO}+f_{IF}$. The second term of the optical mmW autocorrelation function (2.31) contains two components. One $\exp(-2\gamma_{OP}\tau)$ or $\exp(-2\gamma_{OP}\tau_d)$) is from the optical source, and the other ($\exp(-(4\gamma_{LO+}\gamma_{IF})\ \tau)$) is from the two electrical generators. Based on the properties of the Fourier Transform, the PSD of the mmW is the convolution of the PSD of these two components. The PSD of the component from electrical generators is easy to be derived as follows.

$$F\left(\exp\left(-(4\gamma_{LO}+\gamma_{IF})|\tau|\right)\right) = \frac{2(4\gamma_{LO}+\gamma_{IF})}{(4\gamma_{LO}+\gamma_{IF})^2 + (2\pi f)^2} \tag{2.32}$$

Now we focus on the Fourier Transform of the components from optical source.

$$f(\tau)=\begin{cases}\exp\left(-2\gamma_{OP}|\tau|\right) & |\tau|\le|\tau_d| \\ \exp\left(-2\gamma_{OP}|\tau_d|\right) & |\tau|>|\tau_d|\end{cases}$$

$$F\left(f(\tau)\right)=\int_{-\infty}^{\infty}f(\tau)\exp\left(-j2\pi f\tau\right)d\tau$$

$$=\int_{-\infty}^{-|\tau_d|}f(\tau)\exp\left(-j2\pi f\tau\right)d\tau+\int_{-|\tau_d|}^{|\tau_d|}f(\tau)\exp\left(-j2\pi f\tau\right)d\tau+\int_{|\tau_d|}^{\infty}f(\tau)\exp\left(-j2\pi f\tau\right)d\tau$$

$$=\int_{-\infty}^{-|\tau_d|}\exp\left(-2\gamma_{OP}|\tau_d|\right)\exp\left(-j2\pi f\tau\right)d\tau+\int_{|\tau_d|}^{\infty}\exp\left(-2\gamma_{OP}|\tau_d|\right)\exp\left(-j2\pi f\tau\right)d\tau+$$

$$\int_{-|\tau_d|}^{0}\exp\left(2\gamma_{OP}\tau\right)\exp\left(-j2\pi f\tau\right)d\tau+\int_{0}^{|\tau_d|}\exp\left(-2\gamma_{OP}\tau\right)\exp\left(-j2\pi f\tau\right)d\tau \tag{2.33}$$

By using the following equation:

$$\int_{-\infty}^{\infty}\exp\left(-j2\pi f\tau\right)d\tau=\delta(f) \tag{2.34}$$

the first and second term of (2.33) can be derived as:

$$\begin{aligned}&\int_{-\infty}^{-|\tau_d|}\exp\left(-2\gamma_{OP}|\tau_d|\right)\exp\left(-j2\pi f\tau\right)d\tau+\int_{|\tau_d|}^{\infty}\exp\left(-2\gamma_{OP}|\tau_d|\right)\exp\left(-j2\pi f\tau\right)d\tau \\ &=\int_{-\infty}^{-\infty}\exp\left(-2\gamma_{OP}|\tau_d|\right)\exp\left(-j2\pi f\tau\right)d\tau-\int_{-|\tau_d|}^{|\tau_d|}\exp\left(-2\gamma_{OP}|\tau_d|\right)\exp\left(-j2\pi f\tau\right)d\tau \\ &=\exp\left(-2\gamma_{OP}|\tau_d|\right)\delta(f)+\exp\left(-2\gamma_{OP}|\tau_d|\right)\frac{\exp\left(-j2\pi f\tau\right)}{j2\pi f}\Big|_{-|\tau_d|}^{|\tau_d|} \\ &=\exp\left(-2\gamma_{OP}|\tau_d|\right)\delta(f)-2\exp\left(-2\gamma_{OP}|\tau_d|\right)\frac{\sin\left(2\pi f|\tau_d|\right)}{2\pi f}\end{aligned} \tag{2.35}$$

The third and fourth term in (2.33) are derived as:

$$\begin{aligned}&\int_{-|\tau_d|}^{0}\exp\left(2\gamma_{OP}\tau\right)\exp\left(-j2\pi f\tau\right)d\tau+\int_{0}^{|\tau_d|}\exp\left(-2\gamma_{OP}\tau\right)\exp\left(-j2\pi f\tau\right)d\tau \\ &=\frac{\exp\left(\left(-j2\pi f+2\gamma_{OP}\right)\tau\right)}{-j2\pi f+2\gamma_{OP}}\Big|_{-|\tau_d|}^{0}+\frac{\exp\left(\left(-j2\pi f-2\gamma_{OP}\right)\tau\right)}{-j2\pi f-2\gamma_{OP}}\Big|_{0}^{|\tau_d|} \\ &=\frac{1-\exp\left(-\left(-j2\pi f+2\gamma_{OP}\right)|\tau_d|\right)}{-j2\pi f+2\gamma_{OP}}+\frac{\exp\left(\left(-j2\pi f-2\gamma_{OP}\right)|\tau_d|\right)-1}{-j2\pi f-2\gamma_{OP}} \\ &=-\frac{\left[1-\exp\left(-\left(-j2\pi f+2\gamma_{OP}\right)|\tau_d|\right)\right]\left(-j2\pi f-2\gamma_{OP}\right)}{4\gamma_{OP}^2+4\pi^2f^2}- \\ &\frac{\left[\exp\left(\left(-j2\pi f-2\gamma_{OP}\right)|\tau_d|\right)-1\right]\left(-j2\pi f+2\gamma_{OP}\right)}{4\gamma_{OP}^2+4\pi^2f^2} \\ &=\frac{4\gamma_{OP}+4\pi f\exp\left(-2\gamma_{OP}|\tau_d|\right)\sin\left(2\pi f|\tau_d|\right)-4\gamma_{OP}\exp\left(-2\gamma_{OP}|\tau_d|\right)\cos\left(2\pi f|\tau_d|\right)}{4\gamma_{OP}^2+4\pi^2f^2}\end{aligned} \tag{2.36}$$

Hence (2.33) can be derived by using (2.35) and (2.36).

$$
\begin{aligned}
&F\left(f\left(\tau\right)\right)=\exp\left(-2\gamma_{OP}\left|\tau_d\right|\right)\delta\left(f\right)-2\exp\left(-2\gamma_{OP}\left|\tau_d\right|\right)\frac{\sin\left(2\pi f\left|\tau_d\right|\right)}{2\pi f}+\\
&\frac{4\gamma_{OP}+4\pi f\exp\left(-2\gamma_{OP}\left|\tau_d\right|\right)\sin\left(2\pi f\left|\tau_d\right|\right)-4\gamma_{OP}\exp\left(-2\gamma_{OP}\left|\tau_d\right|\right)\cos\left(2\pi f\left|\tau_d\right|\right)}{4\gamma_{OP}^2+4\pi^2f^2}\\
&=\exp\left(-2\gamma_{OP}\left|\tau_d\right|\right)\delta\left(f\right)+\frac{4\gamma_{OP}}{4\gamma_{OP}^2+4\pi^2f^2}-\frac{4\gamma_{OP}\exp\left(-2\gamma_{OP}\left|\tau_d\right|\right)\cos\left(2\pi f\left|\tau_d\right|\right)}{4\gamma_{OP}^2+4\pi^2f^2}+\\
&\frac{-8\gamma_{OP}^2\exp\left(-2\gamma_{OP}\left|\tau_d\right|\right)}{\left(4\gamma_{OP}^2+4\pi^2f^2\right)}\frac{\sin\left(2\pi f\left|\tau_d\right|\right)}{2\pi f}\\
&=\exp\left(-2\gamma_{OP}\left|\tau_d\right|\right)\delta\left(f\right)+\frac{4\gamma_{OP}\exp\left(-2\gamma_{OP}\left|\tau_d\right|\right)}{4\gamma_{OP}^2+4\pi^2f^2}\bullet\\
&\left(\exp\left(2\gamma_{OP}\left|\tau_d\right|\right)-\cos\left(2\pi f\left|\tau_d\right|\right)-2\gamma_{OP}\frac{\sin\left(2\pi f\left|\tau_d\right|\right)}{2\pi f}\right)
\end{aligned}
\tag{2.37}
$$

As a consequence, the Fourier Transform of the autocorrelation function of mmW (PSD of mmW) is expressed as

$$
\begin{aligned}
&S_{mmW}=\left(F\left(2R^2E_1^2E_2^2\exp\left[-\left(4\gamma_{LO}+\gamma_{IF}\right)\left|\tau\right|\right]\right)*F\left(f\left(\tau\right)\right)\right)*F\left(\cos2\pi f_{mmW}\tau\right)\\
&=2R^2E_1^2E_2^2\frac{2\left(4\gamma_{LO}+\gamma_{IF}\right)}{\left(4\gamma_{LO}+\gamma_{IF}\right)^2+\left(2\pi f\right)^2}*\left\{\exp\left(-2\gamma_{OP}\left|\tau_d\right|\right)\delta\left(f-f_{mmW}\right)+\right.\\
&\left.\left(\exp\left(2\gamma_{OP}\left|\tau_d\right|\right)-\cos\left(2\pi\left(f-f_{mmW}\right)\left|\tau_d\right|\right)-2\gamma_{OP}\frac{\sin\left(2\pi\left(f-f_{mmW}\right)\left|\tau_d\right|\right)}{2\pi\left(f-f_{mmW}\right)}\right)\frac{4\gamma_{OP}\exp\left(-2\gamma_{OP}\left|\tau_d\right|\right)}{4\gamma_{OP}^2+4\pi^2\left(f-f_{mmW}\right)^2}\right\}
\end{aligned}
\tag{2.38}
$$

where $S_{mmW}(\omega)$ is the PSD of the optical mmW, $f_{mmW}=2f_{LO}+f_{IF}$, * indicates the convolution.

Similarly, the PSDs of the LO and IF signal can be derived by Fourier Transform of the LO and IF signal autocorrelation function in (2.31) as:

$$
\begin{aligned}
S_{LO}\left(\omega\right)&=\frac{V_{LO}^2}{2}\frac{\gamma_{LO}}{\gamma_{LO}^2+\left(2\pi\left(f-f_{LO}\right)\right)^2}\\
S_{IF}\left(\omega\right)&=\frac{V_{IF}^2}{2}\frac{\gamma_{IF}}{\gamma_{IF}^2+\left(2\pi\left(f-f_{IF}\right)\right)^2}
\end{aligned}
\tag{2.39}
$$

where $S_{LO}(\omega)$ and $S_{IF}(\omega)$ are the PSDs of the LO and IF signal respectively.

Based on the investigation of the mmW phase noise, we further simulate the PSD of the mmW.

(1) $|\tau_d|$ is large

When the optical delay $|\tau_d|$ is large compared to the laser coherence time τ_c, the narrowband electrical phase noise contribution to the PSD of the optical mmW (last term in equation (2.38)) could be ignored because it is convoluted by a large spectrum component from optical phase noise conversion. In this case ($|\tau_d| >> \tau_{cOP}$), the PSD of the optical mmW is simplified as

$$S_{mmW} = 2R^2 E_1^2 E_2^2 \left\{ \exp\left(-2\gamma_{OP}|\tau_d|\right)\delta\left(f - f_{mmW}\right) + \left(\exp\left(2\gamma_{OP}|\tau_d|\right) - \cos\left(2\pi\left(f - f_{mmW}\right)|\tau_d|\right) - 2\gamma_{OP}\frac{\sin\left(2\pi f|\tau_d|\right)}{2\pi\left(f - f_{mmW}\right)} \right) \frac{4\gamma_{OP}\exp\left(-2\gamma_{OP}|\tau_d|\right)}{4\gamma_{OP}^2 + 4\pi^2\left(f - f_{mmW}\right)^2} \right\} \quad |\tau_d| >> \tau_{cOP} \tag{2.40}$$

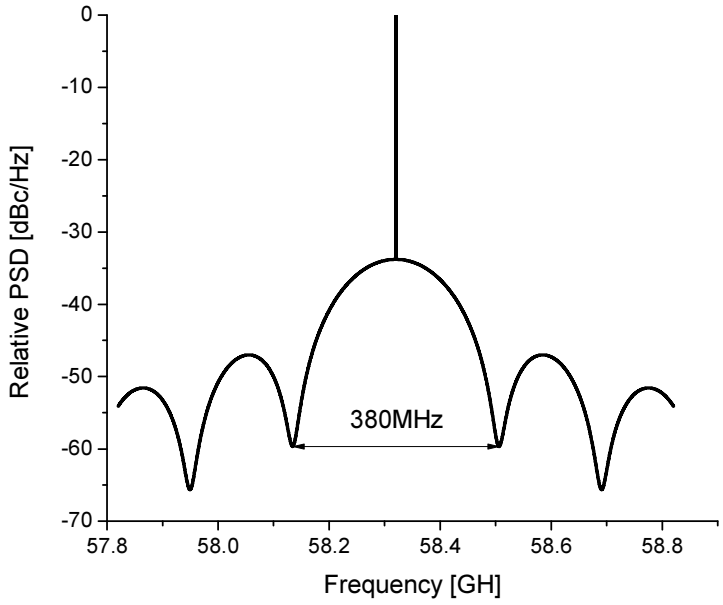

Fig. 2.3. Simulated PSD of the optical mmW ($|\tau_d|/\tau_{cOP} = 0.051$)

In our self-heterodyning system, the optical path difference ΔL is 1.08 m ($|\tau_d| = 0.0054\mu s$) which corresponds typically to the insertion of a pigtailed MZM. The full linewidth of the laser source is 1.5 MHz, while the coherence time of the laser source (τ_{cOP}) is 0.106 μs by the definition of coherence time in (2.30). The up-conversion frequency $2f_{LO}+f_{IF}$ is 58.32 GHz corresponding to the first carrier frequency in ECMA 387 standard. The PSD of the optical mmW, which is normalized relatively to its maximum value, is plotted in Fig. 2.3 by using formula (2.40). The

simulated PSD of the optical mmW and the constellation diagram will be demonstrated by the experiment.

(2) $|\tau_d|$ is small

When $|\tau_d|$ is small compared to τ_{cOP} ($|\tau_d| << \tau_{cOP}$), the PSD of the optical mmW can be developed as

$$S_{\mathrm{m}mW}(\omega) = 4R^2 E_1^2 E_2^2 \frac{4\gamma_{LO} + \gamma_{IF}}{(4\gamma_{LO} + \gamma_{IF})^2 + (2\pi(f - 2f_{LO} - f_{IF}))^2} \tag{2.41}$$

Equations (2.39) and (2.41) indicate that the PSD of the optical mmW follows Lorentzian slope as the RF signals do, under the assumption of perfect optical paths matching. We need to mention that the result (2.41) is valid only under the assumption that the frequency noise of the optical wave and RF signal only contains white component. The PSDs of the optical mmW at best optical path matching conditions ($|\tau_d| \approx 0$), of LO signal, and of IF signal from (2.39) and (2.41) which are normalized relatively to the carriers, are shown in Fig. 2.4.

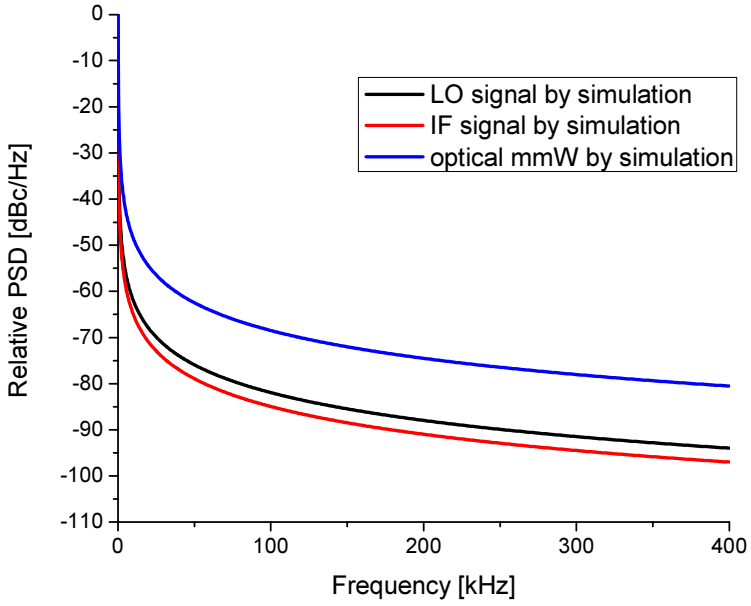

Fig. 2.4. Simulated normalized PSDs of the optical mmW under best matching ($|\tau_d| \approx 0$), of LO signal and of IF signal.

Now, we probe the phase noise impact to the digital modulation. We consider a digital modulation applied to the IF signal in the system as shown in Fig. 2.5.

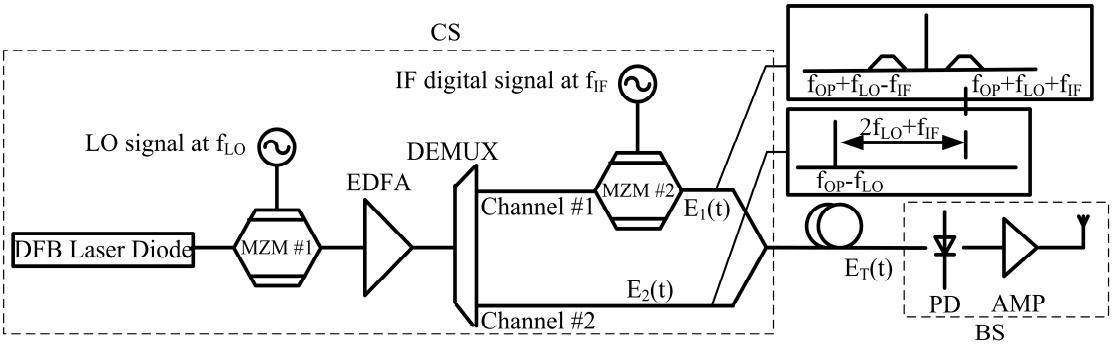

Fig. 2.5. Principle of the optical self-heterodyning digitally mmW generation

The complex envelope of the digital mmW is expressed as

$$\tilde{x}_{mmW}(t) = \tilde{x}(t)\exp\left(j\phi_{mmW}(t)\right) \tag{2.42}$$

where $\tilde{x}(t)$ is the complex envelop of the ideal broadband digital signal, $\phi_{mmW}(t)$ is the phase jitter of the optical mmW defined in (2.7). According to (2.7), the phase jitter of the optical mmW contains two contributions, which are the phase noise $\triangle\phi_{OP}(\tau_d)$ induced by delayed optical self-heterodyning and the phase jitter $\phi_{RF}(t)$ from the two electrical generators. Since the optical phase jitter and electrical phase jitters are totally independent, the variance of the optical mmW phase jitter can be expressed as

$$\begin{aligned}
\sigma^2_{\phi_{mmW}} &= E\left(\left[\phi(t) - E\left(\phi(t)\right)\right]^2\right) \\
&= E\left(\left[\Delta\phi_{OP}(t,\tau_d) + \phi_{RF}(t) - E\left(\Delta\phi_{OP}(t,\tau_d) + \phi_{RF}(t)\right)\right]^2\right) \\
&= E\left(\left\{\left[\Delta\phi_{OP}(t,\tau_d) - E\left(\Delta\phi_{OP}(t,\tau_d)\right)\right] + \left[\phi_{RF}(t) - E\left(\phi_{RF}(t)\right)\right]\right\}^2\right) \\
&= E\left(\left[\Delta\phi_{OP}(t,\tau_d) - E\left(\Delta\phi_{OP}(t,\tau_d)\right)\right]^2\right) + E\left(\left[\phi_{RF}(t) - E\left(\phi_{RF}(t)\right)\right]^2\right) + \\
&2E\left(\left[\Delta\phi_{OP}(t,\tau_d) - E\left(\Delta\phi_{OP}(t,\tau_d)\right)\right]\left[\phi_{RF}(t) - E\left(\phi_{RF}(t)\right)\right]\right) \\
&= \sigma^2_{\Delta\phi_{OP}}(\tau_d) + \sigma^2_{\phi_{RF}} + 2E\left(\left[\Delta\phi_{OP}(t,\tau_d) - E\left(\Delta\phi_{OP}(t,\tau_d)\right)\right]\right)E\left(\left[\phi_{RF}(t) - E\left(\phi_{RF}(t)\right)\right]\right) \\
&= \sigma^2_{\Delta\phi_{OP}}(\tau_d) + \sigma^2_{\phi_{RF}}
\end{aligned} \tag{2.43}$$

where $\sigma_{\phi mmW}{}^2$ is the variance of the optical mmW phase jitter, $\sigma_{\phi\,RF}{}^2$ is the variance of the RF signal phase jitter.

The variance of the RF phase jitter $\sigma_{\phi\,\mathrm{RF}}{}^2$ is derived by the definition of ϕ_{RF} in (2.7).

$$
\begin{aligned}
\sigma_{\phi_{RF}}^2 &= E\left(\left[\phi_{RF}(t) - E\left(\phi_{RF}(t)\right)\right]^2\right) \\
&= E\left(\left[2\phi_{LO}(t) + \phi_{IF}(t) - E\left(2\phi_{LO}(t) + \phi_{IF}(t)\right)\right]^2\right) \\
&= E\left(\left[2\phi_{LO}(t) - 2E\left(\phi_{LO}(t)\right) + \phi_{IF}(t) - E\left(\phi_{IF}(t)\right)\right]^2\right) \\
&= E\left(\left[2\phi_{LO}(t) - 2E\left(\phi_{LO}(t)\right)\right]^2\right) + E\left(\left[\phi_{IF}(t) - E\left(\phi_{IF}(t)\right)\right]^2\right) + \\
&\quad 4E\left(\phi_{LO}(t) - E\left(\phi_{LO}(t)\right)\right)E\left(\phi_{IF}(t) - E\left(\phi_{IF}(t)\right)\right) \\
&= 4\sigma_{\phi_{LO}}^2 + \sigma_{\phi_{IF}}^2
\end{aligned}
\tag{2.44}
$$

where $\sigma_{\phi LO}^2$ and $\sigma_{\phi IF}^2$ are the variances of the LO and IF signal phase jitter respectively. $\sigma_{\triangle \phi OP}^2(\tau_d)$ is obtained by (2.28)

$$
\sigma_{\Delta\phi_{OP}}^2(\tau_d) = 2\gamma_{OP}|\tau_d| = \frac{|\tau_d|}{\tau_{cOP}} \tag{2.45}
$$

The variance of the optical mmW phase jitter $\sigma_{\phi mmW}^2$ is thus derived by substituting (2.44) and (2.45) into (2.43)

$$
\sigma_{\phi_{mmW}}^2 = 2\gamma_{OP}|\tau_d| + \left(4\sigma_{\phi_{LO}}^2 + \sigma_{\phi_{IF}}^2\right) = \frac{|\tau_d|}{\tau_{cOP}} + \left(4\sigma_{\phi_{LO}}^2 + \sigma_{\phi_{IF}}^2\right) \tag{2.46}
$$

(1) $|\tau_d|$ is large

When the optical delay $|\tau_d|$ is large compared to the laser coherence time τ_{cOP}, $\sigma_{\phi LO}^2$ and $\sigma_{\phi IF}^2$ in (2.44) can be ignored. In this case, the optical mmW phase jitter follows stationary Gaussian process, and the variance of which depends on $|\tau_d|/\tau_{cOP}$ (see equation (2.46)).

$$
\sigma_{\phi_{mmW}}^2 = \frac{|\tau_d|}{\tau_{cOP}} \tag{2.47}
$$

(2) $|\tau_d|$ is small

When $|\tau_d|$ is small compared to τ_{cOP} ($|\tau_d| << \tau_{cOP}$), the variance of the optical mmW only depends on the phase noise contributions from LO generator and from IF generator.

$$
\begin{aligned}
\sigma_{\phi_{mmW}}^2 &= 2\gamma_{OP}|\tau_d| + \left(4\sigma_{\phi_{LO}}^2 + \sigma_{\phi_{IF}}^2\right) \\
&\approx 4\sigma_{\phi_{LO}}^2 + \sigma_{\phi_{IF}}^2
\end{aligned}
\tag{2.48}
$$

2.2.2 Phase noise impact on digitally modulated optical mmW

Based on the investigation of optical phase to intensity noise conversion, we managed to build a model for the mmW phase noise. To meet the demands of the mmW wireless transmission standards, such as ECMA 387 standard [15], it is necessary to further inquire into the degradation of the digital signal quality induced by the phase noise. EVM is usually applied to qualify the digital signal in different standard. In the thesis, we try to meet the demands of ECMA 387 standard [15].

In ECMA 387 standard, EVM is defined as [15]

$$EVM = \frac{\sqrt{\frac{1}{N}\sum_{n=1}^{N}\left|S_r(n) - S_t(n)\right|^2}}{R_{\max}} \tag{2.49}$$

where N is the number of the transmitted symbols, S_r is normalized received symbol, S_t is the ideal transmitted symbol, R_{max} is maximum magnitude of the ideal transmitted symbol for the chosen modulation. The EVM as a function of SNR and $\sigma_{\phi mmW}{}^2$ can be presented as [16]

$$EVM = \sqrt{\frac{1}{SNR} + 2 - 2\exp\left(-\frac{\sigma_{\phi_{mmW}}^2}{2}\right)}\sqrt{\frac{1}{PAPR}} \tag{2.50}$$

where PAPR is the peak to average power ratio for the considered modulation scheme and SNR is the output signal to noise ratio. The noise comes from the amplified spontaneous emission (ASE) of the EDFA and laser source and the thermal noise of receiver.

Since the optical heterodyning system using WDM DEMUX is proposed to be compatible with different modulation scheme, it makes sense to investigate the phase noise impact to different modulation scheme. Generally speaking, equation (2.49) validates for any modulation scheme. The EVM value depends on the SNR, which is defined by the amplitude noise of the optical mmW, and the variance of the phase noise defined as (2.46). By using (2.46), the EVM expressed in (2.49) is derived as

$$EVM = \sqrt{\frac{1}{SNR} + 2 - 2\exp\left(-\frac{|\tau_d|}{2\tau_{cOP}} - 2\sigma_{\phi_{LO}}^2 - \frac{1}{2}\sigma_{\phi_{IF}}^2\right)}\sqrt{\frac{1}{PAPR}} \tag{2.51}$$

Usually, the electrical generator applied to the MZM in our system for the optical frequency conversion is with low phase noise. That means that the phase noise contributions from the LO signal and IF signal are negligible compared to the optical phase to intensity noise conversion contribution. In this case, the EVM of a system, with a given SNR, only depends on the value of $|\tau_d|/\tau_{cOP}$.

$$EVM = \sqrt{\frac{1}{SNR} + 2 - 2\exp\left(-\frac{|\tau_d|}{2\tau_{cOP}}\right)}\sqrt{\frac{1}{PAPR}} \tag{2.52}$$

It is possible to figure out the curve which indicates EVM as a function of $|\tau_d|/\tau_{cOP}$ by using (2.52). Fig. 2.6 indicates that the typical relationship between EVM and SNR ($EVM = \sqrt{1/SNR}$) validates under the best optical path matching ($|\tau_d| = 0$). With a given SNR, it is easy to find the maximum $|\tau_d|/\tau_{cOP}$, which feed up the requirement of EVM value according to the standard (EVM_{max} in Fig. 2.6), such as ECMA 387 standard [15]. It is also shown from Fig. 2.6 that the contribution of optical phase to intensity conversion could be the dominant contribution, since the EVM grows fast even if $|\tau_d|/\tau_{cOP}$ is small. It is necessary to find the maximum value of $|\tau_d|/\tau_{cOP}$ for different modulation scheme corresponding to the ECMA 387 standard [15], when we assume that SNR is large ($1/SNR \approx 0$) so that we can quantify only the impact of the phase noise on the digitally modulated mmW.

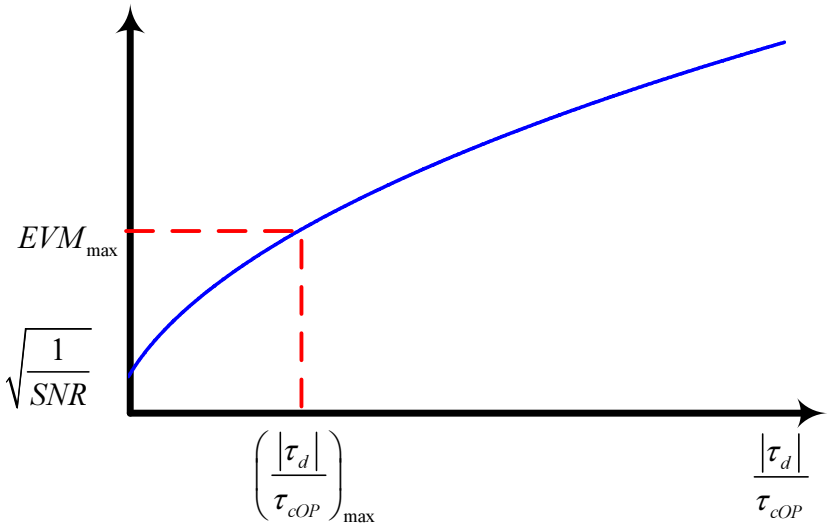

Fig. 2.6. Theoretical analysis of EVM as a function of $|\tau_d|/\tau_{cOP}$

Tab. 2.1 gives maximum $|\tau_d|/\tau_{cOP}$ for different modulation schemes, which are

calculated by using (2.52) with the assumption $1/SNR \approx 0$ and maximum optical path difference corresponding to the use of typical DFB laser with full linewidth of 1.5 MHz. We compare 1588 Mbps BPSK, 3175 Mbps QPSK, 4763 Mbps NS8QAM and 6352 Mbps QAM 16 modulation schemes, which have the same bandwidth, in order to have the same noise conversion contribution. PAPRs for both BPSK and QPSK signals are 1, and PAPRs for both NS8QAM and QAM 16 are 1.8. Tab. 2.1 indicates that the requirement of optical paths matching for higher order modulation scheme is stricter, following the EVM requirements. Despite on this, maximum optical path difference for 6352 Mbps QAM 16 modulation application is in the range of several centimeters in high SNR optical heterodyning system, which would be still feasible using commercial pigtailed components.

Tab. 2.1. Max values of $|\tau_d|/\tau_{cOP}$ for signals with different modulation scheme compliant with ECMA 387 standard with laser full linewidth of 1.5 MHz

Modulation Scheme	1588Mbps BPSK	3175 Mbps QPSK	4763 Mbps NS8QAM	6352 Mbps QAM 16
PAPR	1	1	1.8	1.8
EVM requirement (%)	11.2	10.9	6.3	5.6
Maximum τ_d/τ_c	0.0126	0.0119	0.0072	0.0057
Maximum optical path difference (m)	0.4005	0.3793	0.2278	0.1799

As a conclusion, the phase noise impact to the EVM value has been theoretically investigated in this part. It has given a rule to design the WDM-RoF system. The model will be experimentally demonstrated in the following sections.

2.3 Phase noise measurement

2.3.1 K-band signal measurement

The optical mmW is generated by the experimental setup shown in Fig. 2.1. As it is said above, it is necessary to find the best optical paths matching. Since electrical spectrum analyzer (ESA) working in 60 GHz band needs an external harmonic mixer [17], we can only observe the spectrum of the optical generated signal in low bandwidth (<340 MHz), which is not enough to prove the slope of the PSD by theoretical analysis

as shown in Fig. 2.4. As a consequence, we firstly measure the spectrum of the optical generated signal in K-band for different optical lengths differences, and further measure the phase noise of the optical mmW in V-band by Agilent ESA using external harmonic mixer. During the measurement in K-band, f_{LO} is set at 25 GHz and f_{IF} is set at 15 GHz. Therefore, the RF signal at $2f_{LO}$ - f_{IF} =35 GHz, which has the same phase noise as the target RF signal at $2f_{LO}$ + f_{IF}, is measured in our experiment. Several optical fibers with different lengths are applied in channel #1 and #2 in order to find the good optical paths matching. The optically generated RF signal spectrums with the large span of 1 GHz for different optical length differences, which take the best path matching as reference, are shown in Fig. 2.7. Comparing Fig. 2.4 and Fig. 2.7, the slope of the measured spectrum (Fig. 2.7) agrees with theoretical analysis (Fig. 2.4) in large span, while the optical path difference brings significant phase to intensity noise.

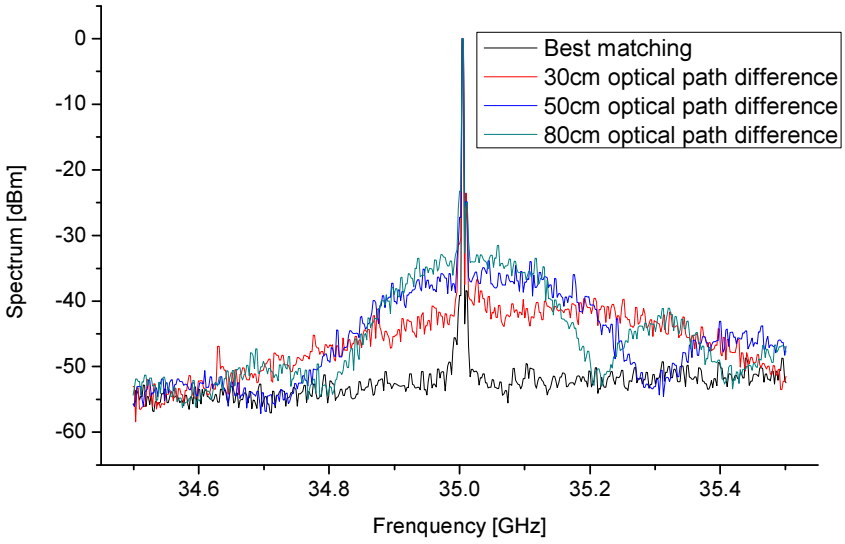

Fig. 2.7. Spectrum of 35GHz optical mmW with different optical delays

Furthermore, in order to prove that there is no impact of the phase noise due to the optical paths mismatching in our self-heterodyning system, we have measured the single side-band (SSB) phase noise of the optically generated RF signal under the best path matching, compared with the phase noise of the two electrical generators, in Fig. 2.8. We mention that the phase noise floor shown in Fig. 2.8 is induced by the photodetection of ASE-Signal beat noise from EDFA, which is dominant for a frequency offset larger than 1 MHz.

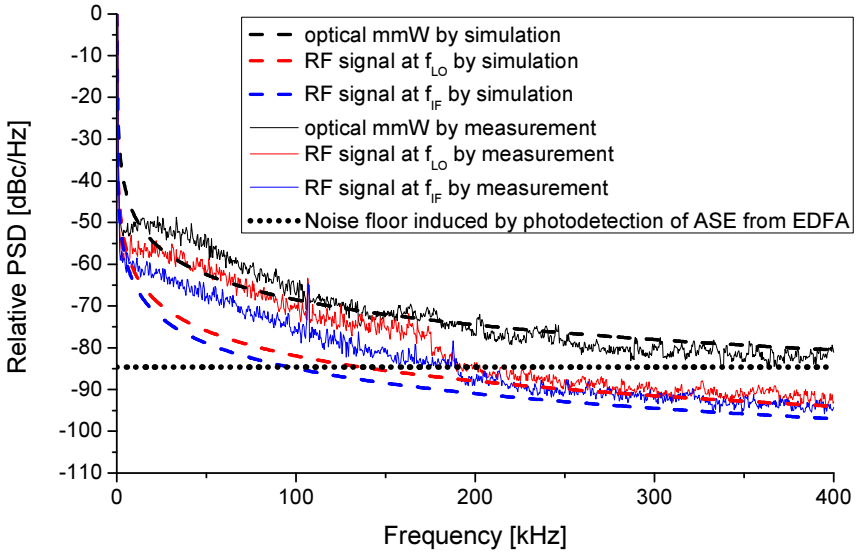

Fig. 2.8. Measured and simulated single side-band (SSB) normalized PSDs of LO signal (f_{LO} = 25GHz), IF signal (f_{IF} = 15GHz) and mmW signal ($2f_{LO}$ - f_{IF} =35 GHz) generated with optical self-heterodyning system.

Under the best path matching ($|\tau_d| \approx 0$), the phase noise PSD of the optical mmW, the RF signals at f_{LO} and f_{IF} from the two electrical generators, which are normalized relatively to the carriers respectively, could be expressed as the following equation by using (2.39) and (2.48)

$$S_{mmWnormalized}(f) = 10\log_{10}\frac{(4\gamma_{LO}+\gamma_{IF})^2}{(4\gamma_{LO}+\gamma_{IF})^2+(2\pi(f-2f_{LO}-f_{IF}))^2}$$
$$S_{LOnormalized}(f) = 10\log_{10}\frac{\gamma_{LO}^2}{\gamma_{LO}^2+(2\pi(f-f_{LO}))^2} \quad (2.53)$$
$$S_{IFnormalized}(f) = 10\log_{10}\frac{\gamma_{IF}^2}{\gamma_{IF}^2+(2\pi(f-f_{IF}))^2}$$

Comparing the measured PSD of RF signal at f_{LO} and f_{IF} in Fig. 2.8, γ_{IF} is half of γ_{LO} (γ_{LO} =0.5γ_{IF}). As a consequence, from the results of the theoretical approach when $|\tau_d| \approx 0$ in (2.53), the normalized phase noise PSD of the optical mmW is expected $S_{mmWnormalized}$- $S_{LOnormalized}$ = 12.2 dB higher than the phase noise PSD of LO generator. Indeed, from Fig. 2.8, around 400 kHz, we measured that the phase noise PSD of the optical mmW is 12 dB higher than the phase noise PSD of LO generator, which is close enough to the theoretical value of 12.2 dB found with (2.53).

Hence the theoretical PSD of the optical mmW and RF signal at f_{LO} and f_{IF} by using (2.53) are shown in Fig. 2.8 compared to the measurement results. It is obvious that the

measured spectrums agree with the theoretical analysis far from the carrier which is the validity domain of the proposed approach considering white frequency noise. From Fig. 2.8, the measured phase noise PSD for both optical mmW and RF signals close to the carrier are much higher than the theoretical results because of the additional *1/f* noise contributions, which are not taken into account during the theoretical analysis.

Experimental results show that optical path matching can be reached so that optical phase noise to intensity noise conversion does not impact the optically generated mmW phase noise.

The important result is that when optical path matching is realized, optical mixing process is transparent and mmW phase noise is only impacted by RF source phase noises.

2.3.2 V-band signal measurement

In the part above, the best matching of the optical path is found by implementing the phase noise measurement in 40 GHz band. We further give the phase noise investigation of the optical mmW in 60 GHz band. The LO signal in Fig. 2.1 is set to 26.91 GHz and the IF signal is set to 6.66 GHz. As a result, the RF signal at $2f_{LO} + f_{IF}$ = 60.48 GHz is measured by ESA. Here we use Agilent N9030 PXA signal analyzer with the external waveguide harmonic mixer M1970V option 002 [17] to analyze the mmW in V-band.

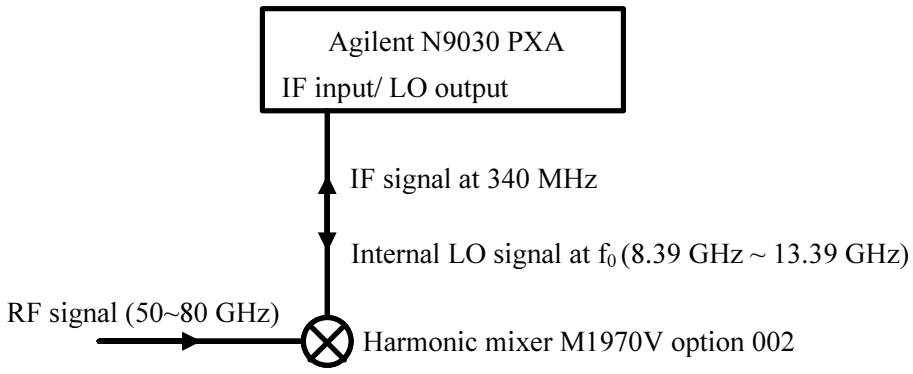

Fig. 2.9. Principle of the V-band phase noise measurement by using harmonic mixer

Fig. 2.9 shows the principle of the harmonic mixer M1970V [17]. An internal LO signal from the Agilent ESA is applied to the harmonic mixer. The V-band signal is mixed with 6 order harmonic LO signal to generate an IF signal at 340 MHz, which is

sent back to the Agilent ESA to analyze. Since the IF signal will be remixed into harmonic mixer, there will be many down-converted products with the frequency space of 340 MHz input into the Agilent ESA. Although there is a software in the ESA to suppress the other down-converted products, the ESA only supports narrow band (<340 MHz) accurate spectrum analysis to get rid of the impact of the other mixing products. Regarding the phase noise measurement, it is done in 1 or 2 MHz band, and the impact of the other mixing products will be avoided. Since the IF signal input into the Agilent ESA is generated by the mixing of optical mmW and 6 order harmonic internal LO signal, the variance of the IF signal phase noise is expressed as

$$\sigma^2_{\phi_{IFmixer}} = \sigma^2_{\phi_{mmW}} + 36\sigma^2_{\phi_{LOmixer}} = 4\sigma^2_{\phi_{LO}} + \sigma^2_{\phi_{IF}} + 36\sigma^2_{\phi_{LOmixer}} \tag{2.54}$$

Equation (2.54) indicates that the phase noise of the optical mmW will be over evaluated by Agilent ESA, since there's an additional component from the internal LO signal. However, the internal LO signal is in 8.39 GHz to 13.39 GHz band, which is much lower that the frequency of LO signal (f_{LO}) in Fig. 2.1. The variance of the internal LO signal (8.39 GHz to 13.39 GHz) from the Agilent ESA is commonly negligible compared to the variance of the LO signal (26.91 GHz) from electrical generator. As a consequence, the impact of the harmonic mixer can be ignored. The phase noise is measured in V-band by Agilent ESA using the harmonic mixer M1970V and is shown in Fig. 2.10.

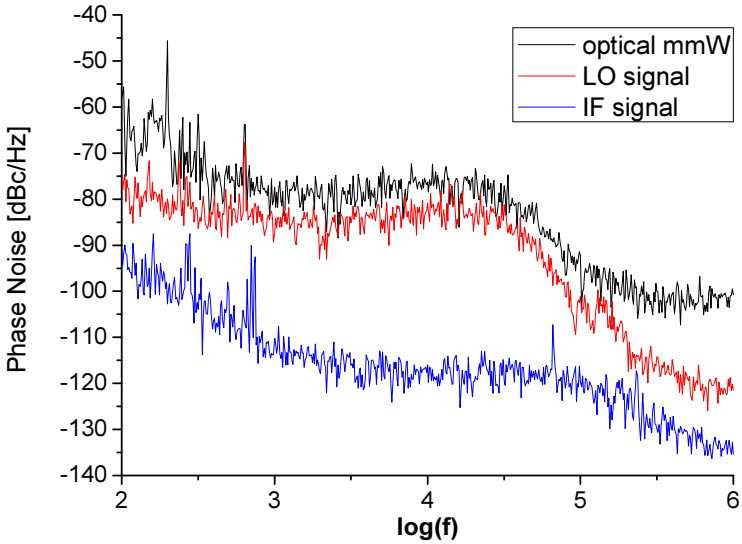

Fig. 2.10. Phase noise measurement in V-band

Fig. 2.10 indicates that the PSD of the optical mmW and PSD of the LO signal follow the same slope and there is commonly 10dB between the two figures. This agrees with the theoretical analysis of (2.53). The PSD of the IF signal (6.66 GHz) is roughly 30 dB lower than the PSD of the LO signal. The internal LO signal from the Agilent ESA for the harmonic mixer is in the same range of IF signal so that the phase noise variance internal LO signal for the harmonic mixer ($\sigma_{\phi LOmixer}^2$) is approximate to the phase noise variance of the IF signal. This experimental result proves that the impact of the harmonic mixer is negligible.

As it is discuss above, the phase noise is quantified by the variance of the phase jitter. In general case, the PSD of a CW signal from the electrical generator is usually expressed as [18]:

$$S(f) = \frac{V^2}{2}\delta(f - f_c) + \frac{V^2}{2}S_\phi(f - f_c) \tag{2.55}$$

where S is the PSD of the signal, V is the amplitude of the signal, fc is the center frequency of the signal, S_ϕ is the PSD of the phase jitter.

And signal power is derived from (2.55) [18]:

$$P = \int_0^\infty S(f)\,df = \frac{V^2}{2} + \frac{V^2}{2}\sigma_\phi^2 \tag{2.56}$$

where P is the power of the signal. Equation (2.56) indicates that the variance of the CW signal phase jitter can be obtained by integrating the normalized phase noise PSD of the signal. As a result, the variances of the optical mmW phase jitter, of LO signal phase jitter and of IF signal phase jitter can be expressed as (2.57) by using (2.56)

$$\begin{aligned}
\sigma_{\phi_{mmW}}^2 &= \int_0^\infty S_{mmWnormalized}(f)\,df \\
\sigma_{\phi_{LO}}^2 &= \int_0^\infty S_{LOnormalized}(f)\,df \\
\sigma_{\phi_{IF}}^2 &= \int_0^\infty S_{IFnormalized}(f)\,df
\end{aligned} \tag{2.57}$$

The phase jitter variances of the optical mmW ($\sigma_{\phi mmW}^2$), of the LO signal ($\sigma_{\phi LO}^2$) and of the IF signal ($\sigma_{\phi IF}^2$) can be obtained by integrating the normalized phase noise PSD of the LO and IF generators in Fig. 2.10. Since the ESA cannot measure from 0 Hz to ∞, we integrate the normalized phase noise PSD in the bandwidth from 100 Hz to 1 MHz

(Fig. 2.10).

$$\begin{aligned}\sigma^2_{\phi_{mmW}} &\approx \int_{1E2}^{1E6} S_{mmWnormalized}(f)\,df = 1.0518\times10^{-6}\\ \sigma^2_{\phi_{LO}} &= \int_{1E2}^{1E6} S_{LOnormalized}(f)\,df = 2.2737\times10^{-7}\\ \sigma^2_{\phi_{IF}} &= \int_{1E2}^{1E6} S_{IFnormalized}(f)\,df = 4.5230\times10^{-10}\end{aligned} \tag{2.58}$$

From experimental results extracted from (2.58), it is obvious that $\sigma_{\phi mmW}{}^2 \approx 4\sigma_{\phi LO}{}^2+\sigma_{\phi IF}{}^2$, which agrees with the theoretical model (2.46).

2.4 Broadband mmW generation by optical heterodyning technique using WDM DEMUX

In section 2.3, the phase noise for CW signal is experimentally demonstrated. In this section, the digital modulation is implemented and the broadband mmW generation by optical heterodyning technique using WDM DEMUX is performed.

2.4.1 Experimental setup

In this paragraph, it should be mentioned that the optical path difference can be adjusted to show the impact of phase modulation to intensity modulation conversion, investigated in the previous section, on the transmission performance.

Fig. 2.11 shows the configuration of the proposed RoF system for broadband mmW generation using WDM DEMUX. In CS, the experiment is performed on a single longitudinal mode DFB laser emitting at 1550 nm. A Mach-Zehnder Modulator (MZM #1) is employed to realize the up-conversion. A DC voltage of 2.1 V is applied to the MZM #1 in order to get the minimum optical carrier output. A power of 12 dBm CW signal at f_{LO}=25.66 GHz is applied to the MZM. Here we mention that the CW signal is only applied to one electrode of MZM #2. This means that the MZM #2 is behaving as single-arm MZM, which will be theoretically analyzed in the following section. The modulated optical wave is then amplified by the EDFA to get a constant output power of 20 dBm. The amplified optical wave is sent into the WDM Demultiplexer (DEMUX) with a channel spacing of 25 GHz. Therefore, the upper-sideband and

lower-sideband of the optical field, separated by 51.32GHz, are divided in channel #2 and channel #4.

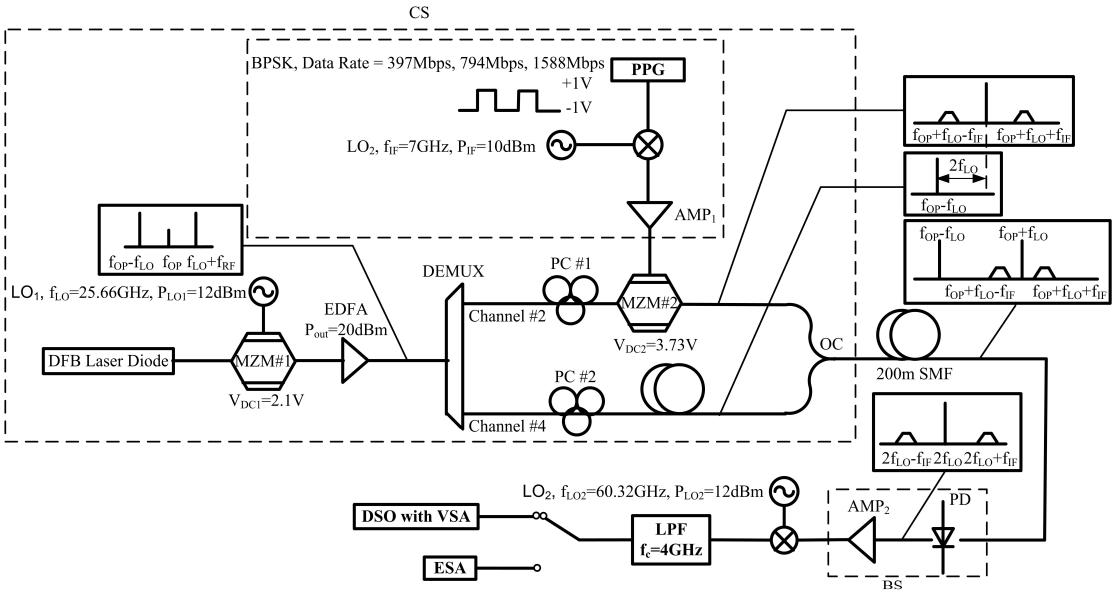

Fig. 2.11. Experimental setup of RoF system for broadband mmW generation using WDM DEMUX
CS: Center Station, BS: Base Station, MZM: Mach-Zehnder Modulator, LO: Local oscillator, EDFA: Erbium-Doped Fiber Amplifier, DEMUX: WDM Demultiplex, PC: Polarization Controller, PPG: Pulse Pattern Generator, AMP: electrical Amplifier, OC: Optical Coupler, SMF: Single Mode Fiber, PD: Photo Diode, LPF: Low Pass Filter, DSO: Digital Storage Oscilloscope, VSA: Vector Signal Analyzer software, ESA: Electrical Spectrum Analyzer

In channel #2, the optical field is modulated by using a second MZM (MZM #2 in Fig. 2.11) biased in linear regime. A Polarization Controller (PC #1) is employed to adjust the input optical polarization for the MZM #2. The signal which drives MZM #2 is a BPSK signal with the data rate of 397 Mbps, 794 Mbps or 1588 Mbps at intermediate frequency f_{IF} =7 GHz. The selected data rates correspond to the values defined in the ECMA 387 standard. More complex modulation schemes, which are compliant with the ECMA 387 standard, such as Quadrature Phase Shift Keying (QPSK), Non-Square 8 Quadrature Amplitude Modulation (NS8QAM), 16 Quadrature Amplitude Modulation (16QAM), or Orthogonal Frequency Division Multiplexing (OFDM), could be implemented with this configuration, but can not be demonstrated due to the limitation of our generation capabilities. The broadband BPSK signal is then electrically amplified to reach the power of 10 dBm. In channel #4, another PC #2 is applied to adapt the polarization of the optical field to the optical polarization of

channel #2. The two optical signals from channel #2 and #4 are combined by using an optical combiner and transmitted through a 200 meter length single mode fiber (SMF) to the BS. As a result of the photodetection in the BS, the output signal of the PD contains not only the desired BPSK modulated signal at $2f_{LO} + f_{IF}$ = 58.32 GHz, but also a BPSK modulated signal at $2f_{LO} - f_{IF}$ = 44.32 GHz and a CW signal at $2f_{LO}$ = 51.32 GHz, which are undesired. The BPSK signal at 44.32 GHz could be removed by using a waveguide filter. The CW signal at 51.32 GHz could be efficiently reused in the up-link system (not investigated in this chapter), for frequency down-conversion of the received mmW signal at the BS by using an electronic mixer. Finally, the optically generated signal at the PD is amplified with a 28 dB gain amplifier (AMP_2).

As it is shown in Fig. 2.11, the BPSK signal at 58.32 GHz is electronically down-converted to 2 GHz band using an electrical mixer driven by 60.32 GHz mmW local oscillator (LO_3). The electrically down-converted signal is either digitalized with the Digital Storage Oscilloscope (DSO) and demodulated by the Vector Signal Analyzer (VSA) software (Agilent) or analyzed by using a spectrum analyzer. A low-pass filter (cut-off frequency f_c=4 GHz) is employed before the DSO to filter out all the undesired spectral components. We mention that we do not down-convert the mmW signal into baseband in order to benefit from the synchronization facility provided by the VSA software for coherent RF demodulation. The Error Vector Magnitude measurement (EVM) is performed by the VSA to quantify the quality of the received digital signal.

2.4.2 Experimental results

2.4.2.1 Demonstration of mmW generation by optical self-heterodyning technique

The spectrum and the constellation diagram for different data rates BPSK signal after photonic mmW generation and electrical frequency down-conversion are shown in Fig. 2.12

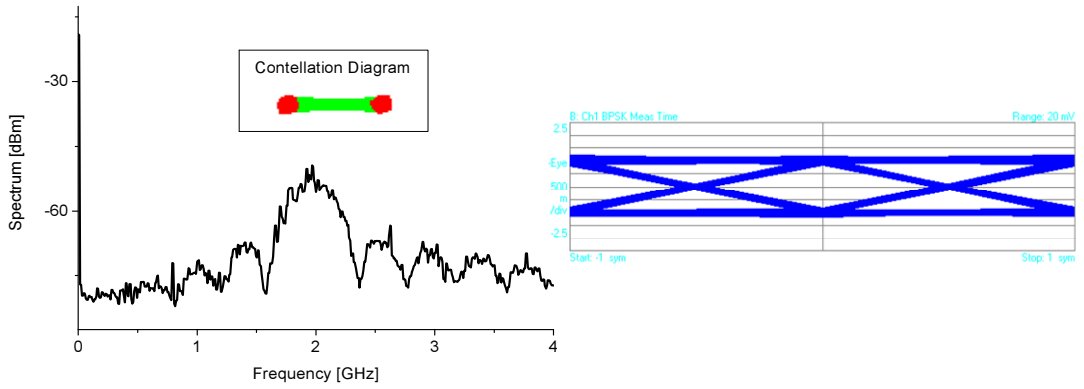

Spectrum after electrical down-conversion (inset constellation diagram) Eyediagram after demodulation

(a) 397Mbps mmW

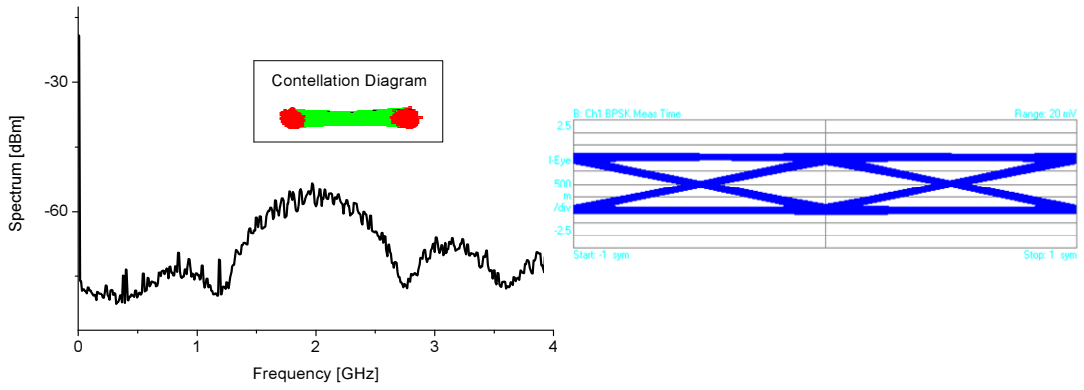

Spectrum after electrical down-conversion (inset constellation diagram) Eyediagram after demodulation

(b) 794Mbps mmW

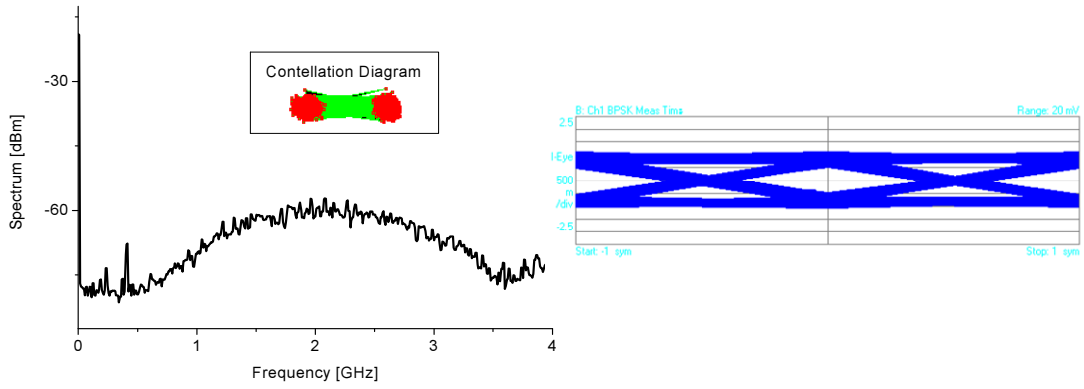

Spectrum after electrical down-conversion (inset: constellation diagram) Eyediagram after demodulation

(c) 1588Mbps mmW

Fig. 2.12. Measurement results of the optical generated mmW after electrical down-convertion and demodulation

EVM and the signal power are reported in Tab. 2.2, compared with the EVM requirements according to ECMA 387 standard based on the assumptions of near ideal receiver and AWGN channel and the back-to-back (BTB) measurement of the IF signal source. We mention that all the results for photonic generated mmW are

measured after electrical down-conversion from 58.32GHz to 2GHz.

Tab. 2.2. Power and EVM measurements compared with the requirements according to ECMA 387 standard

(i) ECMA387 requirements for transmitter and receiver			
Data Rate (Mbps)	397	794	1588
Maximum emitted power (dBm)	10	10	10
Maximum allowed EVM (%)	33.4	23.7	11.2
(ii) Output optical mmW by photodetection			
Data Rate (Mbps)	397	794	1588
Power after down-conversion (dBm)	-27.49	-27.77	-28.44
Received Power at 58.32 GHz (dBm)	-20.49	-20.77	-21.44
EVM (%)	7.18	9.57	12.56
(iii) Back-to-back measurement of the IF signal source			
Data Rate (Mbps)	397	794	1588
EVM(%)	5.8	6.0	7.2

Comparing measurement results shown in Tab. 2.2 (ii) with the EVM requirements according to ECMA 387 standard shown in Tab. 2.2 (i), EVM value of the optical mmW are in the limit of the ECMA 387 standard to insure error free transmission except for the EVM of 1588 Mbps data signal. EVM measurements for the optical generated broadband mmW at 397 Mbps and 794 Mbps meet the requirements of the ECMA 387 standard with a big margin (Tab. 2.2).

Tab. 2.2 (iii) shows the BTB measurements of IF signal source. Comparing Tab. 2.2 (ii) and (iii), it can be seen that the EVM degradation due to the RoF system is not significant. During the BTB EVM measurements of the IF signals, it can be seen that there is significant intersymbol interference (ISI). We can expect that another high-quality IF digital signal generator will improve the mmW generated by the RoF system and lead the 1588 Mbps BPSK mmW compliant with the ECMA 387 standard requirement.

2.4.2.2 Single-arm MZM without bias voltage

Since the MZM #2 works as single-arm MZM, we show below that it is unnecessary to bias MZM #2. In order to analyze the output optical field of the MZM, it is necessary to figure out the structure of the MZM.

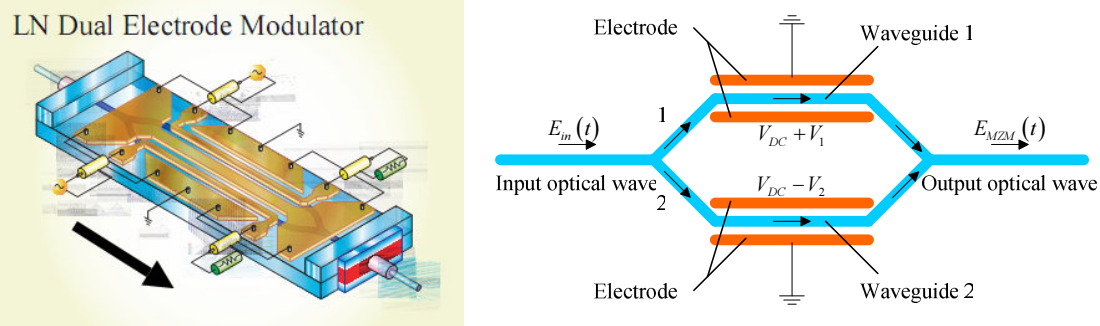

Fig. 2.13. Structure of the MZM produced by Sumitomo Osaka Cement Co., Ltd

Fig. 2.13 shows the MZM from Sumitomo Corporation, which is applied in our optical self-heterodyning system. The input optical field is separated into two optical waveguides by the optical Y junction. Each waveguide is biased by a pair of electrodes. Each pair of electrodes is driven by a RF signal and the two pairs of electrodes share the same DC voltage. As a consequence, the electrical fields of the two pairs of electrodes are expressed as

$$\begin{aligned} V_1(t) &= V_{DC} + V_{RF1}(t) \\ V_2(t) &= -\left(V_{DC} - V_{RF2}(t)\right) \end{aligned} \tag{2.59}$$

where $V_1(t)$ and $V_2(t)$ are the electrical fields of the two pairs of electrodes respectively. $V_{RF1}(t)$ and $V_{RF2}(t)$ are the two RF signals applied to the two pairs of electrodes respectively. V_{DC} is the DC voltage. The refractive index of the optical waveguide is controlled by the electrical field of the pair of electrodes. As a result, the phase shift of the two optical waveguide is

$$\begin{aligned} \phi_1(t) &= \frac{V_1(t)}{2V_\pi}\pi \\ \phi_2(t) &= \frac{V_2(t)}{2V_\pi}\pi \end{aligned} \tag{2.60}$$

where V_π is half wave voltage of the MZM.

- Case 1 : MZM works as push-pull function

We assume here that there are two RF signals applied to the MZM. When the two RF signals follows V_{RF1}=-V_{RF2}=V_{RF}, the MZM works as push-pull function. The output optical field is expressed as

$$
\begin{aligned}
E_{MZM}(t) &= \frac{1}{2}\frac{1}{\sqrt{I_L}} E_{in}(t)\left[\exp\left(j\pi\frac{V_1(t)}{2V_\pi}\right)+\exp\left(j\pi\frac{V_2(t)}{2V_\pi}\right)\right] \\
&= \frac{1}{2\sqrt{I_L}} E_{in}(t)\left[\exp\left(j\pi\frac{V_{DC}+V_{RF}(t)}{2V_\pi}\right)+\exp\left(-j\pi\frac{V_{DC}+V_{RF}(t)}{2V_\pi}\right)\right] \\
&= \frac{1}{\sqrt{I_L}} E_{in}(t)\cos\left(\pi\frac{V_{DC}+V_{RF}(t)}{2V_\pi}\right)
\end{aligned}
\tag{2.61}
$$

where $E_{MZM}(t)$ is the output optical field of the MZM, and $E_{in}(t)$ is the input optical field of the MZM. I_L is the insertion loss of the MZM, which is typically lower than 6 dB. The ratio of the output and input optical power as a function of $V_{DC} + V_{RF}(t)$ is expressed as

$$
\begin{aligned}
\frac{P_{out}}{P_{in}} &= \frac{\left|E_{MZM}(t)\right|^2}{\left|E_{in}(t)\right|^2} = \frac{1}{I_L}\cos^2\left(\pi\frac{V_{DC}}{2V_\pi}\right) \\
&= \frac{1}{I_L}\frac{1}{2}\left(\cos\left(\pi\frac{V_{DC}+V_{RF}}{V_\pi}\right)+1\right)
\end{aligned}
\tag{2.62}
$$

The ratio of the output and input optical power P_{out}/P_{in} as a function of $V_{DC} + V_{RF}(t)$ is plotted as Fig. 2.14 by using equation (2.62).

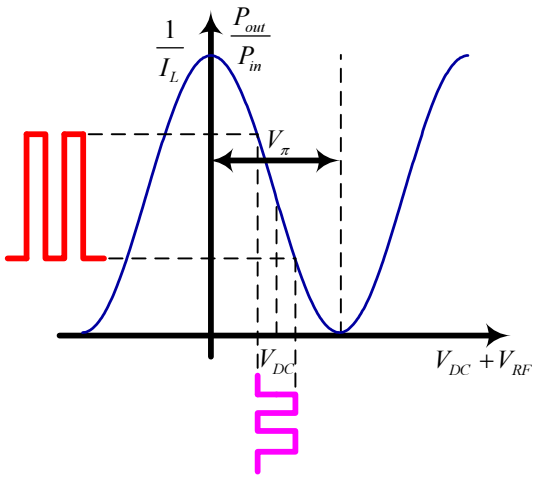

Fig. 2.14. P_{in}/P_{out} as a function of $V(t)$

Fig. 2.14 shows that it is better to bias the MZM at linear regime to get the maximum optical amplitude output without distortion, when a signal is applied to the MZM.

- Case 2 : MZM works as single-arm function

In our system, MZM #2 does not work as push-pull function but as a single arm.

The BPSK signal at IF frequency only applies to one RF port. The output optical field is expressed as

$$
\begin{aligned}
E_{MZM}(t) &= \frac{1}{2}\frac{1}{\sqrt{I_L}} E_{in}(t)\left[\exp\left(j\pi\frac{V_1(t)}{2V_\pi}\right)+\exp\left(j\pi\frac{V_2(t)}{2V_\pi}\right)\right] \\
&= \frac{1}{2\sqrt{I_L}} E_{in}(t)\left[\exp\left(j\pi\frac{V_{DC}+V_{RF}(t)}{2V_\pi}\right)+\exp\left(-j\pi\frac{V_{DC}}{2V_\pi}\right)\right] \\
&= \frac{1}{2\sqrt{I_L}} E_{in}(t)\exp\left(j\pi\frac{V_{DC}+V_{RF}(t)}{2V_\pi}\right)+\frac{1}{2\sqrt{I_L}} E_{in}(t)\exp\left(-j\pi\frac{V_{DC}}{2V_\pi}\right)
\end{aligned}
\tag{2.63}
$$

Equation (2.63) indicates that the optical wave in the waveguide 1 is phase modulated by the RF signal and the optical wave in the waveguide 2 is only phase shifted by the DC voltage. When the MZM works as single-arm function, the optical sideband is generated by optical phase modulation with waveguide 1. The optical field in waveguide 2 only contains the optical carrier. As a result, the amplitude of the sideband does not depend on the DC voltage applied to the MZM any longer. Hence, it is possible to simulate the optical spectrum of $E_{MZM}(t)$ with equation (2.63). In order to see clearly from the spectrum, we simply assume that the RF signal is a CW signal.

$$
V_{RF}(t) = V_{RF}\cos(2\pi f_{RF} t) \tag{2.64}
$$

where V_{RF} is the amplitude of the RF signal, f_{RF} is the carrier frequency of the RF signal. We assume that $f_{RF} = 20\ GHz$. Fig. 2.15 shows different optical spectrums of MZM output with different DC voltages applied to the MZM.

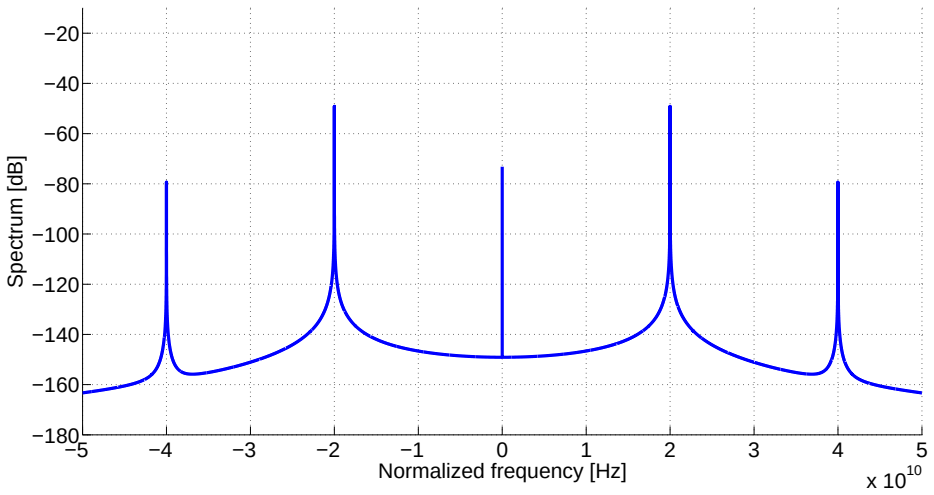

(a) minimum transmission ($V_{DC}=V_\pi$)

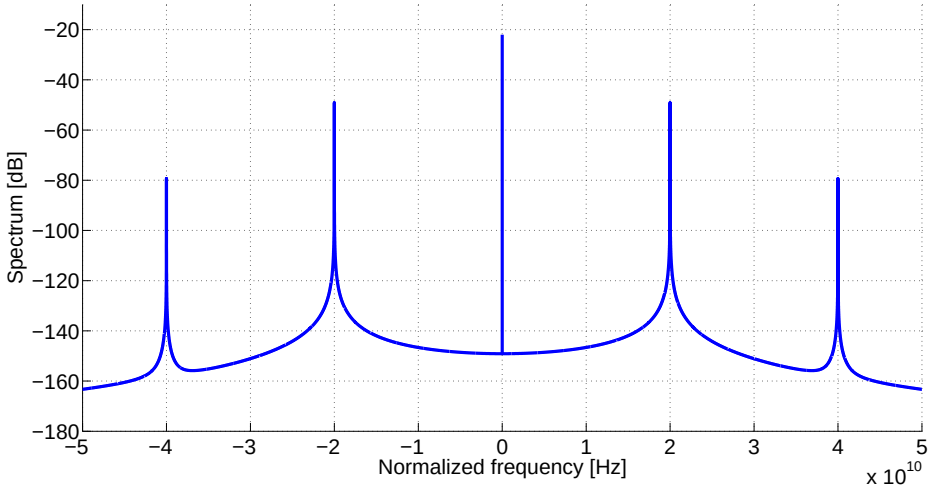

(b) linear transmission (V_{DC}=0.5$V\pi$)

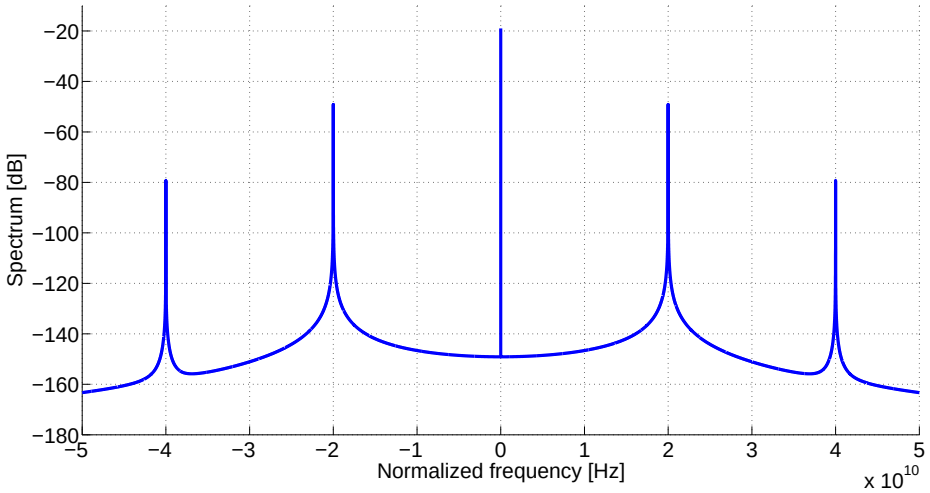

(c) maximum transmission (V_{DC}=0)

Fig. 2.15. Simulation of the output optical spectrum of the MZM as single-arm function

Fig. 2.15 proves that the output optical sidebands don't depend on the DC voltage, when LO signal is only applied to one waveguide. Fig. 2.16 shows the experimental demonstration with different optical spectrum of the MZM output for different bias voltage. The carrier frequency of the RF signal applied to the MZM is setup to 20 GHz corresponding to the setup of the simulation shown as Fig. 2.15.

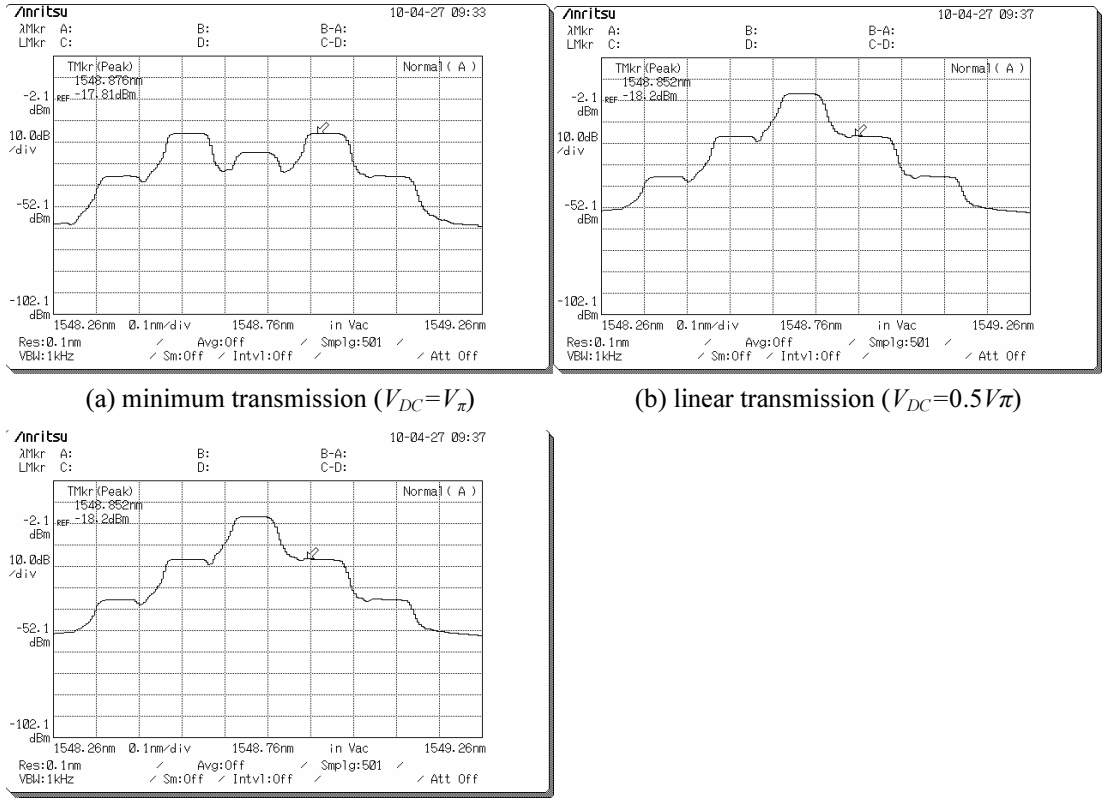

(a) minimum transmission (V_{DC}=V_{π}) (b) linear transmission (V_{DC}=0.5$V\pi$)

(c) maximum transmission (V_{DC}=*0*)

Fig. 2.16. Experimental result of the output optical spectrum of the MZM as single-arm function

Furthermore, we measured the EVM value without DC voltage applied to MZM #2 compared with the EVM value with DC voltage applied to MZM #2. From Tab. 2.3, it can be seen that the EVM with unbiased MZM #2 is slightly higher than the EVM with biased MZM #2, since the power of the CW signal at $2f_{LO}$ is much higher with unbiased MZM #2. Although the broadband mmW at the output of PD is with the same power, the amplifier connected with the PD is saturated by this CW signal. As consequence, the amplified broadband mmW is less powerful. Despite on this, the degradation of the broadband mmW is negligible, as seen from Tab. 2.3.

Tab. 2.3. EVM measurements with unbiased MZM #2

Data Rate (Mbps)	EVM with unbiased MZM #2	EVM with biased MZM #2
397	7.41	7.18
794	9.94	9.57
1588	13.39	12.56

Both experimental results and theoretical analysis of the single-arm MZM indicates that it is unnecessary to bias MZM #2, since the optical mmW is generated by the beating between the optical sideband and the optical field in another optical channel

of DEMUX. In the section 3.4, we will further inquire the MZM using the conclusion of the single-arm MZM.

2.4.2.3 Demonstration of phase noise impact to EVM value

As it has been discussed before (section 2.2), the unequal optical paths of the two DEMUX channels can induce phase noise to the broadband signal generated by the self-heterodyne detection. Fig. 2.17 shows the measured spectrum and the constellation diagrams for BPSK signals with different data rates after optical self-heterodyning without any optical delay adapter, so that the optical path difference is equivalent to 1.08 m fiber. To see clearly the phase noise impact on the spectrum, the $2f_{LO}$ signal at $2f_{LO}$ =51.32 GHz, which is not modulated by data, is down-converted to 9 GHz.

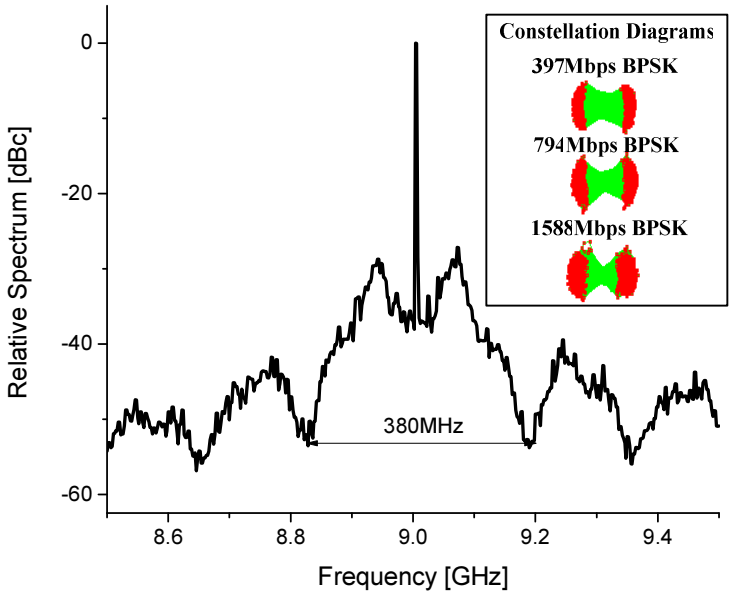

Fig. 2.17 Measured relative spectrum of the CW optical mmW at 51.32 GHz after electrical down-conversion, τ_d/τ_{cOP}=0.051. Inset: constellation diagrams of 58.32 GHz BPSK signals with 397 Mbps, 794 Mbps, 1588 Mbps respectively.

Constellation diagram (inset in Fig. 2.17) of the electrically downconverted $2f_{LO}$ $+f_{IF}$ exhibits arcs of circle. Both spectrum and constellation diagrams match very well simulation results shown in Fig. 2.4. BPSK constellation diagram at 1588 Mbps exhibits thicker arcs compared to the simulation results (inset Fig. 2.4) because of the significant impact of the photodetected ASE/signal beat noise from EDFA, which has not been taken into account in the theoretical model for simplicity. In the experiment, both amplitude noise and phase noise degrade the output signal EVM. EVM

measurements for $|\tau_d|/\tau_{cOP} = 0.051$, which corresponds to 1.08 m different optical fiber length between the two WDM channels (Fig. 2.11) and 1.5 MHz full linewidth of the laser source, are reported in Tab. 2.4, compared with the EVM results under perfect optical length matching ($|\tau_d|/\tau_{cOP} = 0$).

Tab. 2.4. EVM measurements with optical phase to intensity noise conversion after electrical down-conversion $|\tau_d|/\tau_c = 0.051$

Data Rate (Mbps)	EVM under $\|\tau_d\|/\tau_c = 0.051$	EVM under $\|\tau_d\|/\tau_c = 0$
397	22.3	7.18
794	24.7	9.57
1588	27.3	12.56

The phase jitter variances of the LO signal ($\sigma_{\phi LO}^2$) and of the IF signal ($\sigma_{\phi IF}^2$) have been already obtained by integrating the normalized phase noise PSD of the LO and IF generators in Fig. 2.10 and reported in (2.58).

Since we know the EVM value under the perfect optical length matching ($\tau_d/\tau_{cOP} = 0$), the output SNR of the optical self-heterodyning system can be evaluated for the different BPSK data rates using (2.51) and (2.58). When the optical path difference is not null, EVM can be evaluated using (2.51), considering the previously calculated SNR. Tab. 2.5 shows the calculated output SNR and expected EVM values assuming $|\tau_d|/\tau_{cOP} = 0.051$ after the aforementioned approach. Comparing Tab. 2.4 (for $|\tau_d|/\tau_{cOP} = 0.051$) and Tab. 2.5, the simulation results are closed to the measurement results.

Tab. 2.5. SNR and EVM of the BPSK signal by theoretical approach

Data Rate(Mbps)	397	794	1588
SNR (dB)	24.0	21.0	18.4
EVM (%)	23.5	24.4	25.7

Fig. 2.18 shows the simulation curve of EVM from (2.51) as a function of $|\tau_d|/\tau_c$ for different data rates in our system. EVM limitations for ECMA 387 standard, for the different data rates, are also reported on Fig 2.18.

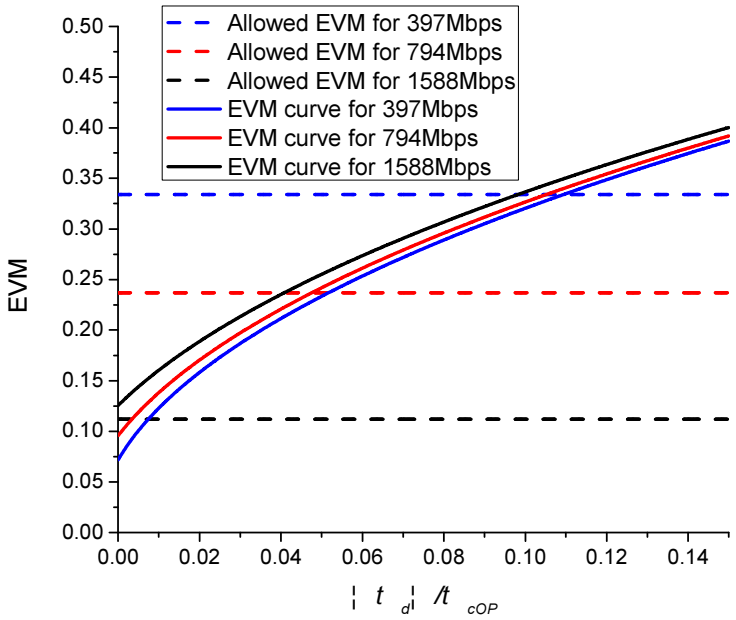

Fig. 2.18. EVM as a function of $|\tau_d|/\tau_{cOP}$ for different data rate optical BPSK signal

According to maximum allowed EVM values given by ECMA 387 standard which are shown in Tab. 2.2 (i) and reported on Fig. 2.18, equation (2.50) gives the maximum acceptable values of $|\tau_d|/\tau_{cOPs}$ for BPSK signal of different data rate generated by our system, which are shown in Tab. 2.6. Hence, we give the maximum optical path difference considering our 1.5 MHz full linewidth the laser source.

Tab. 2.6. Max values of $|\tau_d|/\tau_{cOP}$ for BPSK signal compliant with ECMA 387 standard with laser full linewidth of 1.5 MHz

Data Rate(Mbps)	397	794	1588
Maximum $\|\tau_d\|/\tau_{cOP}$	0.107	0.046	X
Maximum optical path difference (m)	2.27	0.98	X

As it can be seen in Tab. 2.6, for the highest data rate of 1588 Mbps, maximum τ_d/τ_c cannot be defined because EVM requirements for the ECMA 387 standard is not achieved even with perfect optical path matching, since the SNR for the 1588 Mbps signal in our system is already over the limitation to meet the requirement of ECMA 387 standard. Maximum optical path differences found for 397 Mbps and 794 Mbps (Tab. 2.6) are in the range of what it can be achieved with commercial pigtailed components. Even if we would use a DFB laser with a higher linewidth of 20 MHz, maximum optical path difference for 397 Mbps and 794 Mbps would decrease but in the range of several centimeters which would be still feasible using commercial

components. For the highest data rate of 1588 Mbps, supposing that we manage to improve SNR to fulfill ECMA requirement when $|\tau_d|$=0, accurate optical path matching will be more challenging because the margin separating the optimum EVM when $|\tau_d|$=0 to the maximum acceptable EVM value will be smaller than for the lower data rates, and also because EVM as a function of $|\tau_d|/\tau_{cOP}$ increases faster when $|\tau_d|/\tau_{cOP}$ is close to zero (Fig. 2.18).

2.5 Conclusions

In this chapter, the total phase noise of the optically generated mmW has been theoretically analyzed and experimentally demonstrated by integrating the phase noise contribution of the optical phase to intensity noise conversion, which is induced by a delay in one arm of the self-heterodyning detection, and the RF signals from the electrical generators, which are applied to realize optical frequency conversion. Hence, based on the theoretical investigation on the phase noise, the EVM value as a function of $|\tau_d|/\tau_{cOP}$ is theoretically deduced and the law of maximum allowed optical path difference is obtained, which would be the key point of WDM DEMUX application on optical mmW generation. Based on the investigation of phase noise issue in the optical self-heterodyning technique using WDM DEMUX, the generation of broadband optical mmW which follows the ECMA 387 standard is experimentally demonstrated. The proof-of-concept of optical heterodyning mmW generation is successfully demonstrated for ECMA 387 standard . Moreover, the model of EVM as a function of $|\tau_d|/\tau_{cOP}$ is proved experimentally. Optical self-heterodyning systems, as we developed with WDM DEMUX, appear to be sensitive to optical path difference for multigigabit per second mmW. Integrated optics could be a suitable technology to control with good accuracy the optical path difference and reduce phase to intensity noise conversion.

References of chapter 2

[1] T. Nakasyotani, *et al.*, "Wavelength-division-multiplexed millimeter-waveband radio-on-fiber system using a supercontinuum light source," *Journal of Lightwave Technology,* vol. 24, pp. 404-410, Jan 2006.

[2] D. Taggart and R. Kumar, "Impact of phase noise on the performance of the QPSK modulated signal," in *Aerospace Conference, 2011 IEEE*, 2011, pp. 1-10.

[3] Y. Xingwen, *et al.*, "Phase Noise Effects on High Spectral Efficiency Coherent Optical OFDM Transmission," *Lightwave Technology, Journal of,* vol. 26, pp. 1309-1316, 2008.

[4] T. Kuri, *et al.*, "Characterizations of supercontinuum light source for WDM millimeter-wave-band radio-on-fiber systems," *Photonics Technology Letters, IEEE,* vol. 17, pp. 1274-1276, 2005.

[5] M. L. Dennis, *et al.*, "Photonic upconversion of 60 GHz IEEE 802.15.3c standard compliant data signals using a dual-wavelength laser," in *IEEE Photonics Society, 2010 23rd Annual Meeting of the*, 2010, pp. 383-384.

[6] C. Xiangfei, *et al.*, "Photonic generation of microwave signal using a dual-wavelength single-longitudinal-mode fiber ring laser," *Microwave Theory and Techniques, IEEE Transactions on,* vol. 54, pp. 804-809, 2006.

[7] N. Satyan, *et al.*, "Coherent Power Combination of Semiconductor Lasers Using Optical Phase-Lock Loops," *Selected Topics in Quantum Electronics, IEEE Journal of,* vol. 15, pp. 240-247, 2009.

[8] A. Hirata, *et al.*, "Low-phase noise photonic millimeter-wave generator using an AWG integrated with a 3-dB combiner," in *Microwave Photonics, 2004. MWP'04. 2004 IEEE International Topical Meeting on*, 2004, pp. 209-212.

[9] P. T. Shih, *et al.*, "WDM up-conversion employing frequency quadrupling in optical modulator," *Optics Express,* vol. 17, pp. 1726-1733, 2009.

[10] M. R. Salehi and B. Cabon, "Theoretical and experimental analysis of influence of phase-to-intensity noise conversion in interferometric systems," *Journal of Lightwave Technology,* vol. 22, pp. 1510-1518, 2004.

[11] M. Poulin, *et al.*, "Effect of laser decorrelation on the phase noise of RF signals generated by optical mixing of modulation sidebands," in *Microwave Photonics (MWP), 2010 IEEE Topical Meeting on*, 2010, pp. 253-256.

[12] L. B. Mercer, "1/f Frequency Noise Effects on Self-Heterodyne Linewidth Measurements," *Journal of Lightwave Technology,* vol. 9, pp. 485-493, Apr 1991.

[13] P. Gallion and G. Debarge, "Quantum Phase Noise and Field Correlation in Single Frequency Semiconductor Laser Systems," *Quantum Electronics, IEEE Journal of,* vol. 20, pp. 343-349, 1984.

[14] L. S. Cutler and C. L. Searle, "Some aspects of the theory and measurement of frequency fluctuations in frequency standards," *Proceedings of the IEEE,* vol. 54, pp. 136-154, 1966.

[15] ECMA387. http://www.ecma-international.org/publications/standards/Ecma-387.htm.

[16] A. Georgiadis, "Gain, phase imbalance, and phase noise effects on error vector

magnitude," *Vehicular Technology, IEEE Transactions on,* vol. 53, pp. 443-449, 2004.

[17] *Agilent Waveguide Harmonic Mixers M1970V 50 GHz to 75/80 GHz M1970W 75 GHz to 110 GHz*

[18] F. Hoeksema*, et al.*, "Spectral Weighting Functions for Single-symbol Phase-noise Specifications in OFDM Systems," presented at the 8th Intemnational OFDM Workshop, Hamburg, 2003.

Chapter 3

Convergence of RoF and WDM-PON system

3.1 Introduction

In the last chapter, we have inquired the phase noise impact in the RoF system using WDM DEMUX, which includes the optical phase to intensity noise conversion and phase noise from the pure RF signal applied for optical frequency conversion. Low phase noise CW mmW is generated with this RoF system using WDM DEMUX. Moreover, the generation of broadband mmW by optical self-heterodyning technique using WDM DEMUX is demonstrated. In this chapter, we will concentrate on the combination of optical self-heterodyning technique and WDM-PON networks, which we call WDM-RoF system. As we have mentioned in chapter 1, the proposed WDM-RoF system should meet the following requirements:

i) The broadband mmW generated by optical heterodyning should be compliant with the ECMA 387 standard [1].

ii) The length of optical links should meet the demands of FTTH.

iii) The WDM-RoF system should be compatible with simultaneous mmW transmission and base band transmission for WDM-PON requirement.

iv) The WDM-RoF system should be designed for low cost.

According to these targets, the Chapter 3 will be organized in three parts. Firstly, we will inquire the broadband mmW generation by optical heterodyning using WDM DEMUX. Hence, we will propose a new RoF system compatible with simultaneous baseband transmission. The new concept of RoF over WDM PON infrastructure will be developped. The baseband signal and the data stream for mmW will be transmitted in different optical channels. In order to lower the cost of the infrastructure, a new WDM-RoF system with the multi-band modulation technique by one modulator is proposed and experimentally demonstrated finally.

3.2 Combination of optical self-heterodyning technique and baseband transmission

3.2.1 Experimental setup

In the last chapter, broadband mmW generation using WDM DEMUX has been experimentally demonstrated. As it is said in Chapter 1, the WDM-RoF system is proposed for both mmW generation and baseband transmission. In the RoF system, the broadband mmW is generated by optical heterodyning of the optical fields in WDM DEMUX channel #2 and channel #4. To make the RoF system compatible with the baseband transmission, a natural idea is to implement baseband modulation in another free optical channel, such as channel #3.

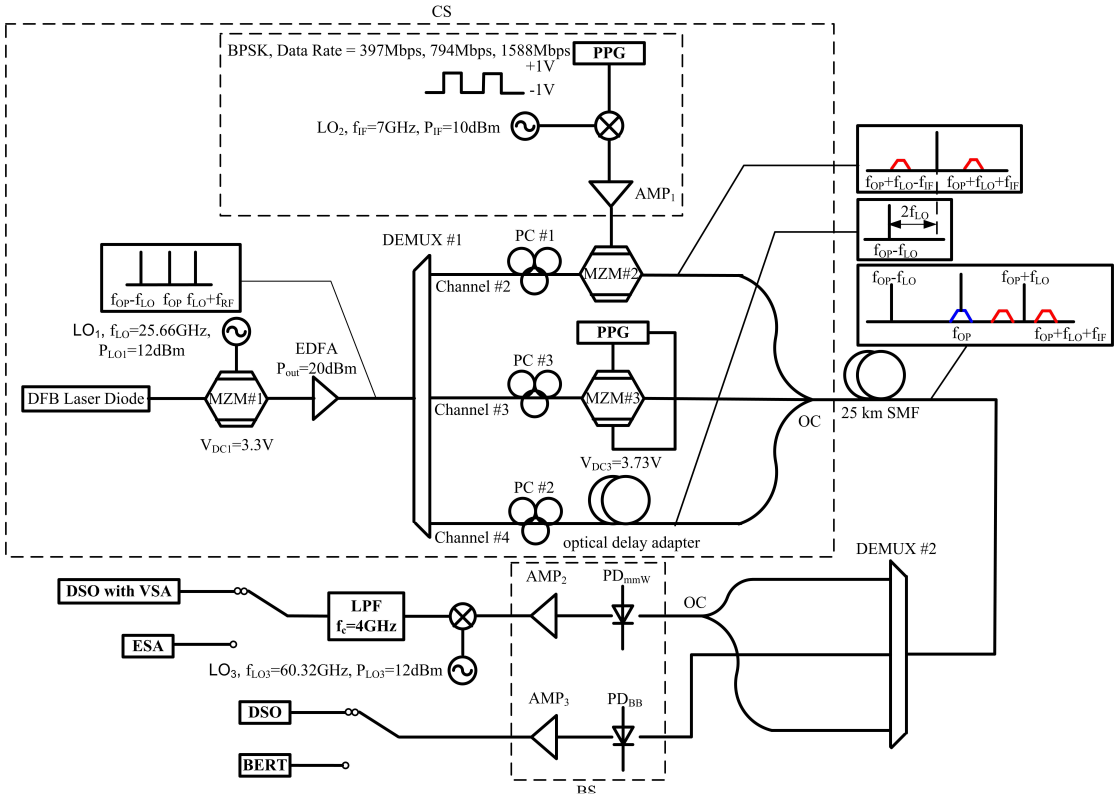

Fig. 3.1. Experimental setup of RoF system for broadband mmW generation and baseband transmission CS: Center Station, BS: Base Station, MZM: Mach-Zehnder Modulator, LO: Local oscillator, EDFA: Erbium-Doped Fiber Amplifier, DEMUX: WDM Demultiplex, PC: Polarization Controller, PPG: Pulse Pattern Generator, AMP: electrical Amplifier, OC: Optical Coupler, SMF: Single Mode Fiber, PD: Photo Diode, LPF: Low Pass Filter, DSO: Digital Storage Oscilloscope, VSA: Vector Signal Analyzer software, ESA: Electrical Spectrum Analyzer

Fig. 3.1 shows the experimental setup for mmW generation and baseband transmission. The experimental setup for the mmW generation is the same as Fig. 2.11, except that the MZM #1 behaving as single-arm MZM is biased at linear regime. As a result, there is significant optical power in channel #3 of the WDM DEMUX. Another Mach-Zehnder Modulator (MZM #3) is used for the baseband modulation. The baseband data stream with a non-return-zero (NRZ) pseudo random bit sequence (PRBS) of 2^{31}-1 is generated by another Pulse Pattern Generator (PPG #2) and is applied to the two electrodes of the MZM #3, which is biased in linear regime. Here, we need to mention that MZM #3 works as push-pull modulator. As the configuration of channel #2, another Polarization Controller (PC #2) is employed to adjust the input optical polarization for MZM #3.

The optical fields in the three optical channels are combined by using an optical coupler and transmitted to the BS by 25 km single mode fiber (SMF). To separate the optical field for mmW generation and optical field for baseband detection, another DEMUX (DEMUX #2) with the same channel frequencies as DEMUX #1 is employed before the BS.

The BS is composed of two receivers for mmW and baseband signal respectively. Channel #2 and Channel #4 of the DEMUX #2 are recombined by an optical coupler and sent to the mmW receiver, which is made up of a PD exhibiting a 70 GHz bandwidth cascaded with an electrical amplifier (AMP_2). Channel #3 of the DEMUX #2 carries the baseband data stream to the baseband receiver in BS. A 10 GHz bandwidth PD is employed to detect the baseband signal. The optical mmW is firstly down-converted to 2 GHz band by using an electrical mixer driven by 60.32 GHz LO_3 signal. The down-converted signal is either sent to a Digital Storage Oscilloscope (DSO) and demodulated by the Vector Signal Analyzer (VSA) software (Agilent) or analyzed by using an Electrical Spectrum Analyzer (ESA). The baseband signal is either sent to the Bit Error Rate Tester (BERT) to measure the Bit Error Rate (BER) or to the DSO for the eye diagram display.

3.2.2 Experimental results

3.2.1.1 Broadband mmW generation by optical self-heterodyning

The electrically down-converted signal is digitalized with the Digital Storage Oscilloscope (DSO) and demodulated by the Vector Signal Analyzer (VSA) software. The constellation diagrams, eye diagrams and EVM results for 397 Mbps, 794 Mbps and 1588 Mbps are shown in Fig. 3.2 and Tab. 3.1 respectively.

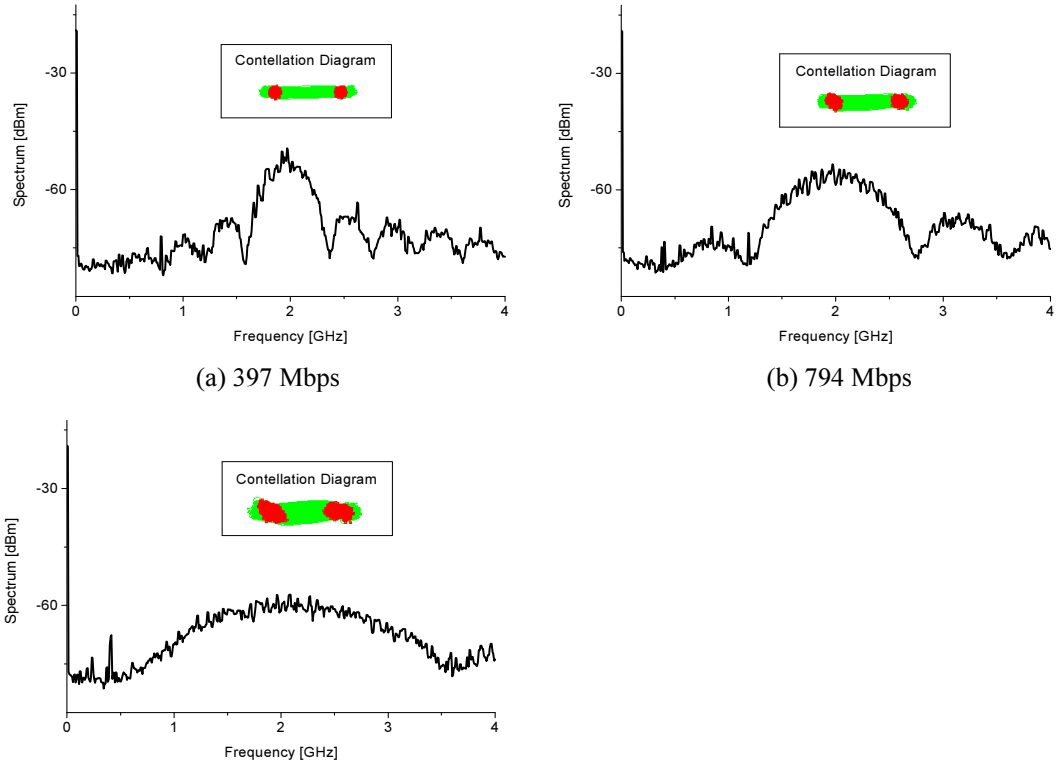

(a) 397 Mbps

(b) 794 Mbps

(c) 1588Mbps

Fig. 3.2. Spectrums of optical broadband optical mmW down-converted to 2 GHz band. Inset: constellation diagrams.

EVMs for different data rate are reported in Tab. 3.1, compared with the EVM requirements according to ECMA 387 standard. Comparing measurement results shown in Tab 3.1 (ii) with the EVM requirements according to ECMA 387 standard shown in Tab. 3.1 (i), EVM value of the optical mmW are in the limit of the ECMA 387 standard to insure error free transmission except for the EVM of 1588 Mbps data signal. EVM measurements for the optical generated broadband mmW at 397 Mbps and 794 Mbps meet the requirements of the ECMA 387 standard with a big margin (Tab. 3.1).

The EVM results shown in Tab. 3.1 are slightly better than the previous measurement results shown in Tab. 2.2, since the devices such as optical polarization controller (PC), the electrical amplifiers (AMPs) are better operated in the complex system.

Tab. 3.1. EVM measurements compared with the requirements according to ECMA 387 standard

(i) ECMA387 requirements			
Data Rate (Mbps)	397	794	1588
Maximum allowed EVM (%)	33.4	23.7	11.2
(ii) Output optical mmW by photodetection			
Data Rate (Mbps)	397	794	1588
EVM (%)	6.85	8.90	11.75

3.2.1.2 Baseband transmission

The baseband signal is digitalized with the DSO with the measurement of Q factor, which is defined as:

$$Q = \frac{V_1 - V_0}{\sigma_1 - \sigma_0} \tag{3.1}$$

where V_1 and V_0 are the mean values for amplitude high and low of the baseband signal respectively, σ_1 and σ_2 are the root mean square (RMS) of the Gaussian noise variance in voltage. Fig. 3.3 shows the eye diagrams and Q-factors for 1 Gbps, 2 Gbps, 2.5 Gbps and 10 Gbps baseband signals.

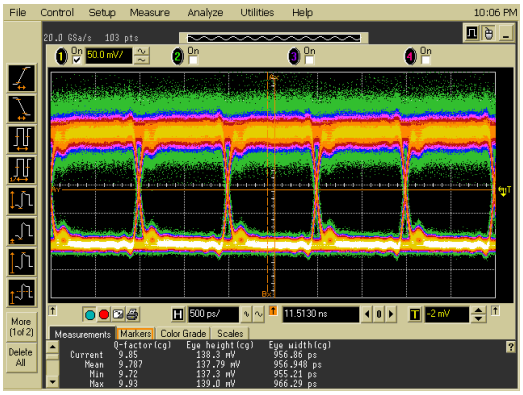

(a) 1 Gbps baseband signal (Q=9.85)

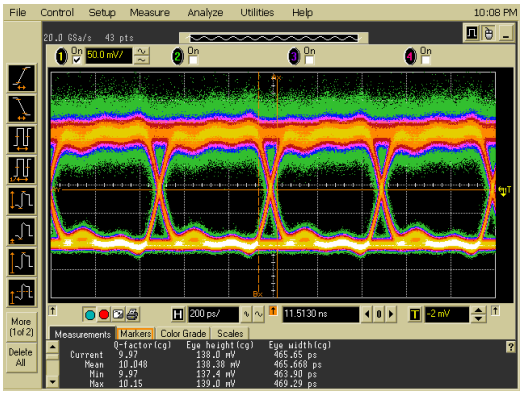

(b) 2 Gbps baseband signal (Q=9.97)

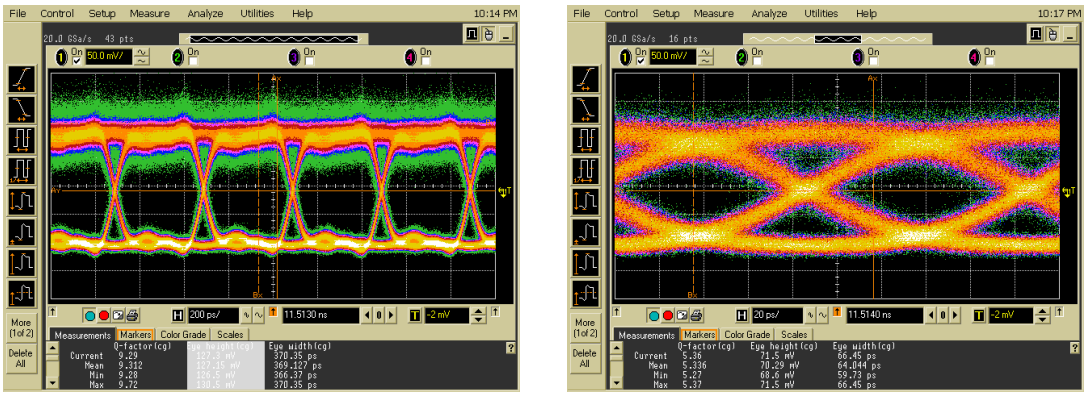

(c) 2.5 Gbps baseband signal (Q=9.3) (d) 10 Gbps baseband signal (Q=5.4)

Fig. 3.3. Eyediagrams for baseband signals

It can be seen that the eye is open from Fig. 3.3. It has been proved that this schematic can support 10 Gbps baseband signal for error free transmission.

3.2.2.3 Radio propagation of broadband mmW

Based on the optical mmW generation, we further test the radio propagation. Fig. 3.4 shows the experimental setup for the radio propagation.

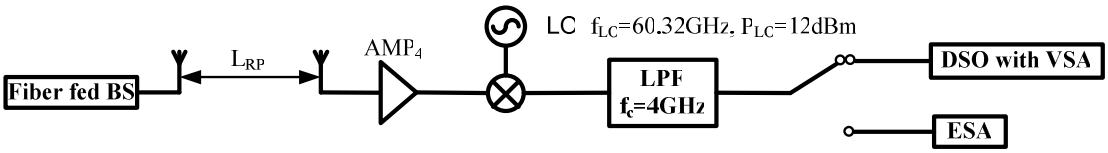

Fig. 3.4. Experimental setup for radio propagation test

Two horn antennas with 20 dB gain each are used for the high data rate radio transmission. In the radio receiver part, a low noise amplifier (AMP_4) with the gain of 24 dB is employed to compensate for the radio propagation loss. The received and amplified binary phase shift keying (BPSK) signal at 58.32 GHz is electronically down-converted using a mixer driven by 60.32 GHz CW signal from LO. The electrically down-converted signal is either digitalized with the Digital Storage Oscilloscope (DSO) and demodulated by the Vector Signal Analyzer (VSA) software (Agilent) or analyzed by using an Electrical Spectrum Analyzer (ESA). Fig. 3.5 shows the spectrums of the optical mmW after 0.5 m air transmission and 1 m air transmission with the constellation diagrams inset.

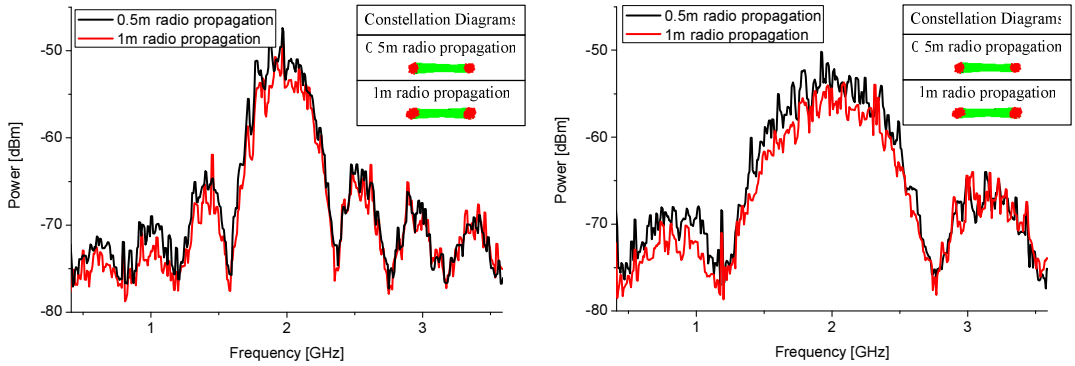

(a) 397 Mbps BPSK signal air transmission (b) 794 Mbps BPSK signal air transmission

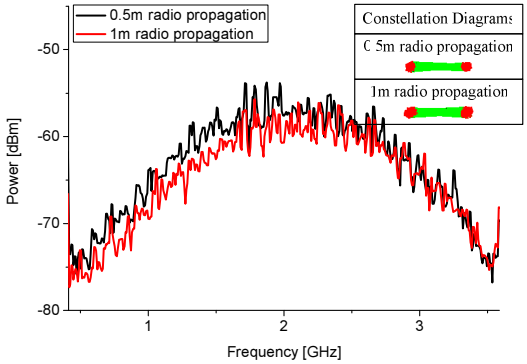

(c) 1588 Mbps BPSK signal air transmission

Fig. 3.5. Spectrums of optical broadband optical mmW after air-transmission and down-converted to 2 GHz band. Inset: constellation diagrams.

EVM and the signal power measured before or after the radio propagation are reported in Tab. 3.2, compared with the EVM requirements according to ECMA 387 standard.

Tab. 3.2. Power and EVM measurements after electrical down-conversion compared with the requirements according to ECMA 387

(i) ECMA387 requirements for transmitter and receiver			
Data Rate (Mbps)	397	794	1588
Maximum emitted power (dBm)	10	10	10
Maximum allowed EVM (%)	33.4	23.7	11.2
Receiver sensitivity (dBm)	-60.0	-57.0	-50.5
(ii) No radio propagation			
Data Rate (Mbps)	397	794	1588
Power after down-conversion (dBm)	-27.49	-27.77	-28.44
Received Power at 58.32 GHz (dBm)	-20.49	-20.77	-21.44
EVM (%)	6.85	8.90	11.75
(iii) 0.5 m radio propagation			
Data Rate (Mbps)	397	794	1588
Power after down-conversion (dBm)	-24.84	-24.84	-25.32

Received power at 58.32 GHz after the antenna (dBm)	-41.84	-41.84	-42.32
EVM (%)	7.33	9.51	12.08
(iv) 1 m radio propagation			
Data Rate (Mbps)	397	794	1588
Power after down-conversion (dBm)	-26.84	-27.20	-27.04
Received power at 58.32 GHz after the antenna (dBm)	-43.84	-44.20	-44.04
EVM (%)	8.69	11.14	15.15

Comparing measurement results (iv) with the EVM requirements according to ECMA 387 standard shown in Tab. 3.2 (i), EVM value after 1m radio propagation are in the limit of the ECMA 387 standard to insure error free transmission except for the EVM of 1588 Mbps data signal. EVM measurements for the optical generated broadband mmW at 397 Mbps and 794 Mbps after radio propagation meet the requirements of the ECMA 387 standard with a big margin.

The received power after 0.5 m radio propagation and 1 m radio propagation are around -42 dBm and -44 dBm respectively, which correspond to the measured down-converted IF power after 24 dB gain AMP_4 and external mixer with 7 dB conversion loss. According to the sensitivity of the receiver defined by the ECMA 387 standard for 1588 Mbps (-50.5 dBm), there is a 6 dB margin for 1588 Mbps BPSK signal after 1m radio propagation.

Tab. 3.2 (ii) shows the measurement result of the BS output signal after electrical down-conversion. The channel power of 1588 Mbps data signal at the BS output can be estimated around -21 dBm, which corresponds to an equivalent isotropic radiated power (EIRP) of -1 dBm (considering a 20 dB horn antenna gain). It is far below the authorized maximum EIRP of 35 dBm[2]. That leaves a large margin to extend coverage distance using larger amplifier gain before radio emission by using an additional power amplifier (PA).

3.3 WDM-RoF system compatible with mmW generation and baseband transmission using multi-band modulation technique

As we said at the beginning of the chapter, the WDM-RoF system is proposed to support numerous users. Although we build up the RoF system which is compatible with mmW generation and baseband signal transmission, it brings additional cost using another MZM in the CS. Besides of the additional cost of the device, we need to reserve an additional optical channel for the baseband transmission which would lower the capacity of the whole system. As a consequence, we need to further inquire another technique to lower the cost of the system and number of optical channels dedicated to one user. In this section, the WDM-RoF system will be built up by using multi-band modulation with one MZM technique. In this section, we test the WDM-RoF system for 25 km optical transmission.

3.3.1 Experimental setup

Fig. 3.6 shows the configuration of the proposed multi-band WDM-RoF system. The system setup for mmW generation in CS is the same as for the RoF system we introduced in section 2.4 (Fig. 2.11). Unlike the system with the combination of baseband and 60 GHz wireless RoF transmission shown in Fig. 3.1, the multi-band modulation technique with one MZM (MZM #2) is applied in CS. An arbitrary waveform generator (AWG) is connected to a wideband modulator PSG to implement an IF band BPSK modulation at f_{IF}=8.82 GHz with the output power of 15 dBm. The selected data rates correspond to the values defined in the ECMA 387 standard. The IF BPSK signal is applied to one electrode of the MZM #2. Moreover, another PPG (PPG #2) is directly fed into the other electrode of the dual-electrode MZM #2 for baseband modulation. The required data rate of the baseband signal is typically higher than 1 Gbps. The 2.5 Gbps BPSK bit stream with a pseudo random bit sequence (PRBS) of 2^{31}-1 and from the PPG is tested in the experiment. As the above RoF

system, the two optical signals from channels #2 and #4 are combined by a 3 dB optical coupler and transmitted through a 25 km long single mode fiber to the remote access node (RAN), in which another DEMUX #2 is employed to separate different spectral lines to different receivers in the BS.

The digitally modulated optical field in channel #2 of DEMUX #2 is divided by an optical coupler in the BS. One is directly sent to the baseband receiver and the other is combined with the optical wave in channel #4 of DEMUX #2 and sent to the mmW receiver in the BS. Regarding the broadband mmW generation, the received optical wave is detected by the 70 GHz bandwidth PD (PDmmW) and amplified by an electrical amplifier (AMP_1) with a gain of 28 dB. A 7 GHz bandwidth PD cascaded with an electrical amplifier (AMP_2) is employed for baseband detection. The baseband signal is either digitalized by the DSO for the display of eye diagram or applied to the Bit Error Rate Tester (BERT).

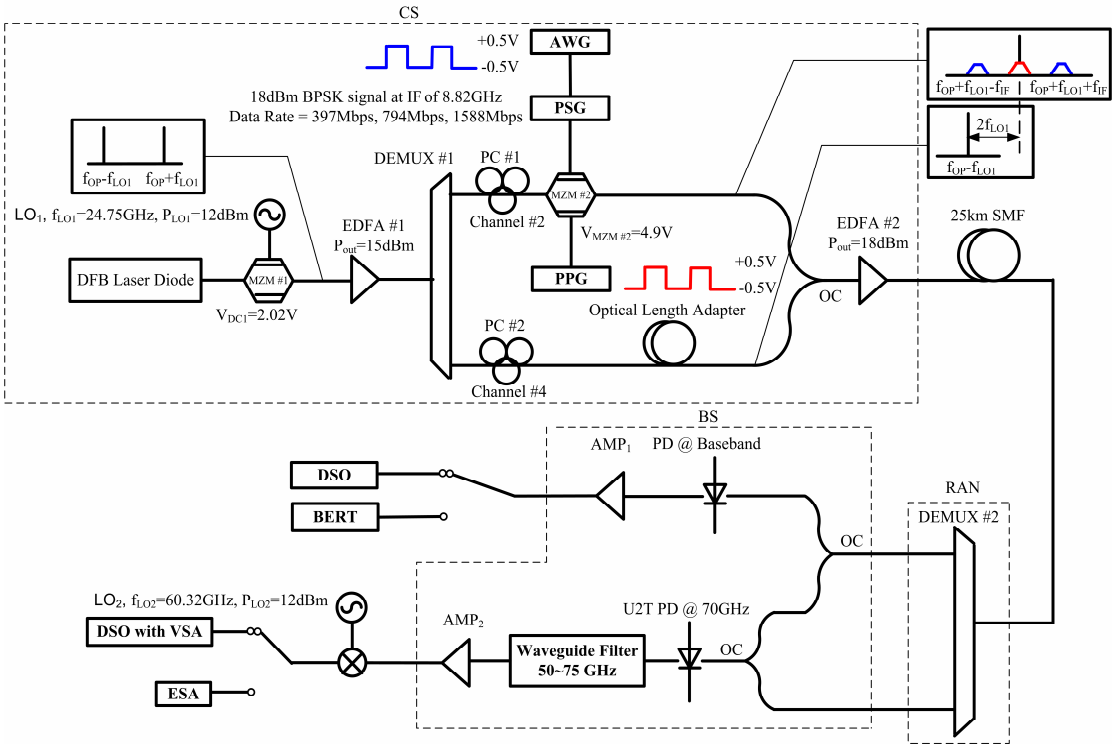

Fig. 3.6. WDM-RoF system using multi-band modulation with one MZM technique.

CS: Central Station, BS: Base Station, DFB Laser: Distributed Feedback Laser, MZM: Mach-Zehnder Modulator, LO: Local oscillator, EDFA: Erbium Doped Fiber Amplifier, DEMUX: WDM Demultiplexer, AWG: Arbitrary Waveform Generator, PPG: Pulse Pattern Generator, PD: Photo Diode, IF: Intermediate Frequency, PC: Polarization Controller, SMF: Single Mode Fiber, AMP: electrical Amplifier, DSO: Digital storage oscilloscope, VSA: Vector Signal Analyzer, ESA: Electrical Spectrum Analyzer, BERT: Bit Error Rate Tester

3.3.2 Theoretical investigation of the parallel phase modulation with one MZM

3.3.3.1. Theoretical model of the parallel phase modulation

Since the WDM-RoF system shown in Fig. 3.7 relies on the multi-band modulation technique with a single MZM, it is necessary to investigate theoretically the multi-band modulation technique. In the proposed WDM-RoF system, the MZM #2 performs as two parallel phase modulators.

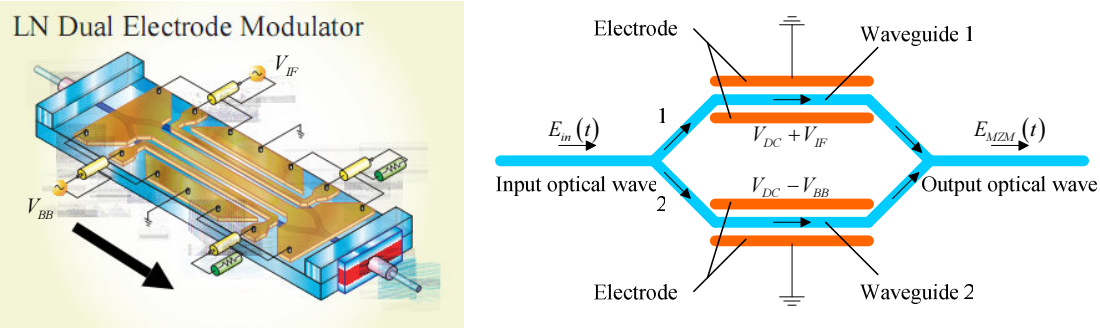

Fig. 3.7. Configuration of the multi-band modulation with single MZM

Fig. 3.7 shows the structure of the MZM used with the multi-band modulation technique. As we mentioned in chapter 2, there are two optical waveguides. Each optical waveguide is biased by a pair of electrodes. A DC voltage is applied to the two pairs of electrodes respectively. Baseband signal $V_{BB}(t)$ is applied to one electrode of MZM #2 (Fig. 3.7) and an IF signal $V_{IF}(t)$ at f_{IF} is applied to the other electrode simultaneously. These signals are expressed as :

$$V_{BB}(t)=\sum_{k=0}^{+\infty}a_k\Pi_{TBB}(t-kT_{BB})$$
$$V_{IF}(t)=s(t)\cos\left(2\pi f_{IF}t+\phi(t)\right) \quad (3.2)$$

where $a_k=\{+A, -A\}$ are the baseband symbols from the PPG, Π_{TBB} is the gate function for the baseband signal with the symbol duration of T_{BB}. Here we generally investigate all the modulation formats for the IF signal. $s(t)$ is the instant amplitude of the IF signal, and $\phi(t)$ is the phase of the IF signal. From equation (3.2), the IF signal is a general analog signal including all the modulation formats, such as phase shift keying (PSK), quadrature amplitude modulation (QAM), or even orthogonal

frequency division multiplexing (OFDM).

The output optical field of MZM #2 is expressed as:

$$E_{MZM\#2} = \frac{1}{2}\frac{1}{\sqrt{I_L}} E_2(t)\left[\exp\left(j\pi\frac{V_{DC}+V_{IF}(t)}{2V_\pi}\right)+\exp\left(-j\pi\frac{V_{DC}-V_{BB}(t)}{2V_\pi}\right)\right]$$
$$= \frac{E_2}{2\sqrt{I_L}}\left[\exp\left(j\left(2\pi(f_{OP}+f_{LO})t+\pi\frac{V_{DC}+V_{IF}(t)}{2V_\pi}\right)\right)+\right. \quad (3.3)$$
$$\left.\exp\left(j\left(2\pi(f_{OP}+f_{LO})t-\pi\frac{V_{DC}-V_{BB}(t)}{2V_\pi}\right)\right)\right]$$

where $E_{MZM\#2}(t)$ is the output optical field of the MZM #2, and $E_2(t)$ is the input optical field of the MZM #2. I_L is the insertion loss of the MZM, which is typically lower than 6 dB. V_{DC} is the DC voltage applied to the MZM #2, V_π is the half wave voltage of MZM #2. f_{LO} is the carrier frequency of LO1 (Fig. 3.6). Equation (3.3) shows that the output optical field of MZM #2 is the combined optical fields of the two optical waveguides. The optical wave in each optical waveguide is phase modulated by the applied voltages.

- **Expression of the photocurrent at mmW band**

In BS, the photocurrent at the mmW receiver i_{PDmmW} is issued from the beating of output optical field from MZM #2 ($E_{MZM\#2}(t)$) and optical field from channel #4 ($E_4(t)$) (Fig. 3.6) and can be written as

$$i_{PD_{mmW}} = \left|E_{MZM\#2}(t)+E_4(t)\right|^2$$
$$= \left[E_{MZM\#2}(t)+E_4(t)\right]\left[E_{MZM\#2}(t)+E_4(t)\right]^* \quad (3.4)$$
$$= \left|E_{MZM\#2}(t)\right|^2+\left|E_4(t)\right|^2+E_{MZM\#2}(t)E_4^*(t)+E_{MZM\#2}^*(t)E_4(t)$$

By using (3.3), equation (3.4) can be derived as:

$$
\begin{aligned}
i_{PD_{mmW}} &= E_4^2 + \frac{E_2^2}{2I_L} + \frac{E_2^2}{4I_L}\exp\left(j\pi \frac{2V_{DC} + V_{IF}(t) - V_{BB}(t)}{2V_\pi} \right) + \frac{E_2^2}{4I_L}\exp\left(-j\pi \frac{2V_{DC} + V_{IF}(t) - V_{BB}(t)}{2V_\pi} \right) + \\
&\frac{E_2 E_4}{2\sqrt{I_L}}\left[\exp\left(j\left(4\pi f_{LO} t + \pi \frac{V_{DC} + V_{IF}(t)}{2V_\pi} \right) \right) + \exp\left(j\left(4\pi f_{LO} t - \pi \frac{V_{DC} - V_{BB}(t)}{2V_\pi} \right) \right) \right] + \\
&\left\{ \frac{E_2 E_4}{2\sqrt{I_L}}\left[\exp\left(j\left(4\pi f_{LO} t + \pi \frac{V_{DC} + V_{IF}(t)}{2V_\pi} \right) \right) + \exp\left(j\left(4\pi f_{LO} t - \pi \frac{V_{DC} - V_{BB}(t)}{2V_\pi} \right) \right) \right] \right\}^* \\
&= E_4^2 + \frac{E_2^2}{2I_L} + \frac{E_2^2}{2I_L}\cos\left(\pi \frac{2V_{DC} + V_{IF}(t) - V_{BB}(t)}{2V_\pi} \right) + \frac{E_2 E_4}{\sqrt{I_L}}\cos\left(4\pi f_{LO} t - \pi \frac{V_{DC} - V_{BB}(t)}{2V_\pi} \right) + \\
&\frac{E_2 E_4}{\sqrt{I_L}}\cos\left(4\pi f_{LO} t + \pi \frac{V_{DC} + V_{IF}(t)}{2V_\pi} \right)
\end{aligned}
\tag{3.5}
$$

The last term of (3.5) contains the optical mmW at the frequency $2f_{LO} + f_{IF}$.

$$
\begin{aligned}
&\frac{E_2 E_4}{\sqrt{I_L}}\cos\left(4\pi f_{LO} t + \pi \frac{V_{DC} + V_{IF}(t)}{2V_\pi} \right) \\
&= \frac{E_2 E_4}{\sqrt{I_L}}\cos\left(4\pi f_{LO} t + \pi \frac{V_{DC}}{2V_\pi} \right)\cos\left(\pi \frac{s(t)\cos\left(2\pi f_{IF} t + \phi(t)\right)}{2V_\pi} \right) - \\
&\frac{E_2 E_4}{\sqrt{I_L}}\sin\left(4\pi f_{LO} t + \pi \frac{V_{DC}}{2V_\pi} \right)\sin\left(\pi \frac{s(t)\cos\left(2\pi f_{IF} t + \phi(t)\right)}{2V_\pi} \right)
\end{aligned}
\tag{3.6}
$$

By using the Jacobi-Anger expansion:

$$
\begin{aligned}
\cos(z\cos\theta) &= J_0(z) + 2\sum_{n=1}^{\infty}(-1)^n J_{2n}(z)\cos(2n\theta) \\
\sin(z\cos\theta) &= -2\sum_{n=1}^{\infty}(-1)^n J_{2n-1}(z)\cos\left[(2n-1)\theta\right]
\end{aligned}
\tag{3.7}
$$

where $J_n(z)$ is n-order Bessel function of the first kind. It can be seen that the last term of the equation (3.6) contains the broadband mmW at $2f_{LO}+f_{IF}$. The last term of equation (3.6) can be derived as

$$
\begin{aligned}
&\frac{E_2 E_4}{\sqrt{I_L}}\sin\left(4\pi f_{LO} t + \pi \frac{V_{DC}}{2V_\pi} \right)\sin\left(\pi \frac{s(t)\cos\left(2\pi f_{IF} t + \phi(t)\right)}{2V_\pi} \right) \\
&= \frac{-2E_2 E_4}{\sqrt{I_L}}\sin\left(4\pi f_{LO} t + \pi \frac{V_{DC}}{2V_\pi} \right)\sum_{n=1}^{\infty}(-1)^n J_{2n-1}\left(\pi \frac{s(t)}{2V_\pi} \right)\cos\left[(2n-1)\left(2\pi f_{IF} t + \phi(t)\right)\right]
\end{aligned}
\tag{3.8}
$$

By using equation (3.8), the mmW at $2f_{LO} + f_{IF}$ can be derived as

$$i_{mmW} = \frac{-E_2 E_4}{\sqrt{I_L}} J_1\left(\pi \frac{s(t)}{2V_\pi}\right) \sin\left(2\pi\left(2f_{LO} + f_{IF}\right)t + \pi \frac{V_{DC}}{2V_\pi} + \phi(t)\right) \tag{3.9}$$

Fig. 3.8 shows the first-order Bessel function of the first kind ($y=J_1(z)$). It can be seen that when $z<1$, the first-order Bessel function of the first kind is in linear. In practice, V_π is 5V, and the average power of the IF signal is lower than 20 dBm so that $s(t)<3.2$ V. In this case $\pi s(t) / 2V_\pi < 1$, the photodetected mmW can be recovered without significant distortion. We need to mention that the model is valid for different modulation formats compliant with ECMA 387 or IEEE 815.3c requirements. From (3.9), it can be seen that there is no impact from the baseband modulation on the mmW signal, since the mmW signal is actually generated from a single beating between the optical sideband in channel #2 generated by phase modulation and a pure CW optical spectral line in channel #4 (Fig. 3.6). Moreover, the mmW does not depend on the bias voltage of MZM #2. In chapter 2, we have concluded that the bias voltage of the MZM #2 does not impact the mmW generation, when MZM #2 works as single-arm MZM. Here the MZM #2 performs as parallel phase modulators. For mmW generation, it plays the same role as a single-arm MZM.

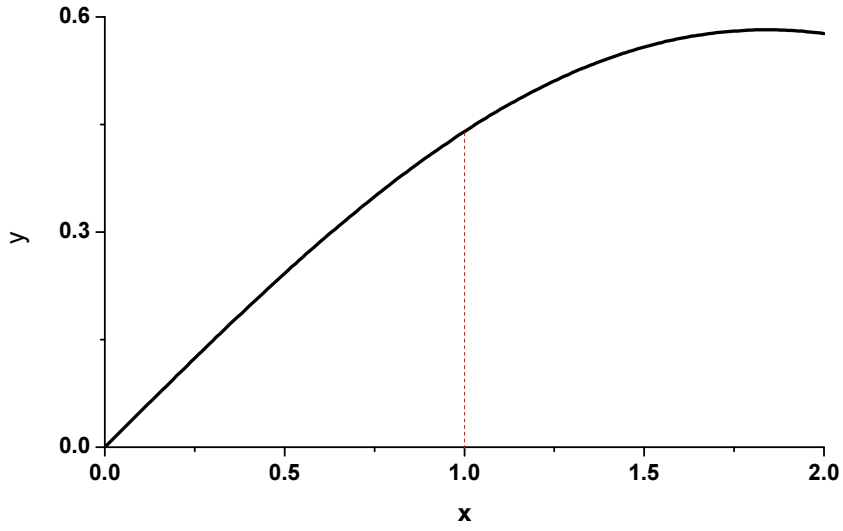

Fig. 3.8. First-order Bessel function of the first kind

- **Expression of the photocurrent at baseband**

The photocurrent at the baseband receiver i_{PDBB} is expressed as:

$$
\begin{aligned}
&i_{PD_{BB}} = k_2 \left| E_{MZM\#2}(t) \right|^2 \\
&= \frac{k_2 E_2}{2\sqrt{I_L}} \left[\exp\left(j\left(2\pi \left(f_{OP} + f_{LO} \right) t + \pi \frac{V_{DC} + V_{IF}(t)}{2V_\pi} \right) \right) + \exp\left(j\left(2\pi \left(f_{OP} + f_{LO} \right) t - \pi \frac{V_{DC} - V_{BB}(t)}{2V_\pi} \right) \right) \right] \times \\
&\left\{ \frac{E_2}{2\sqrt{I_L}} \left[\exp\left(j\left(2\pi \left(f_{OP} + f_{LO} \right) t + \pi \frac{V_{DC} + V_{IF}(t)}{2V_\pi} \right) \right) + \exp\left(j\left(2\pi \left(f_{OP} + f_{LO} \right) t - \pi \frac{V_{DC} - V_{BB}(t)}{2V_\pi} \right) \right) \right] \right\}^* \\
&= \frac{k_2 E_2^2}{2I_L} + \frac{k_2 E_2^2}{4I_L} \exp\left(j\pi \frac{2V_{DC} + V_{IF}(t) - V_{BB}(t)}{2V_\pi} \right) + \frac{E_2^2}{4I_L} \exp\left(-j\pi \frac{2V_{DC} + V_{IF}(t) - V_{BB}(t)}{2V_\pi} \right) \\
&= \frac{k_2 E_2^2}{2I_L} + \frac{k_2 E_2^2}{2I_L} \cos\left(\pi \frac{2V_{DC} + V_{IF}(t) - V_{BB}(t)}{2V_\pi} \right) \\
&= \frac{k_2 E_2^2}{2I_L} + \frac{k_2 E_2^2}{2I_L} \cos\left(\pi \frac{2V_{DC} - V_{BB}(t)}{2V_\pi} \right) \cos\left(\pi \frac{V_{IF}(t)}{2V_\pi} \right) - \frac{E_2^2}{2I_L} \sin\left(\pi \frac{2V_{DC} - V_{BB}(t)}{2V_\pi} \right) \sin\left(\pi \frac{V_{IF}(t)}{2V_\pi} \right)
\end{aligned}
\tag{3.10}
$$

By using the Jacobi-Anger expansion in (3.7), equation (3.10) can be derived as:

$$
\begin{aligned}
&i_{PD_{BB}} = \frac{k_2 E_2^2}{2I_L} + \frac{k_2 E_2^2}{2I_L} J_0\left(\pi \frac{s(t)}{2V_\pi} \right) \cos\left(\pi \frac{2V_{DC} - V_{BB}(t)}{2V_\pi} \right) + \\
&\frac{k_2 E_2^2}{I_L} \cos\left(\pi \frac{2V_{DC} - V_{BB}(t)}{2V_\pi} \right) \sum_{n=1}^{\infty} (-1)^n J_{2n}\left(\pi \frac{s(t)}{2V_\pi} \right) \cos\left[2n\left(2\pi f_{IF} t + \phi(t) \right) \right] + \\
&\frac{k_2 E_2^2}{I_L} \sin\left(\pi \frac{2V_{DC} - V_{BB}(t)}{2V_\pi} \right) \sum_{n=1}^{\infty} (-1)^n J_{2n-1}\left(\pi \frac{s(t)}{2V_\pi} \right) \cos\left[(2n-1)\left(2\pi f_{IF} t + \phi(t) \right) \right]
\end{aligned}
\tag{3.11}
$$

it can be seen that the second term of (3.11) represents the baseband component. The third and fourth term in (3.11) express the components at harmonic frequencies of IF carrier. By using a lowpass filter, the baseband signal can be easily selected. Equation (3.9) also indicates that MZM #2 has to be biased in linear regime ($V_{DC}=0.5V_\pi$) in order to obtain the maximum output of baseband signal.

Finally only the baseband signal is extracted from baseband receiver and can be derived as:

$$
i_{BB} = \frac{k_2 E_2^2}{2I_L} J_0\left(\pi \frac{s(t)}{2V_\pi} \right) \cos\left(\pi \frac{2V_{DC} - V_{BB}(t)}{2V_\pi} \right) \tag{3.12}
$$

Equation (3.12) indicates that RF modulation will bring interference to the baseband photocurrent i_{BB}, which depends on the amplitude of the IF signal *s(t)*. The impact factor F_i of the IF modulation to the baseband signal is defined as

$$F_i = J_0\left(\pi \frac{s(t)}{2V_\pi}\right) \tag{3.13}$$

If we consider a BPSK signal, despite of the constant amplitude for BPSK, IF signal (*s(t)=constant*), will degrade the power and so signal to noise ratio (SNR) of the baseband signal because $J_0(X)<1$ for $X\neq 0$. If the IF modulation contains amplitude modulation technique, such as QAM modulation, the amplitude of IF signal is not constant. In this case, the amplitude modulation component of the I/Q modulation for the IF signal will be overlaid on the photodetected baseband signal. Fig. 3.9 shows impact factor of the IF modulation to the baseband signal as a function of the IF signal amplitude. The half-wave voltage of MZM #2 V_π is set to 5 V according to the experiment setup.

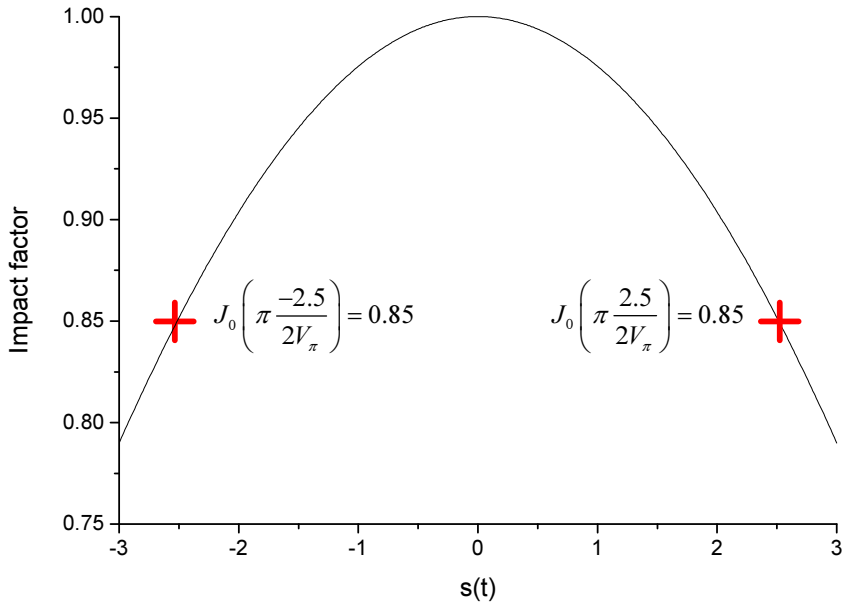

Fig. 3.9. Impact factor of the IF modulation.

In our experimental setup, the IF modulation is BPSK modulation with the output power of 18 dBm. The amplitude *s(t)* is then 2.5V. From Fig. 3.8, we can see that the power degradation on i_{BB} induced by the RF modulation is around 15%. This impact will be proved experimentally in the next section.

Now we consider that IF band modulation is 16-QAM. The output power of the IF signal is 18 dBm. In this case, the amplitude $|s(t)|$ has three possible values ($|s(t)|$={1.1V, 2.5V, 3.4V}) as shown in Fig. 3.10 (a). The impact of the RF

modulation on the eye diagram of the baseband signal is shown in Fig. 3.10 (b), by means of simulations. Unlike the PSK modulation, the QAM modulation or any other amplitude modulation will not only induce an average power degradation of baseband signal, but will also cause the amplitude fluctuation of the baseband signal. This fluctuation could be restricted by limiting the modulation depth of the amplitude modulation. Moreover, it can be predicted that IF modulation with high peak to average power ratio (PAPR) will induce significant larger impact than constant envelope modulations to the baseband signal, which will be demonstrated experimentally in the next section.

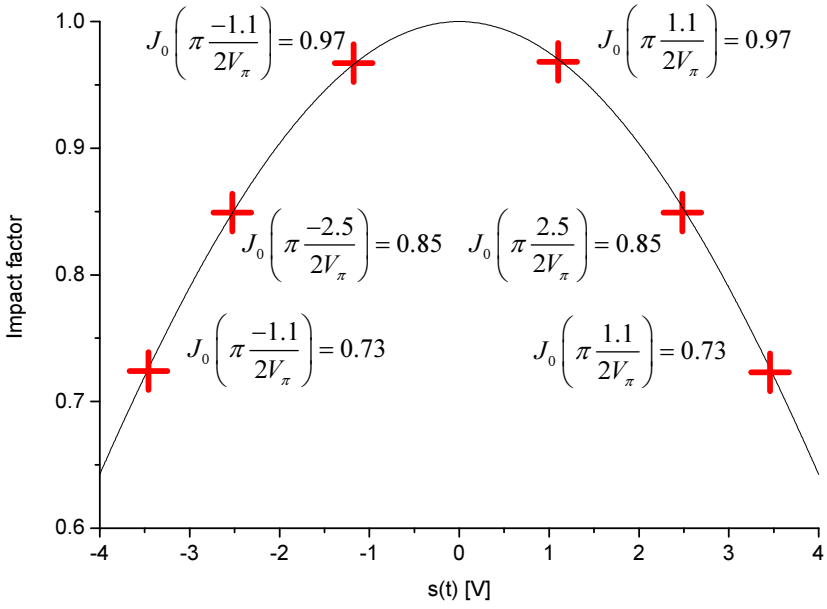

(a) impact factor of the 16-QAM IF modulation

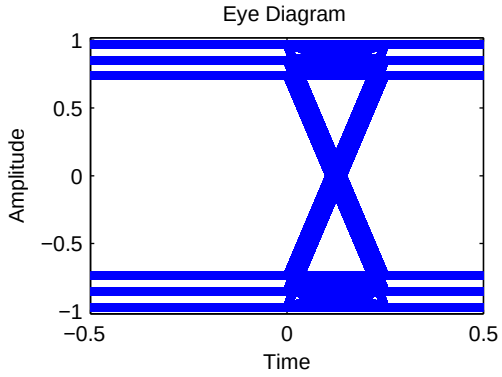

(b) Simulated baseband eyediagram with the impact of 18 dBm 16-QAM

Fig. 3.10. 18dBm 16-QAM IF impact to the baseband signal

3.3.3.2. Comparison of different multiband modulation techniques

From equation (3.9), we have mentioned that our proposed parallel phase modulation causes no impact from baseband modulation to the mmW signal. It would be a substantial advantage compared to other multiband modulation techniques, such as classical multiband modulation with pure intensity modulator (IM). Since multiband modulation technique is the key-technique in the converged RoF and WDM-PON system, it is necessary to compare these different multiband modulation techniques.

- **MZM as parallel phase modulators**

The architecture of the MZM, which is employed as two parallel phase modulators, is already shown in Fig. 3.7. The optical fields in optical waveguide 1 driven by IF signal and optical waveguide 2 driven by baseband signal can be expressed as

$$\begin{aligned} E_{wg1} &= \frac{E_2}{2\sqrt{I_L}} \exp\left(j\left[2\pi\left(f_{OP} + f_{LO1} \right)t + \pi \frac{V_{DC}}{2V_\pi} \right] \right) \exp\left(j\pi \frac{V_{IF}(t)}{2V_\pi} \right) \\ E_{wg2} &= \frac{E_2}{2\sqrt{I_L}} \exp\left(j\left[2\pi\left(f_{OP} + f_{LO1} \right)t - \pi \frac{V_{DC}}{2V_\pi} \right] \right) \exp\left(j\pi \frac{V_{BB}(t)}{2V_\pi} \right) \end{aligned} \tag{3.14}$$

Using the Jacobi-Anger identity as equation (3.7), E_{wg1} can be derived as:

$$\begin{aligned} E_{wg1} \approx{}& \frac{E_2}{2\sqrt{I_L}} \exp\left(j\left[2\pi\left(f_{OP} + f_{LO1} \right)t + \pi \frac{V_{DC}}{2V_\pi} \right] \right) J_0\left(\pi \frac{s(t)}{2V_\pi} \right) + \\ & \frac{E_2}{2\sqrt{I_L}} \exp\left(j\left[2\pi\left(f_{OP} + f_{LO1} + f_{IF} \right)t + \pi \frac{V_{DC}}{2V_\pi} + \frac{\pi}{2} \right] \right) J_1\left(\pi \frac{s(t)}{2V_\pi} \right) \exp\left(j\phi(t) \right) + \\ & \frac{E_2}{2\sqrt{I_L}} \exp\left(j\left[2\pi\left(f_{OP} + f_{LO1} - f_{IF} \right)t + \pi \frac{V_{DC}}{2V_\pi} + \frac{\pi}{2} \right] \right) J_1\left(\pi \frac{s(t)}{2V_\pi} \right) \exp\left(j\phi(t) \right) + \ldots \end{aligned} \tag{3.15}$$

The first term of (3.15) indicates that the impact of the phase modulation of an IF signal to the optical carrier is due to a non-linearity of the phase modulation. When the IF signal is small compared to V_π, the impact is negligible, since the zero order Bessel function of the first kind $J_0(x)$ is flat when x is small. When the IF signal is large enough, and the IF modulation is not constant amplitude modulation, the first term of (3.15) indicates that the carrier of the optical field in waveguide 1 is actually amplitude modulated. The spectrums of the optical fields in DEMUX channel #2, with the 3 main spectral components calculated in (3.15), and optical spectrums of

optical signal in channel #4 are shown in Fig. 3.11.

Fig. 3.11 shows that there is no impact from the baseband modulation to the mmW generation since the mmW signal is actually generated from a single beating between a pure CW optical spectral line in channel #4 and the first optical sideband of optical wave from MZM #2, which is generated by pure IF phase modulation and depends only on the IF signal. Moreover, there is no chromatic dispersion impact, due to the fact that the mmW is issued by a single beating.

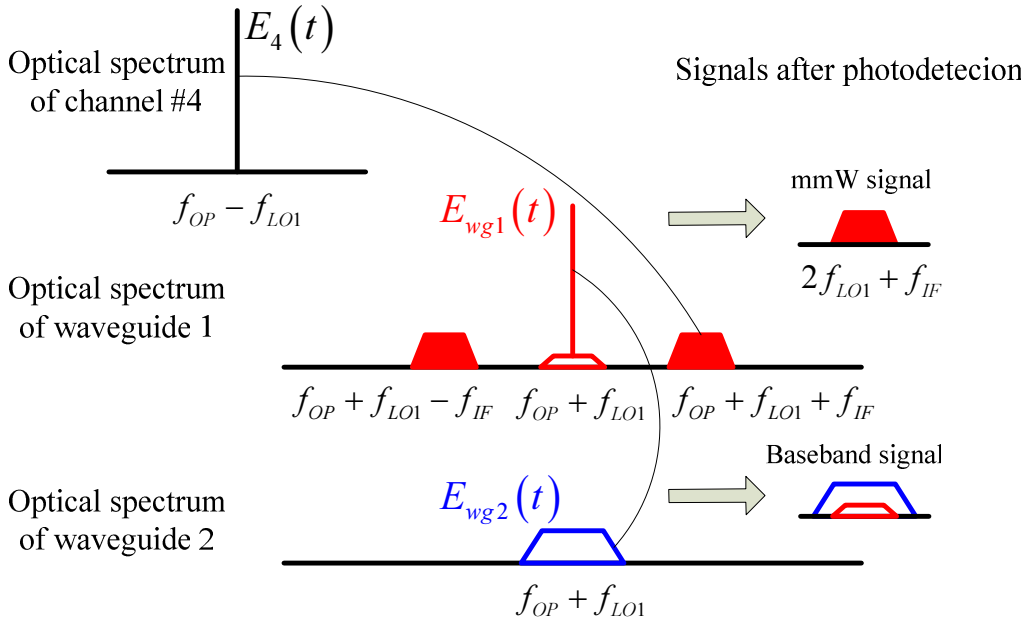

Fig. 3.11. Spectrums of optical fields by using multi-band modulation with MZM

Fig. 3.11 also shows that the baseband signal is generated by the phase to intensity conversion of the phase modulated optical wave in waveguide #2 with the optical carrier in waveguide #1. From (3.15), it can be said that the IF modulation in waveguide #1 influences the amplitude of the optical carrier in waveguide #1. Consequently the IF modulation brings impact to the baseband signal after the photodetection, which cannot be suppressed by using any optical filter, but can be minimized by limiting the IF signal power. This impact is small when the power of the IF signal is low. We also need to mention that only a DC is issued by the optical self-heterodyning of the two sidebands, since the optical sidebands in optical waveguide 1 are phase modulated. Because of this, it is not necessary to employ another optical filter to extract the optical carrier modulated by the baseband signal

from the output of MZM #2 for the baseband photodetection. These elements make it advantageous the use of MZM as parallel phase modulators instead of as an intensity modulator.

- **MZM as a single-arm modulator**

In [3], a multi-band modulation technique with a single MZM is proposed for the multi-band modulation in order to lessen the cost of the infrastructure. However, it does not give deeply investigation about the interference between two-band modulation.

Fig. 3.12 shows the MZM as a single-arm modulator for two-band modulation. The two-band signal, which contains baseband signal and IF signal, is applied to one electrode of the MZM.

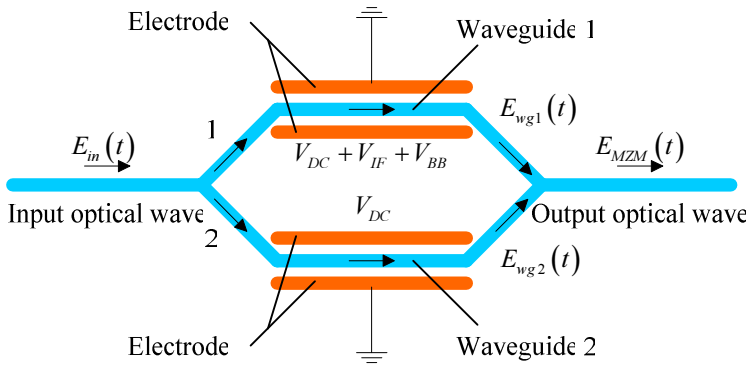

Fig. 3.12. Two-band modulation with MZM as a single-arm modulator

The optical field of the MZM is expressed as

$$E_{MZM\#2}=\frac{1}{2}\frac{1}{\sqrt{I_L}}E_2(t)\left[\exp\left(j\pi\frac{V_{DC}+V_{IF}(t)+V_{BB}(t)}{2V_\pi}\right)+\exp\left(-j\pi\frac{V_{DC}}{2V_\pi}\right)\right]$$

$$=\frac{E_2}{2\sqrt{I_L}}\left[\exp\left(j\left(2\pi(f_{OP}+f_{LO})t+\pi\frac{V_{DC}+V_{IF}(t)+V_{BB}(t)}{2V_\pi}\right)\right)+\exp\left(j\left(2\pi(f_{OP}+f_{LO})t-\pi\frac{V_{DC}}{2V_\pi}\right)\right)\right] \quad (3.16)$$

The photocurrent at the mmW receiver i_{PDmmW} is issued from the beating of output optical field of MZM #2 ($E_{MZM\#2}(t)$) and optical field of channel #4 ($E_4(t)$) and can be written as

$$
\begin{aligned}
i_{PD_{mmW}} &= k_1 \left| E_{MZM\#2}(t) + E_4(t) \right|^2 \\
&= k_1 E_4^2 + \frac{k_1 E_2^2}{2I_L} + \frac{k_1 E_2^2}{2I_L} \cos\left(\pi \frac{2V_{DC} + V_{IF}(t) - V_{BB}(t)}{2V_\pi} \right) + \\
&\frac{k_1 E_2 E_4}{\sqrt{I_L}} \cos\left(4\pi f_{LO} t - \pi \frac{V_{DC}}{2V_\pi} \right) + \frac{k_1 E_2 E_4}{\sqrt{I_L}} \cos\left(4\pi f_{LO} t + \pi \frac{V_{DC} + V_{IF}(t) - V_{BB}(t)}{2V_\pi} \right)
\end{aligned} \tag{3.17}
$$

The last term of (3.17) contains the mmW signal at frequency $2f_{LO} + f_{IF}$, which can be derived as

$$
\begin{aligned}
&\frac{E_2 E_4}{\sqrt{I_L}} \cos\left(4\pi f_{LO} t + \pi \frac{V_{DC} + V_{IF}(t) - V_{BB}(t)}{2V_\pi} \right) \\
&= \frac{E_2 E_4}{\sqrt{I_L}} \left[\cos\left(4\pi f_{LO} t + \pi \frac{V_{DC} - V_{BB}(t)}{2V_\pi} \right) \cos\left(\pi \frac{V_{IF}(t)}{2V_\pi} \right) - \right. \\
&\left. \sin\left(4\pi f_{LO} t + \pi \frac{V_{DC} - V_{BB}(t)}{2V_\pi} \right) \sin\left(\pi \frac{V_{IF}(t)}{2V_\pi} \right) \right]
\end{aligned} \tag{3.18}
$$

By using the Jacobi-Anger expansion in (3.7), the optical mmW is expressed as

$$
i_{mmW} = k_1 \frac{E_2 E_4}{\sqrt{I_L}} J_1\left(\pi \frac{s(t)}{2V_\pi} \right) \sin\left(2\pi (2f_{LO} + f_{IF}) t + \phi(t) + \pi \frac{V_{DC} - V_{BB}(t)}{2V_\pi} \right) \tag{3.19}
$$

Equation (3.19) indicates that the baseband signal induces phase modulation on the mmW when multiband modulation technique is used with a single-arm MZM. The impact of the baseband signal to the mmW is significant due to the linear phase impact, contrary to our proposed parallel phase modulation technique, for which there is no impact of baseband on the photodetected mmW.

The photocurrent at the baseband receiver is generated from the self-heterodyning of the output optical field of the MZM #2 as:

$$
\begin{aligned}
&i_{PD_{BB}} = k_2 \left| E_{MZM\#2}(t) \right|^2 \\
&= \frac{k_2 E_2}{2\sqrt{I_L}} \left[\exp\left(j\left(2\pi \left(f_{OP} + f_{LO} \right) t + \pi \frac{V_{DC} + V_{IF}(t) + V_{BB}(t)}{2V_\pi} \right) \right) + \exp\left(j\left(2\pi \left(f_{OP} + f_{LO} \right) t - \pi \frac{V_{DC}}{2V_\pi} \right) \right) \right] \bullet \\
&\left\{ \frac{E_2}{2\sqrt{I_L}} \left[\exp\left(j\left(2\pi \left(f_{OP} + f_{LO} \right) t + \pi \frac{V_{DC} + V_{IF}(t) + V_{BB}(t)}{2V_\pi} \right) \right) + \exp\left(j\left(2\pi \left(f_{OP} + f_{LO} \right) t - \pi \frac{V_{DC}}{2V_\pi} \right) \right) \right] \right\}^* \\
&= \frac{k_2 E_2^2}{2I_L} + \frac{k_2 E_2^2}{4I_L} \exp\left(j\pi \frac{2V_{DC} + V_{IF}(t) + V_{BB}(t)}{2V_\pi} \right) + \frac{k_2 E_2^2}{4I_L} \exp\left(-j\pi \frac{2V_{DC} + V_{IF}(t) + V_{BB}(t)}{2V_\pi} \right) \\
&= \frac{k_2 E_2^2}{2I_L} + \frac{k_2 E_2^2}{2I_L} \cos\left(\pi \frac{2V_{DC} + V_{IF}(t) + V_{BB}(t)}{2V_\pi} \right)
\end{aligned}
\tag{3.20}
$$

Comparing (3.20) with (3.10), the photocurrent at the baseband receiver with a single-arm MZM is the same as the photocurrent with our parallel phase modulation technique. The impact factor of the IF modulation to the baseband signal is the same one as defined in (3.13).

It can be concluded that the multiband modulation technique with a single-arm MZM will bring significant phase impact from the baseband signal to the mmW compared to the parallel phase modulation. The impact of the RF modulation to the baseband is due to the non-linearity of the MZM as for the parallel phase modulation technique with the same impact factor.

- **MZM as a push-pull MZM**

In [4, 5], a electro absorption modulator (EAM) is employed for the multi-band modulation. However, this technique requires proper bias voltage of the EAM in order to avoid the signal distortion due to the non-linearity of the EAM. A MZM working as push-pull function is another optical intensity modulator with the similar characterization as EAM. Here we would like to use push-pull MZM model to present the multi-band modulation technique with a common optical intensity modulator.

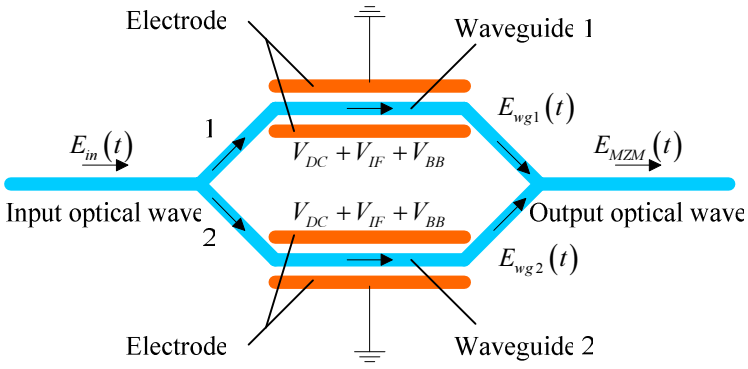

Fig. 3.13. Two-band modulation with MZM as a single-arm modulator

Fig. 3.13 shows the MZM as an intensity modulator for two-band modulation. The two-band signal, which contains baseband signal and IF signal, is applied to the two electrodes of the push-pull MZM. The optical field of the MZM is expressed as

$$E_{MZM\#2}=\frac{1}{2}\frac{1}{\sqrt{I_L}}E_2(t)\left[\exp\left(j\pi\frac{V_{DC}+V_{IF}(t)+V_{BB}(t)}{2V_\pi}\right)+\exp\left(-j\pi\frac{V_{DC}+V_{IF}(t)+V_{BB}(t)}{2V_\pi}\right)\right]$$
$$=\frac{E_2}{\sqrt{I_L}}\exp\left(j2\pi\left(f_{OP}+f_{LO}\right)t\right)\cos\left(\pi\frac{V_{DC}+V_{IF}(t)+V_{BB}(t)}{2V_\pi}\right)$$

(3.21)

The photocurrent of the baseband receiver is expressed as:

$$i_{PD_{BB}}=k_2\left|E_{MZM\#2}(t)\right|^2$$
$$=\frac{k_2E_2}{I_L}\cos^2\left(\pi\frac{V_{DC}+V_{IF}(t)+V_{BB}(t)}{2V_\pi}\right)$$
$$=\frac{k_2E_2}{2I_L}\left[1+\cos\left(\pi\frac{V_{DC}+V_{IF}(t)+V_{BB}(t)}{V_\pi}\right)\right]$$
$$=\frac{k_2E_2}{2I_L}+\frac{k_2E_2}{2I_L}\left[\cos\left(\pi\frac{V_{DC}+V_{BB}(t)}{V_\pi}\right)\cos\left(\pi\frac{V_{IF}(t)}{V_\pi}\right)-\sin\left(\pi\frac{V_{DC}+V_{BB}(t)}{V_\pi}\right)\sin\left(\pi\frac{V_{IF}(t)}{V_\pi}\right)\right]$$

(3.22)

Using the Jacobi-Anger expansion in (3.7), equation (3.22) can be derived as

$$i_{PD_{BB}}=\frac{k_2E_2}{2I_L}+\frac{k_2E_2}{2I_L}\left\{2\sin\left(\pi\frac{V_{DC}+V_{BB}(t)}{V_\pi}\right)\sum_{n=1}^{\infty}(-1)^nJ_{2n-1}\left(\pi\frac{s(t)}{2V_\pi}\right)\cos\left[(2n-1)\left(2\pi f_{IF}t+\phi(t)\right)\right]+\right.$$
$$\left.\cos\left(\pi\frac{V_{DC}+V_{BB}(t)}{V_\pi}\right)\left[J_0\left(\pi\frac{s(t)}{V_\pi}\right)+2\sum_{n=1}^{\infty}(-1)^nJ_{2n}\left(\pi\frac{s(t)}{V_\pi}\right)\cos\left(2n\left(2\pi f_{IF}+\phi_{IF}(t)\right)\right)\right]\right\}$$

(3.23)

It can be seen that the second term in the bracket contains the baseband component, which can be extracts by a low-pass filter. The baseband signal is expressed as:

$$i_{BB} = \frac{k_2 E_2}{2I_L}\cos\left(\pi\frac{V_{DC}+V_{BB}(t)}{V_\pi}\right)J_0\left(\pi\frac{s(t)}{V_\pi}\right) \tag{3.24}$$

The mmW is issued from the beating between the optical field of the MZM #2 and the CW optical tone in channel #4. The photocurrent of the mmW receiver is expressed as:

$$\begin{aligned}
i_{PD_{mmW}} &= \left|E_{MZM\#2}(t)+E_4(t)\right|^2 \\
&= \left[E_{MZM\#2}(t)+E_4(t)\right]\left[E_{MZM\#2}(t)+E_4(t)\right]^* \\
&= \left|E_{MZM\#2}(t)\right|^2+\left|E_4(t)\right|^2+E_{MZM\#2}(t)E_4^*(t)+E_{MZM\#2}^*(t)E_4(t) \\
&= E_4^2+\frac{E_2^2}{I_L}\cos^2\left(\pi\frac{V_{DC}+V_{IF}(t)+V_{BB}(t)}{2V_\pi}\right)+\frac{2E_2E_4}{\sqrt{I_L}}\cos\left(\pi\frac{V_{DC}+V_{IF}(t)+V_{BB}(t)}{2V_\pi}\right)\cos\left(4\pi f_{LO}t\right)
\end{aligned} \tag{3.25}$$

The last term in (3.25) contains the mmW signal at the frequency $2f_{LO}+f_{IF}$. By using Jacobi-Anger expansion in (3.7), it can be derived as

$$\begin{aligned}
&\frac{2E_2E_4}{\sqrt{I_L}}\cos\left(\pi\frac{V_{DC}+V_{IF}(t)+V_{BB}(t)}{2V_\pi}\right)\cos\left(4\pi f_{LO}t\right) \\
&= \frac{2E_2E_4}{\sqrt{I_L}}\cos\left(4\pi f_{LO}t\right)\left[\cos\left(\pi\frac{V_{DC}+V_{BB}(t)}{2V_\pi}\right)\cos\left(\pi\frac{V_{IF}(t)}{2V_\pi}\right)+\sin\left(\pi\frac{V_{DC}+V_{BB}(t)}{2V_\pi}\right)\sin\left(\pi\frac{V_{IF}(t)}{2V_\pi}\right)\right] \\
&= \frac{2E_2E_4}{\sqrt{I_L}}\cos\left(4\pi f_{LO}t\right)\left\{-2\sin\left(\pi\frac{V_{DC}+V_{BB}(t)}{2V_\pi}\right)\sum_{n=1}^{\infty}(-1)^n J_{2n-1}\left(\pi\frac{s(t)}{2V_\pi}\right)\cos\left[(2n-1)\left(2\pi f_{IF}t+\phi(t)\right)\right]+\right. \\
&\left.\cos\left(\pi\frac{V_{DC}+V_{BB}(t)}{2V_\pi}\right)\left[J_0\left(\pi\frac{s(t)}{V_\pi}\right)+2\sum_{n=1}^{\infty}(-1)^n J_{2n}\left(\pi\frac{s(t)}{V_\pi}\right)\cos\left(2n\left(2\pi f_{IF}+\phi_{IF}(t)\right)\right)\right]\right\}
\end{aligned} \tag{3.26}$$

The first term in bracket in (3.26) contains the mmW signal at $2f_{LO}+f_{IF}$, which can be extracted by using wave-guide filter. Finally the mmW signal at $2f_{LO}+f_{IF}$ can be derived as:

$$i_{mmW} = \frac{2E_2E_4}{\sqrt{I_L}}\sin\left(\pi\frac{V_{DC}+V_{BB}(t)}{2V_\pi}\right)J_1\left(\pi\frac{s(t)}{2V_\pi}\right)\cos\left[2\pi\left(2f_{LO}+f_{IF}\right)t+\phi(t)\right] \tag{3.27}$$

From equation (3.27), it is obvious that the DC voltage of the MZM #2 should be set to $V_{DC} = V_{\pi}$ in order to minimize the impact from the baseband modulation to the mmW signal. However, from equation (3.24), it can be seen that the MZM #2 should be biased at $V_{DC} = 0.5V_{\pi}$ to have the maximum baseband output, which contradicts the requirement for the mmW generation. In practice, it is necessary to probe the bias voltage of the MZM to optimize both the baseband signal transmission and mmW generation. Moreover, we need to mention that the IF modulation brings impact to the baseband signal with the impact factor as

$$F_{i\_push-pull} = J_0\left(\pi \frac{s(t)}{V_{\pi}}\right) \tag{3.28}$$

Comparing (3.28) and (3.13), it is obvious that the IF modulation impact to the baseband signal by using the MZM as push-pull MZM is larger than the one with the MZM as parallel phase modulators.

Based on the comparison of different modulation technique, it can be concluded that the parallel modulation technique with a single MZM provides significant advantage.

3.3.3 Experimental demonstration of the simultaneous transmission of broadband mmW and multi-gigabit baseband signal

Our novel parallel phase modulation technique presented in section 3.3.2 is experimentally demonstrated in the following section. Experimental set-up shown in Fig. 3.6 is realized, MZM #2 is used as a parallel phase modulator.

3.3.3.1 Broadband mmW measurements

The electrical spectrum and constellation diagram for 1588 Mbps BPSK mmW with and without baseband modulation after electrical down-conversion to 2 GHz band are shown in Fig. 3.14 (a) and (b) respectively.

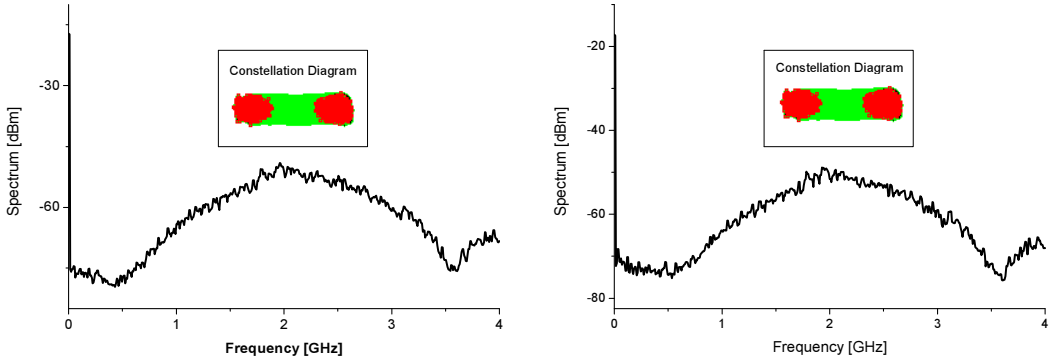

(a) Single RF modulation (b) Two band modulation

Fig. 3.14. Spectrums of optical broadband optical mmW down-converted to 2 GHz band with and without the baseband modulation. Inset: constellation diagrams.

EVM of the broadband mmW with and without baseband modulation, which are compared with the EVM requirements according to ECMA 387 standard, are reported in Tab. 3.3.

Tab. 3.3 Power and EVM measurements after electrical down-conversion compared with the requirements of ECMA 387 standard

(i) ECMA387 requirements for transmitter and receiver			
Data Rate (Mbps)	397	794	1588
Maximum emitted power (dBm)	10	10	10
Maximum allowed EVM (%)	33.4	23.7	11.2
(ii) Broadband mmW with baseband signal			
Data Rate (Mbps)	397	794	1588
Power after down-conversion (dBm)	-14.2	-14.8	-15.9
Received Power at 58.32 GHz (dBm)	-7.2	-7.8	-8.9
EVM (%)	7.0	10.1	13.0
(iii) Broadband mmW without baseband signal			
Data Rate (Mbps)	397	794	1588
Power after down-conversion (dBm)	-14.1	-14.8	-16.4
Received Power at 58.32 GHz (dBm)	-7.1	-7.8	-9.4
EVM (%)	7.1	10.1	13.0

EVM values are in the limit of the ECMA 387 standard to insure error free transmission except for the 1588 Mbps data rate. EVM measurements for the optical generated broadband mmW at 397 Mbps and 794 Mbps meet the requirements of the ECMA 387 standard with a large margin (Tab. 3.3 (i) and (ii)). Comparing Tab. 3.3 (ii) and (iii), it is obvious that, for parallel phase modulation technique, there is no impact from the baseband modulation to the mmW signal, which agrees with the theoretical

conclusions drawn in section 3.3.2.

3.3.3.2 Baseband signal measurements

Fig. 3.15 (a)~(d) show the eye diagrams of 2.5 Gbps baseband signal without IF signal modulation or with 18 dBm, 16 dBm, 13 dBm 1.588 Gbps IF signal modulation respectively.

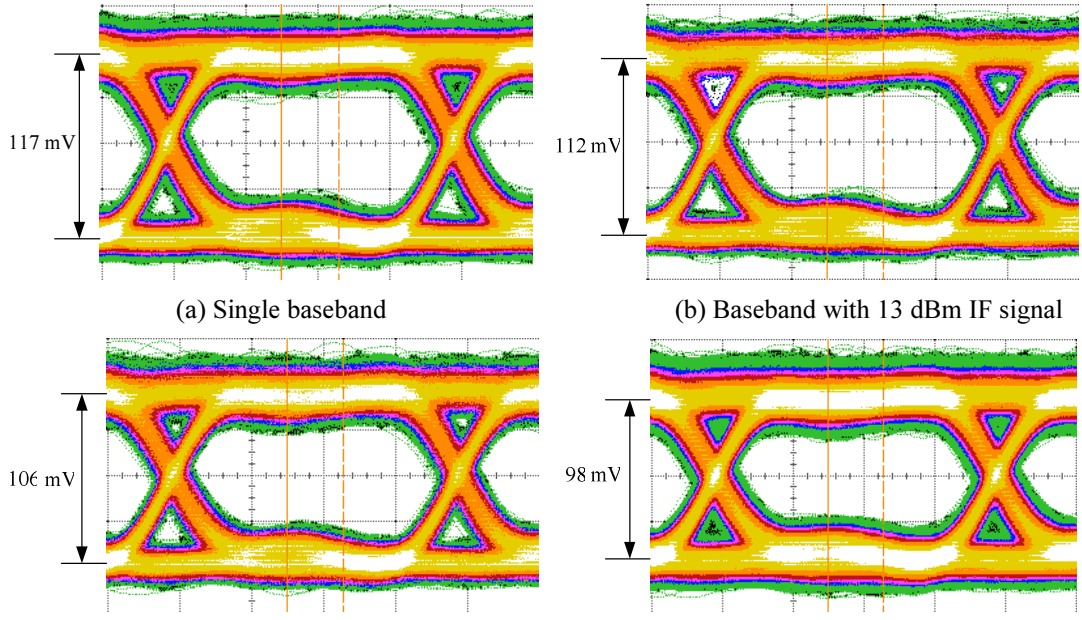

(a) Single baseband (b) Baseband with 13 dBm IF signal

(c) Baseband with 16 dBm IF signal (d) Baseband with 18 dBm IF signal

Fig. 3.15. Eye diagrams of the baseband signal with single band and two-band modulation configurations

The amplitude of the IF signal is a constant, that the impact factor shown in (3.13) is a constant. As it is predicted by the theoretical analysis, the eye height of the baseband signal decreases when IF power increases, owing to the impact of the RF modulation induced by MZM #2 (Fig. 3.6), which is compliant with the theoretical analysis carried out in section 3.3.2.

Tab. 3.4 Measurement results of the IF modulation impact to the baseband signal compared with the theoretical model

(i) Baseband signal measurement				
IF signal power (dBm)	IF off	13	16	18
Q-factor	7.8	7.7	7.4	7
Eyeheight (mV)	117	112	106	98
Amplitude ratio(%)	100	95.7	90.6	83.8
(ii) Estimation of the baseband amplitude degradation due to the IF modulation				
IF signal power (dBm)	IF off	13	16	18
Amplitude ratio $J_0(\pi s(t)/2V_\pi)$ (%)	100	95.1	90.4	85

Tab. 3.4 shows the eyeheights and Q-factors for the baseband signals with

different IF signal power. The ratio of eyeheights with and without IF modulation is also reported and compared with theoretical value calculated using equation (3.12). In equation (3.12), the impact factor $J_0(\pi s(t)/2V_\pi)$ term indicates the loss of the amplitude due to the IF modulation, where V_π is 5V and s(t) is calculated from the IF output power. Comparing the amplitude ratios shown in Tab. 3.4 (i) and (ii), it can be seen that the measured baseband amplitude degradation agrees with the predicted value by using equation (3.12). According to equation (3.11), the baseband signal loses 15% of amplitude due to the impact of 18 dBm IF BPSK modulation, which amounts to 1.4 dB loss in electrical power.

Fig. 3.16 shows the measured BERs as a function of the received optical power for the single baseband modulation and two-band modulation. From Fig. 3.17, the difference between the received optical power in the case of signal baseband modulation and two-band modulation, for the same BER value, is around 0.7 dB, which amounts to 1.4 dB electrical power as well. This agrees with the theoretical model. Despite the impact of RF modulation, the baseband signal with low BER ($<<10^{-9}$) has been transmitted over 25 km long SMF by our system.

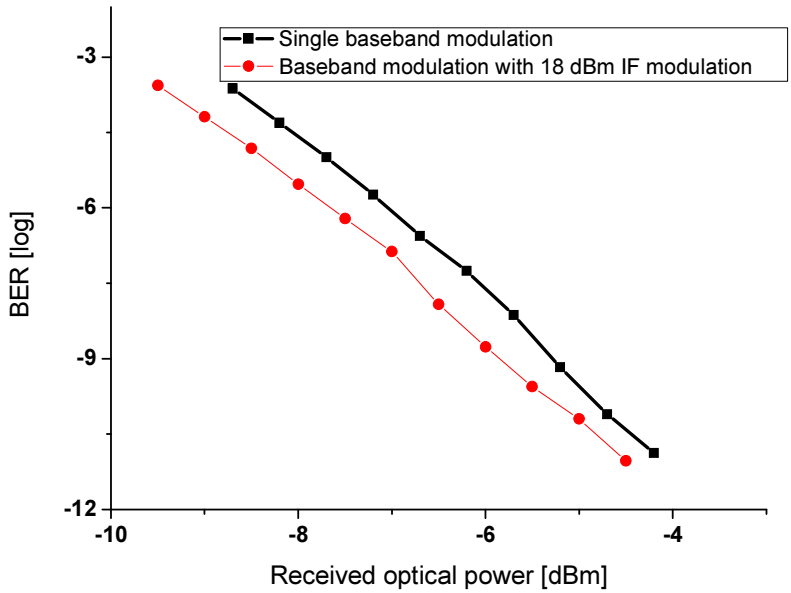

Fig. 3.16. BER measurement as a function of received optical power for single band and two-band modulation configurations.

3.3.4 Investigation of IF Modulation Impact to Baseband

From the theoretical analysis and gigabit wireline and wireless transmission experiment with parallel phase modulation technique developed in section 3.3.2, it can be concluded that the baseband modulation will not bring any impact to the RF signal generation, but IF modulation will degrade the baseband signal. We have also shown that the impact of the IF modulation depends on the amplitude of the IF signal by following the impact factor $J_0(\pi s(t)/2V_\pi)$ defined in equation (3.13). When the amplitude of the BPSK IF signal is roughly a constant, the impact of the IF modulation to the baseband signal is limited even if a high power IF signal is applied to the MZM #2 (Fig. 2). However, the wireless transmission should support different modulation schemes, such as 16-QAM and OFDM. It would be expected that these non-constant amplitude IF modulations would bring significant impact to the baseband signal. In this section, the impact of the different IF modulation schemes to the baseband signal is deeply investigated.

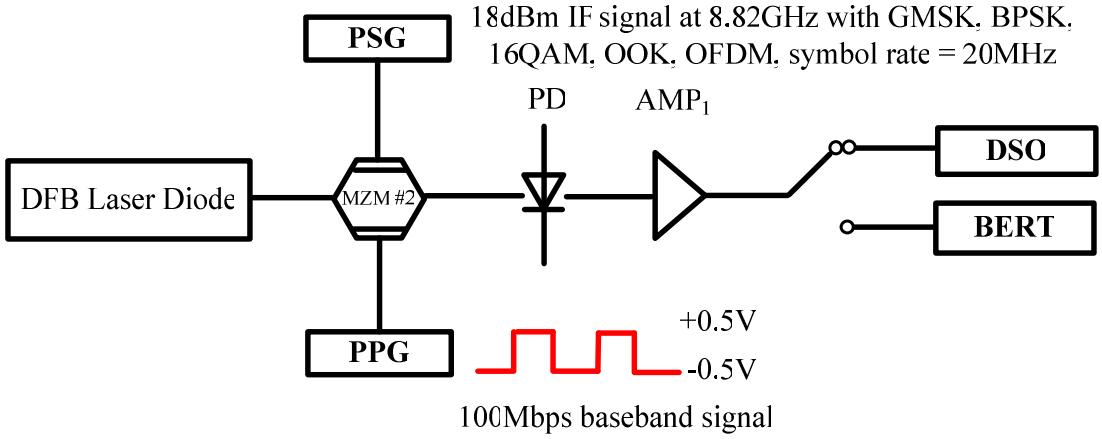

Fig. 3.17. Simple experimental schematic of baseband investigation

Fig. 3.17 shows a simple experimental schematic focused on the investigation of the IF modulation impact to the baseband signal, in which the EDFAs have been discarded to decrease the noise contribution from the amplified spontaneous emission (ASE) emitted by the EDFA. The MZM, which is biased in the linear regime, is employed as two parallel phase modulators for both IF modulation driven by PSG and baseband modulation from PPG. The PD with the bandwidth of 10 GHz is used for

baseband photodetection. Due to the limited bandwidth of our vector signal generator (PSG) a 18 dBm IF signal at 8.82 GHz with only 20 MHz bandwidth is generated and applied to the MZM #2. The Gaussian filtered minimum shift keying (GMSK), BPSK, 16-QAM, on-off-keying (OOK) and OFDM modulations are implemented by the PSG respectively. In order to be scaled in the same range of bandwidth as for the previous experimental analysis with 1588 Mbps BPSK and 2.5 Gbps baseband, a 100 Mbps baseband signal is applied to the MZM #2, so the ratio of symbol duration for baseband and IF modulation is kept constant.

Fig. 3.18 shows the eye diagrams of the baseband signals for the different IF modulation schemes when both signals are applied to the MZM used as a two parallel phase modulators. As expected from theoretical analysis, Fig. 3.18 shows that the non-constant envelop IF modulation will bring bigger impact to the baseband signal compared to the constant envelop IF modulation as GMSK (Fig. 3.18 (b)).

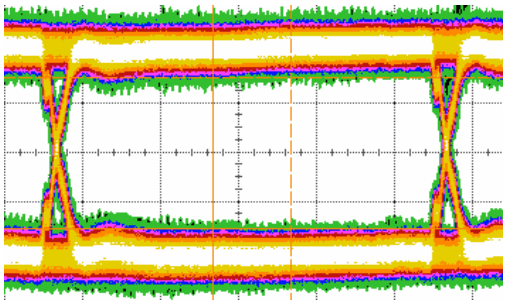

(a) Single baseband

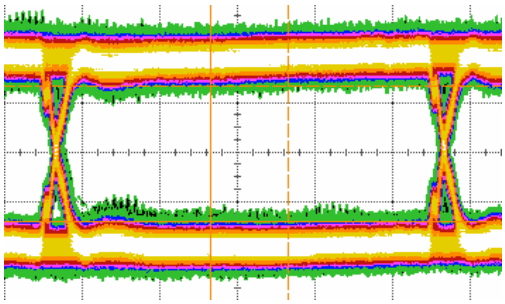

(b) Baseband with GMSK IF signal

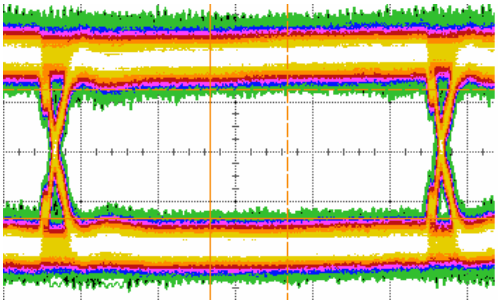

(c) Baseband with BPSK IF signal

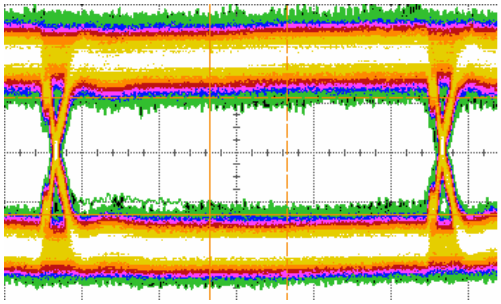

(d) Baseband with 16-QAM IF signal

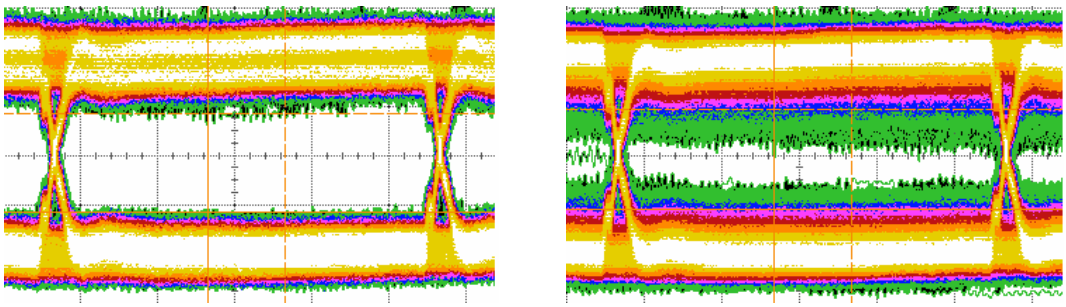

(e) Baseband with OOK IF signal (f) Baseband with OFDM IF signal

Fig. 3.18. Eye diagrams of the baseband signals with or without the impact of different IF modulation schemes

The *Q*-factor is defined in (3.1). *Q*-factor can be linked to the BER by using the following formula.

$$BER = \frac{1}{2} erfc\left(\frac{Q}{\sqrt{2}}\right) \tag{3.29}$$

where *erfc* (•) is the complementary error function.

Assuming that the *Q*-factor of the single baseband modulation system is Q_0, the *Q*-factor which takes into account the impact factor induced by the IF modulation (3.13) is given by

$$Q = Q_0 F_i = Q_0 J_0\left(\pi \frac{s(t)}{2V_\pi}\right) \tag{3.30}$$

Equation (3.30) indicates that the *Q*-factor of the baseband signal is no longer constant when the IF modulation is not constant envelop modulation. By using (3.29) and (3.30), the BER of the baseband signal with the IF modulation impact is derived as

$$BER = \int_0^{+\infty} \frac{1}{2} erfc\left(\frac{Q_0 J_0\left(\pi \frac{s}{2V_\pi}\right)}{\sqrt{2}}\right) P(s)\, ds \tag{3.31}$$

where *P (s)* is the probability density function of the IF amplitude *s(t)*. Equation (3.31) can be derived as

$$BER = \int_0^{s_{av}} \frac{1}{2} erfc\left(\frac{Q_0 J_0\left(\pi \frac{s}{2V_\pi} \right)}{\sqrt{2}} \right) P(s)\,ds + \int_{s_{av}}^{+\infty} \frac{1}{2} erfc\left(\frac{Q_0 J_0\left(\pi \frac{s}{2V_\pi} \right)}{\sqrt{2}} \right) P(s)\,ds \quad (3.32)$$

where s_{av} is the average amplitude of the IF signal. For a high Q baseband transmission, the first term of (3.32) is negligible. As a result, the BER as a function of $P(s)$ is derived as

$$BER \approx \int_{s_{av}}^{+\infty} \frac{1}{2} erfc\left(\frac{Q_0 J_0\left(\pi \frac{s}{2V_\pi} \right)}{\sqrt{2}} \right) P(s)\,ds \quad (3.33)$$

The $P(s)$ with $s(t) > s_{av}$ can be obtained from the investigation of the complementary cumulative distribution function (CCDF) of the PAPR by using the following equation.

$$P(s) = -\frac{d}{ds} CCDF(PAPR) \quad (3.34)$$

Fig. 3.19 shows the CCDFs of the PAPR for IF signals with different modulation formats, which are implemented in the experiment.

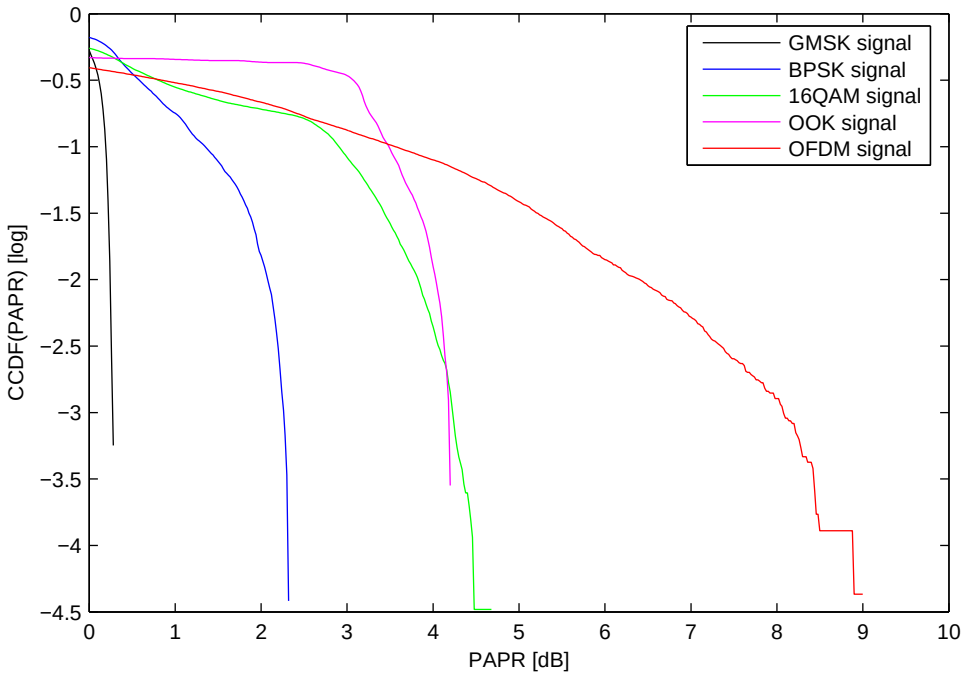

Fig. 3.19. CCDFs of PAPR for different modulation formats

Tab. 3.5 reports the estimated BER with the impact of 18 dBm IF modulation for

different modulation formats using equation (3.33) and the CCDFs of PAPR for different modulation formats, which are shown in Fig. 3.19, compared with the BER testing results. Note that the Q_0 is 11 from the eye diagram measurement of the baseband signal transmission. Since the BERs of the baseband signal with the common modulation formats such as BPSK, 16QAM, OOK are too small ($<10^{-12}$), only the BER for baseband signal with OFDM impact can be precisely measured.

Tab. 3.5. Theoretical and experimental BERs of the baseband signals with and without different IF modulation formats (Q_0 =11)

IF modulation scheme	IF off	GMSK	BPSK	16-QAM	OOK	OFDM
Simulated BER (log)	-27.7	-18.4	-16.0	-11.8	-11.5	-2.4
Measured BER (log)	X	X	X	X	X	-4.7

To measure the BERs of the baseband signal with the impact OOK and 16QAM IF modulation, it is necessary to decrease the *Q*-factor (Q_0) of the single baseband transmission. An optical attenuator is employed before the photodetection to decrease the signal to noise ratio (SNR). In this case, the *Q*-factor (Q_0) of the single baseband transmission is 10. Tab. IV reports the estimated BERs with the impact of 18 dBm IF modulation for different modulation formats using equation (3.33) compared with the BER testing result in the case of Q_0 =10.

Tab. 3.6.Theoretical and experimental BERs of the baseband signals with and without different IF modulation formats (Q_0 =10)

IF modulation scheme	16-QAM	OOK	OFDM
BER from simulations (log)	-9.9	-9.5	-2.3
BER of experiment (log)	-9.7	-9.4	-3.1

From Tab. 3.6, the agreement of the theoretical estimation of the BERs with the measurement results validates the theoretical model to estimate the IF modulation impact to the baseband BER. Nevertheless, the estimated BER with the impact of the OFDM is higher than the experimental result. It is due to the fact that the peak power of the OFDM is much higher than the maximum input power of the MZM to induce saturation of the phase modulation driven by IF signal. As consequence, this non-linearity of the phase modulation constrains the impact of the IF modulation.

Synthesizing Tab. 3.5 and Tab. 3.6, both the experimental results and the theoretical estimations show that the impact of the higher modulation format as 16

QAM can be limited in the high Q baseband transmission system. However, the impact of the OFDM signal is significant due to the high PAPR of this modulation format. It is necessary to investigate on the PAPR of the IF modulation formats before implementing the multiband modulation with single MZM. Optimal average IF modulation power to stay in the limit of BER for error free transmission can be derived from equations (3.33) and (3.34).

3.4 Conclusion

A WDM-RoF system for wireline and wireless transmissions compatible with both broadband BPSK mmW for ECMA 387 standard and 1 Gbps baseband signal for FTTH application has been demonstrated in this section. The digital signal modulations for mmW and baseband signal are implemented by using a single dual-electrode MZM used as a dual parallel phase modulator. This technique is compatible with WDM-RoF scheme to feed multiple BSs. Despite the low output power of the broadband mmW, 1588 Mbps BPSK signal at 60GHz band with the EVM as low as 13% has been generated by photonic up-conversion without any interference from the baseband signal modulation and any impact of chromatic dispersion after 25 km long fiber transmission. 2.5 Gbps baseband signal with the BER lower than 10^{-11} has been transmitted simultaneously. Furthermore, the interference from RF signal modulation to the baseband signal has been quantified by theoretical approach and experiment. It is theoretically proved that the parallel phase modulation with a single MZM for multiband modulation brings significant advantage compared with other multiband modulation techniques. It has been shown that for common I/Q RF modulation, the degradation of the baseband signal induced by the RF modulation is limited in high-Q optical transmission system, considering a high MZM input RF modulation power of 18 dBm. However, the impact of the RF signal modulation with high PAPR, such as OFDM signal, may induce significant impact to the baseband signal transmission if operating conditions are not properly defined. In that purpose, we have defined rules to define optimum RF modulation power to insure

the error free baseband transmission, based on the theoretical model of multi-band modulation technique.

References of chapter 3

[1] ECMA387. http://www.ecma-international.org/publications/standards/Ecma-387.htm.

[2] P. X. a. A. V. Su-Khiong Yong, "60 GHz Technology for Gbps WLAN and WPAN: From Theory to Practice," *John Wiley & Sons, Ltd,* 2011.

[3] Z. Liang*, et al.*, "A 60-GHz RoF system in WDM-PON with reduced number of modulators and low-cost electronics," in *Photonics Global Conference (PGC), 2010*, 2010, pp. 1-3.

[4] T. Kuri*, et al.*, "Radio over fiber: DWDM-based analog/digital access networking and its enabling technologies," in *Radio and Wireless Symposium, 2008 IEEE*, 2008, pp. 137-140.

[5] J. J. Vegas Olmos*, et al.*, "Reconfigurable Radio-Over-Fiber Networks: Multiple-Access Functionality Directly Over the Optical Layer," *Microwave Theory and Techniques, IEEE Transactions on,* vol. 58, pp. 3001-3010, 2010.

Chapter 4

Bidirectional mmW RoF system using photonic mixing technique

4.1 Introduction

In chapter 2, RoF system which centralizes optical mmW frequency generation for the down-link has been experimentally demonstrated. Furthermore, in chapter 3, convergence of RoF and WDM-PON has been proved based on the investigation of dual baseband/mmW radio modulations technique for simultaneous transmission of 60 GHz broadband signal and multi-gigabit per second baseband signal.

However the centralization of signal processing, such as frequency down-conversion, is not possible for the up-link scheme, and the use of one mmW bandwidth electrical to optical (E/O) transceiver per BS is also too expensive. Therefore, uplink data signals are usually frequency down-converted before optical transmission to lower the cost of the infrastructure.

In this chapter, a novel bidirectional mmW RoF architecture is demonstrated based on the application of a commercial off the shelf (COTS) p-i-n photodiode (PD). This PD is driven in non-linear regime to perform both photodetection for the mmW RoF down-link and frequency down-conversion for the mmW RoF up-link, without the need of changing PD bias voltage. In the up-link scheme, the so-called PD electrical output is used as an input for the mmW radio signal to realize optoelectronic mixing with remotely delivered LO from the down-link. The down-link scheme uses typical optical heterodyning scheme for mmW generation [1] and the impact of the non-linear PD on down-link performances is investigated in this chapter. A deep research investigation on optolectronic mixing with non-linear p-i-n photodiodes has been carried out in the frame of Flora PARESYS PhD at IMEP-LAHC [2]. The aim of the chapter is to prove the mmW RoF bidirectional system concept, integrating our optical heterodyning

down-link with up-link based on optoelectronic mixing. Mmw RoF bidirectional system is demonstrated using the modulation format and data rates which are compliant with 60 GHz ECMA 387 standard [3].

The organization of the chapter is as follows : section 4.2 introduces the concept of photonic mixing, which is the key-technique for the frequency down-conversion at the BS for the up-link transmission. The general architecture of the proposed bidirectional mmW RoF system is shown in section 4.3. In section 4.4, experimental investigations on the up-link transmission are presented, leading to optimized PD biasing conditions. The influence of the non-linear PD on the optical heterodyning down-link performances are finally inquired in section 4.5.

4.2 Design of the bidirectional RoF system

4.2.1 Concept of the photonic mixing technique for frequency down-conversion

Fig. 4.1 shows the original concept of optoelectronic mixing investigated in the frame of Flora PARESYS PhD. The optical wave, which is intensity modulated with an electrical signal at f_1 either by direct modulation or by external modulation, is transmitted to the PD for the photodetection. The PD is biased by a DC voltage of V_{PD}, and a CW signal from LO_2 is applied to the PD electrical port (usually used as an output port, but also used as an input here). As a result, the real biased voltage on the PD is modulated, causing fluctuations of the photodiode responsivity. When the PD is biased with direct voltage, it acts as a non-linear device, and PD responsivity is a non-linear function of V_{PD}. If a signal is photodetected at f_1, the non-linear fluctuation of the PD responsivity will cause the generation of intermodulation products at mf_1+nf_2 $m,n \in Z$ [2].

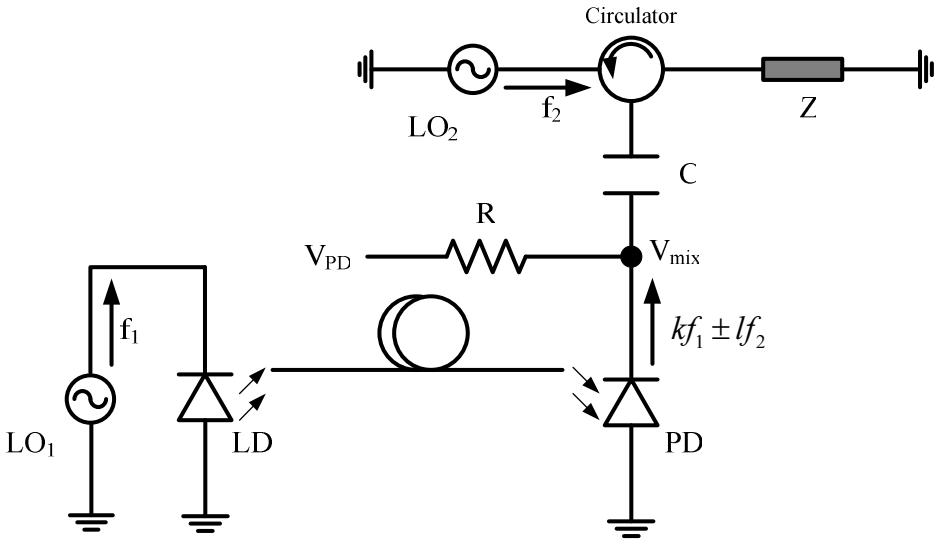

Fig. 4.1. Concept of the photonic mixing

Fig. 4.2 (a) shows the output power of the 60 GHz signal as a function of the bias voltage of the PD, which is normalized to the output power with -2.8 V DC bias. From Fig. 4.2(a), it is possible to draw the output of the photo current at 60 GHz normalized to the output photo current with 2.8 V DC reversed bias as a function of reversed bias voltage, which is proportional to the responsivity of the PD. The responsivity of the PD, which is normalized to the responsivity of PD at 2.8 V reversed bias voltage is shown in Fig.4.2 (b).

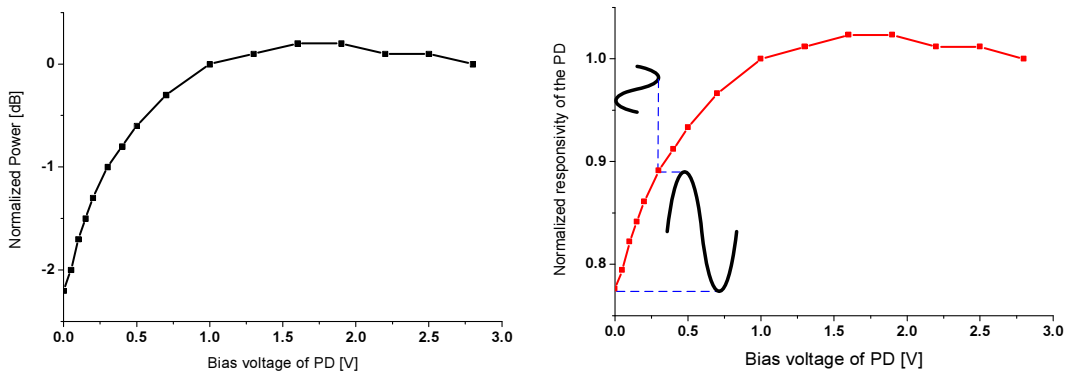

(a) normalized output power of the 60 GHz signal (b) Normalized responsivity of the PD at 60 GHz

Fig. 4.2. Characterization of the PD

From Fig. 4.2, it can be seen that the responsivity of the photodiode is a non-linear function of the reversed bias voltage. Consequently, the output of the PD contains the mixing products between the RF signal generated from photodetection and the LO_2 signal applied to the PD electrical port (Fig. 4.1).

Fig. 4.3 shows the RF output signal as a function of reversed bias voltage with different optical power input.

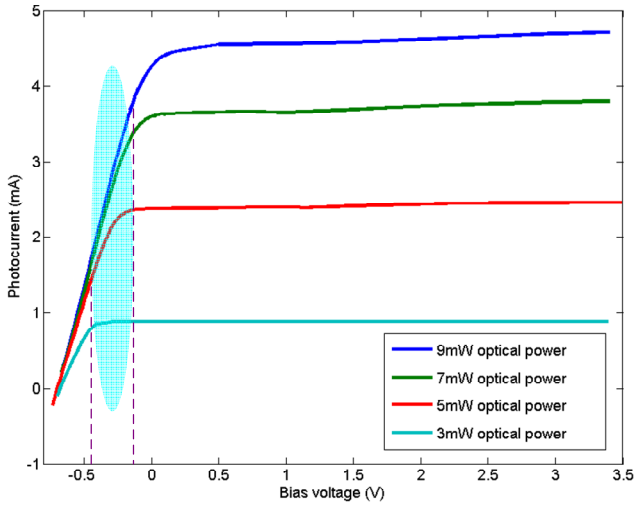

Fig. 4.3. Output of the DC photocurrent as a function of bias voltage with different optical power

From Fig. 4.3, it can be seen that, the PD works in nonlinear regime when the reversed bias voltage is lower than 0 V. Furthermore, when the bias voltage is positive, the output responsivity does not depend on the optical power (except when the device reach saturation), since the PD works as classical diode in the positive bias. In this case, there will be no photonic mixing products, since the photocurrent does not depend on the input optical signal. Here we need to mention that the PD characterized in Fig. 4.3 is not the same as the one characterized in Fig. 4.2.

Non-linearity of the PD response is convenient to evaluate by the use of the nonlinearity parameter A, which is defined as [2]:

$$A = \eta_{PD}(V_{PD}) \frac{d\eta_{PD}(V_{PD})}{dV_{PD}} \tag{4.1}$$

where $\eta_{PD}(V_{PD})$ is the responsivity of the photodiode depending on the reverse bias voltage applied to the PD (V_{PD}).

A theoretical model of the PD has also been developed for further understanding of optoelectronic mixing [4-6], but it is out of the scope of the presented work. Here we only give a conclusion: in order to obtain an efficient opto-electronic mixing, it is necessary to have high photodiode responsivity and large voltage derivative of the

responsivity, which corresponds to the bias voltage range indicated in Fig. 4.3.

4.2.2 Bidirectional RoF system setup

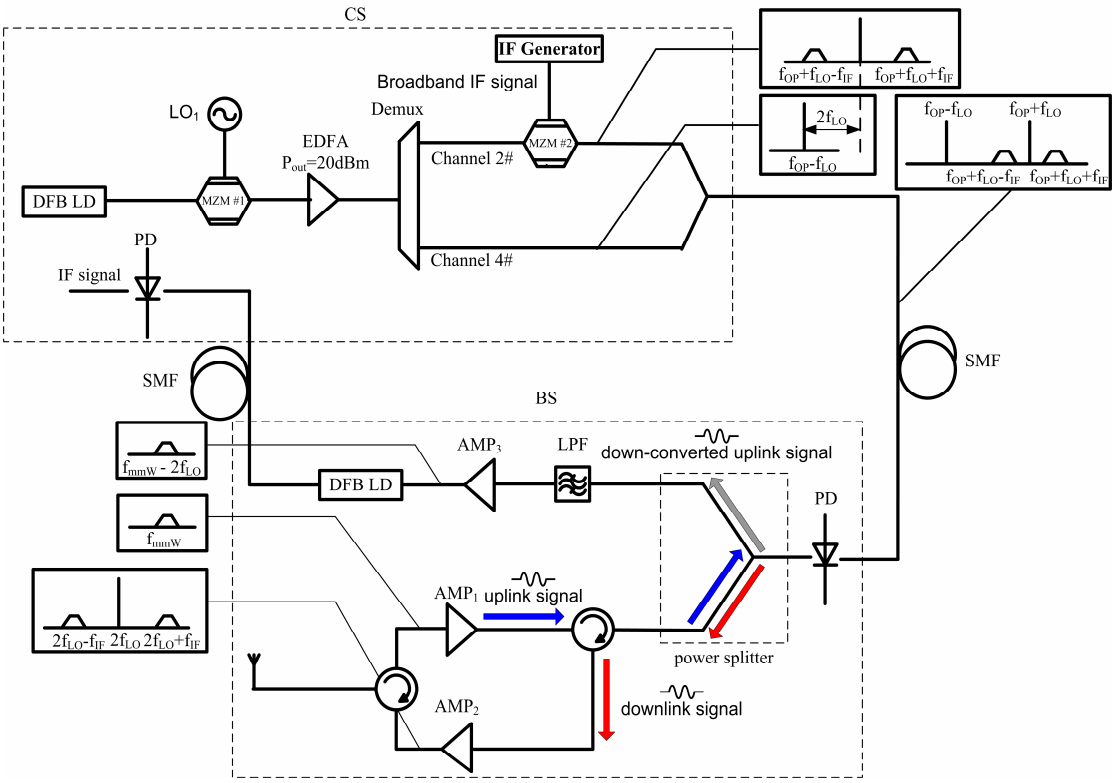

Fig. 4.4. Schematic of the bidirectional RoF system

Fig. 4.4 shows the proposed bidirectional RoF system using the photonic mixing technique for frequency down-conversion in the BS. In the central station (CS), a single mode distributed feedback (DFB) laser diode (LD) is used to generate a CW optical signal. A Mach Zehnder Modulator (MZM #1), biased at minimum of transmission and driven by a CW signal at 26.9 GHz, is employed to generate two spectral lines with a frequency interval of 52.8 GHz. MZM#1 output optical signal is then amplified using an erbium doped fiber amplifier (EDFA). To select the two mmW spaced optical spectral lines, the amplified optical signal is sent into a four-channel wavelength demultiplexer (DEMUX) with a channel spacing of 25 GHz. The optical field in channel #2 is modulated with a broadband intermediated frequency (IF) signal by using a second MZM (MZM#2 on Fig. 4.4). MZM#2 optical output is combined to the CW optical signal in channel #4 output using a 3 dB optical

coupler. The downlink optical signal is transmitted over single mode fiber (SMF) to the BS.

In the BS, a 70 GHz bandwidth p-i-n PD biased in non-linear regime is used either for photodetection process (down-link) or for mmW frequency down-conversion process (up-link).

The optically generated downlink signal includes three component: the broadband signal at $2f_{LO} + f_{IF}$ delivering the downlink data stream, the CW signal at $2f_{LO}$ for uplink down-conversion, the undesired broadband signal at $2f_{LO} - f_{IF}$ which can be easily discarded by using an electrical filter. An electrical power divider is applied to separate the down-converted uplink signal at IF band and the uplink/downlink signals at mmW band. In the case of downlink, the broadband mmW generated by optical heterodyning technique passes the mmW port of the electrical power divider. An electrical circulator is employed to separate the uplink and downlink signals. The downlink signal is amplified by an electrical amplifier (AMP_2) and radio transmitted to the user by the antenna.

The uplink signal at f_{mmW} received by the antenna is firstly amplified by AMP_1 and applied to the PD after the power splitter. The uplink signal is mixed with the optically generated CW signal at $2f_{LO}$ for down-conversion. We insist on the fact this optoelectronic mixing takes benefit of remote LO delivery from the optical heterodyning system presented in chapters 2 and 3. The down-converted signal at $f_{mmW} - 2f_{LO}$ (which corresponds to a few gigahertz typically) is transmitted to the second port of the power splitter. A low pass filter in IF band is employed to discard all the mmW components from the uplink and optical mmW generation. The pure down-converted signal at $f_{mmW} - 2f_{LO}$ is amplified by an electrical amplifier (AMP_3) and directly modulates the DFB LD. The optical signal carrying the uplink IF signal is transmitted by another optical link to the CS. The IF band uplink signal is recovered by the photodetection with a 10 GHz bandwidth PD. This bidirectional approach is compliant with the choice of medium access control (MAC) protocol for ECMA 387 standard which will be based on carrier sense multiple access (CSMA) half-duplex systems using Time Division Duplexing (TDD) [3].

4.3 Experiment for uplink transmission

4.3.1 Experimental setup

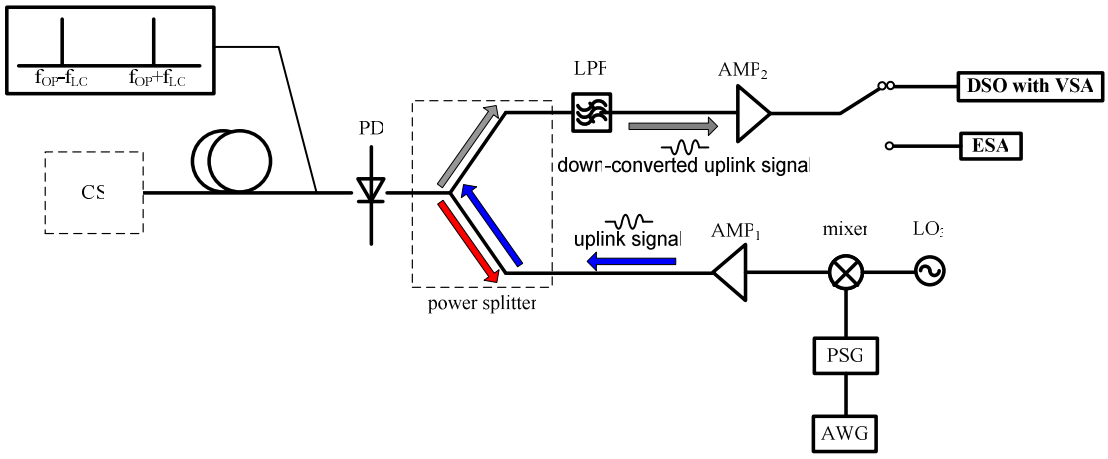

Fig. 4.5. Experimental setup for the uplink transmission

Fig. 4.5 shows the experimental setup for the uplink. The CS delivers a remote CW signal at $2f_{LO}$ =53.82 GHz to the BS for the photonic mixing. A BPSK IF signal at f_{IF} = 8.5 GHz with the data rate of 397 Mbps or 794 Mbps, which corresponds to the ECMA 387 standard data rates, is generated by the PSG and mixed with a LO signal at f_{LO3} = 66.82 GHz. As a result, the mixed signal includes three components: the desired broadband signal at f_{LO3} - f_{IF} =58.32 GHz performing as the uplink signal, the undesired CW signal at f_{LO3} =*66.82 GHz* and the undesired BPSK signal at f_{LO3} + f_{IF} =75.32 GHz are discarded by using a waveguide filter.

The uplink signal is sent into the PD, which is biased in non-linear regime, and is mixed with the CW signal at $2f_{LO.}$ A low pass filter is employed to discard the undesired down-converted component at f_{LO3} - $2f_{LO}$ =15 GHz. The desired down-converted uplink signal at f_{LO3} + f_{IF} - $2f_{LO}$ = 4.5 GHz is amplified by the electrical amplifier (AMP_2) with the gain of 40 dB and either digitalized by the DSO for demodulation or applied to the ESA.

Fig. 4.6 shows the spectrum of the uplink signal analyzed by Agilent N9030 PXA signal analyzer with the external waveguide harmonic mixer M1970V option 002. Fig. 4.6 (a) shows the spectrum from 56.82 GHz to 76.82 GHz. The data rate of the uplink signal is set to 100 Mbps, since the ESA only supports narrow band accurate

spectrum analysis (<340 MHz). It can be seen a lot of harmonic mixing products due to the external harmonic mixer Agilent N9030 PXA used for analysis. Fig. 4.6 (b) shows the accurate spectrum of the uplink signal at 58.32 GHz with 100 Mbps BPSK modulation.

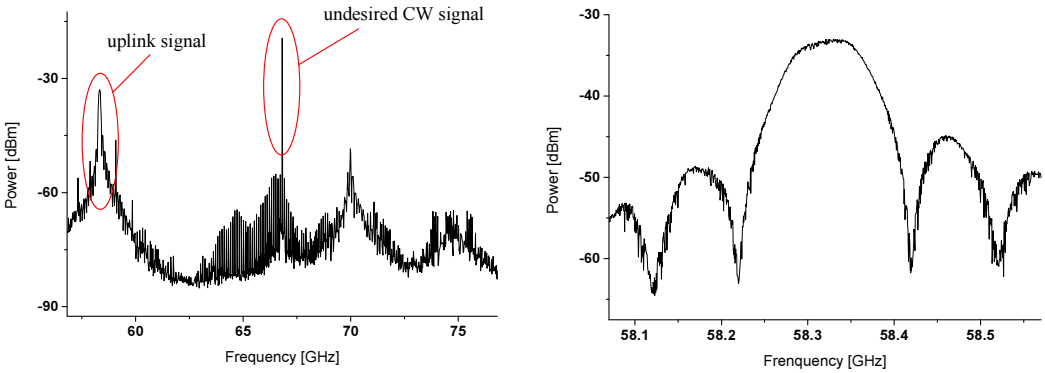

(a) Spectrum from 56.82 GHz to 76.82 GHz (b) Accurate spectrum of the uplink signal

Fig. 4.6. Spectrums of the 100Mbps uplink signal in mmW band

From Fig. 4.6 (a), it is obvious that the undesired signal at $f_{LO3} + f_{IF} = 75.32GHz$ is efficiently discarded by the waveguide filter. However the undesired CW signal and the desired broadband signal are sent into the PD.

4.3.2 Experimental down-conversion results

Fig. 4.7 shows the constellation diagrams of the down-converted BPSK signal for the uplink with the data rate of 397 Mbps and 794 Mbps respectively.

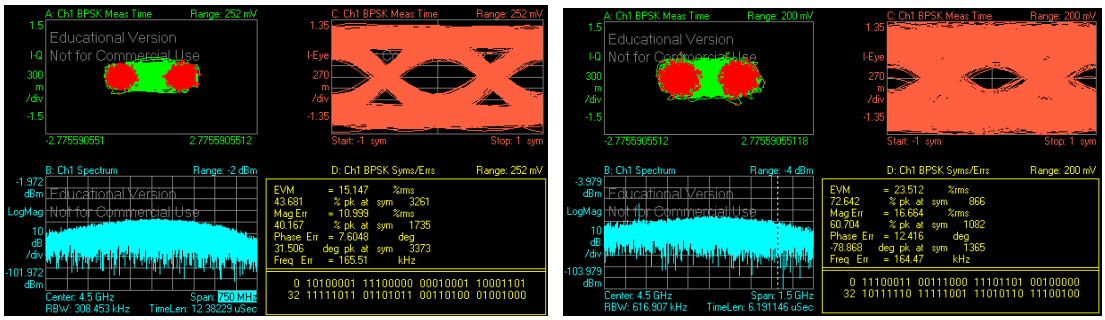

(a) Constellation of the 397 Mbps uplink signal (b) Constellation of the 794 Mbps uplink signal

Fig. 4.7. Constellation diagrams of the uplink signals

The photonic down-conversion of the signals with the EVM as low as 15.1% for 397 Mbps BPSK signal and 23.5% for 794 Mbps BPSK signal are demonstrated and are compliant with the ECMA 387 standard. Since the optical LO signal, digital

uplink signal and CW uplink signal are mixed with each other due to optoelectronic mixing, many intermodulation products are generated in the low frequency band. In practical, it is necessary to use a band pass filter to extract the desired down-converted signal. Due to the lack of this component in our laboratory, a high-pass filter is employed to discard the intermodulation products in low frequency band. We setup the uplink carrier at 58.62 GHz, and optical LO at 53.02 GHz to make all the parasitic intermodulation products out of the bandwidth of the high-pass filter. In this case, the EVM as a function of PD bias voltage and the down-converted signal power after the amplifier as a function of the bias voltage of the PD are measured and reported in Fig. 4.8.

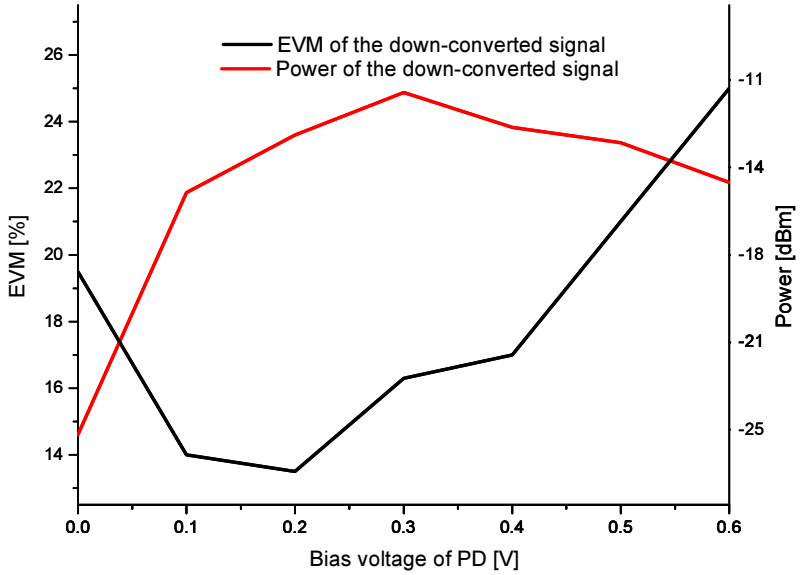

Fig. 4.8 Results for the measured mixing power and EVM after frequency down-conversion as a function of the PD bias voltage for a BPSK data rate of 397 Mbps

From Fig. 4.8, it can be seen that mixing power reaches a maximum for V_{PD}=0.3 V, whereas an optimal EVM for the mixing signal is obtained at V_{PD}=0.15 V. We remark that this optimal bias corresponds to the non linear regime of the PD and is not the typical bias used for classical photodetection.

Due to the presence of EDFA in the down link transmission, dominant noises at photodetection have been identified to be amplified spontaneous emission (ASE) / signal beating noise and additive noise from DSO, which power spectral densities

expressed in current ($\sigma^2_{ASE/Signal}$ and σ^2_{DSO} respectively) are given by [7]:

$$\sigma^2_{ASE/Sign} = 4\eta^2_{PD} N_{ASE} P_{PD} \tag{4.2}$$

$$\sigma^2_{DSO} = \frac{4kT}{R_0} \tag{4.3}$$

where N_{ASE} is the ASE power spectral density, η_{PD} is the responsivity of the PD, P_{PD} is the optical power at the PD input, k is the Boltzmann constant, T is the DSO equivalent noise temperature, R_0 is the DSO input resistor.

Fig. 4.2 (a) shows the measured normalized η^2_{PD} (in dB) as a function of V_{PD}. As it can be seen from (4.2), when PD bias decreases,$\sigma^2_{ASE/Signal}$ is a function of the square of photodiode responsivity (η^2_{PD}) which depends on photodiode bias. The power of the down-converted signal by optoelectronic mixing process follows the of A parameter defined in equation (4.1) [2].

As a consequence, the SNR evolution as a function of V_{PD} will not follow the mixing power P_{mix} evolution. This assumption is verified on Fig. 4.8, since it can be seen that PD bias for which mixing power is maximum does not correspond to the PD bias for which EVM is minimum.

Theoretical investigations have been carried out at IMEP-LAHC [8] and have shown that measured EVM can be retrieved from noise expressions (4.2) and (4.3) taking into account the change of PD responsivity as a function of the PD bias. A theoretical model of the PD has also been developed for further understanding of optoelectronic mixing, but it is out of the scope of the presented work.

4.4 Experiment for downlink transmission

Optoelectronic mixing based on the use of a p-i-n photodiode requires to bias the PD in non-linear regime. In order to use a single photodiode to provide photodetection and mixing capabilities for down-link and up-link respectively, it is necessary to quantify the impact of the non-linear PD on our optical heterodyning down-link system.

4.4.1 Experimental setup

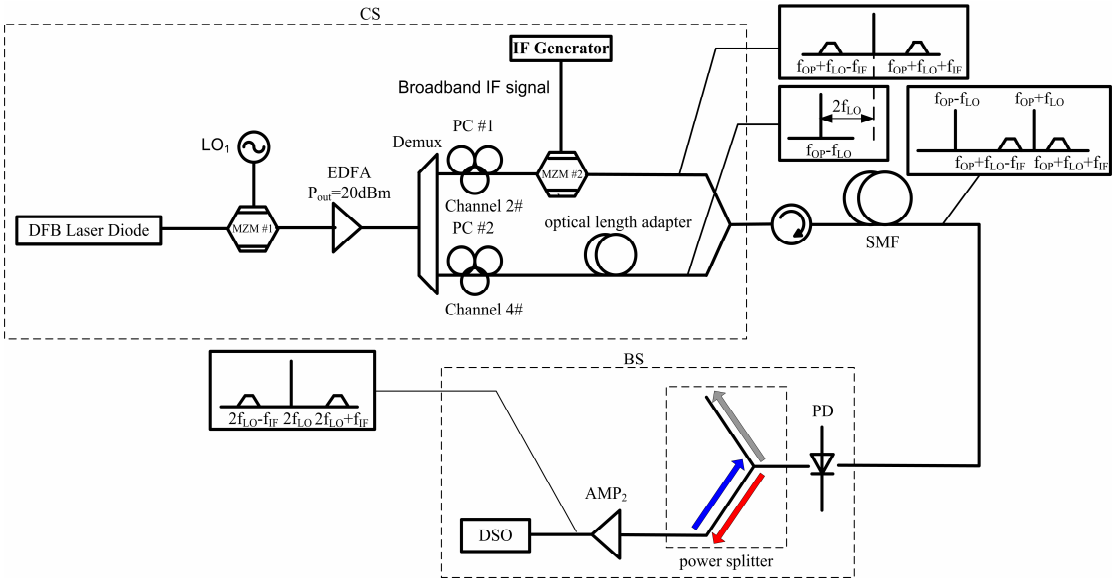

Fig. 4.9. Experimental setup for the downlink transmission

Fig. 4.9 shows the experimental setup of the downlink transmission. The experimental setup used for the down-link study is presented in the chapter 2 and chapter 3. In the BS, mmW BPSK is generated at frequency $f_{mmW} = 2f_1 + f_2$=58.32 GHz by the beating of the optical spectral lines on the PD. Two main other spectral lines at frequencies $f_{lower} = 2f_1 - f_2 = 49.28\ GHz$ and $2f_1 = 53.8$ GHz are also photodetected. PD output signal is coupled to the mmW combiner of which the one output port is connected to mmW amplifier (AMP_2) for the down-link transmission. The optically generated mmW signal is down-converted to 2 GHz band by using an electrical mixer, which is driven by a CW signal at 60.32 GHz from LO_2. The down-converted optical mmW is digitalized by the DSO and demodulated by the Vector Signal Analyzer software (VSA) from Agilent.

4.4.2 Experimental results

Fig. 4.10 shows the constellation diagrams of the downlink signal. 397 Mbps, 794 Mbps and 1588 Mbps BPSK signals with the EVM of 7%, 8.3% and 14% are generated by the PD which is biased in non-linear regime. The EVM are compliant with the ECMA 387 standard except for the 1588 Mbps BPSK signal.

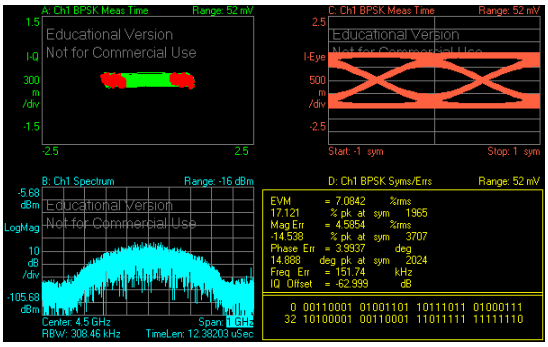

(a) 397 Mbps BPSK

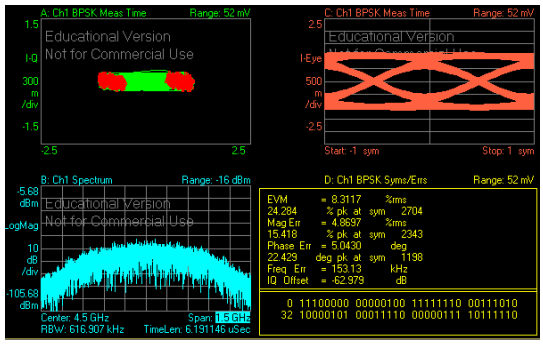

(b) 794 Mbps BPSK

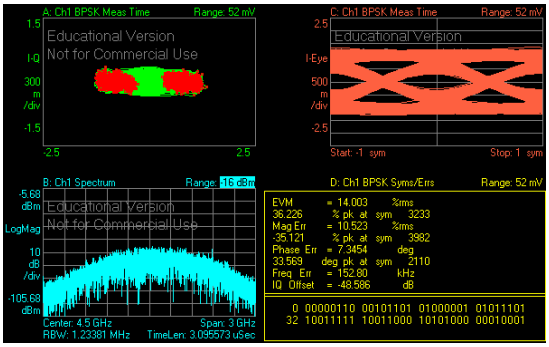

(c) 1588 Mbps BPSK

Fig. 4.10. Constellation diagrams for the downlink transmission

Since the PD is biased in non-linear regime, the responsivity of the PD is reduced as it is shown in Fig. 4.2. It is necessary to investigate on the EVM and signal power as a function of the bias voltage. Fig. 4.11 shows the EVMs of 397 Mbps and 794 Mbps BPSK signals as a function of the bias voltage of PD. The signal power as a function of PD bias voltage is also reported in Fig. 4.11.

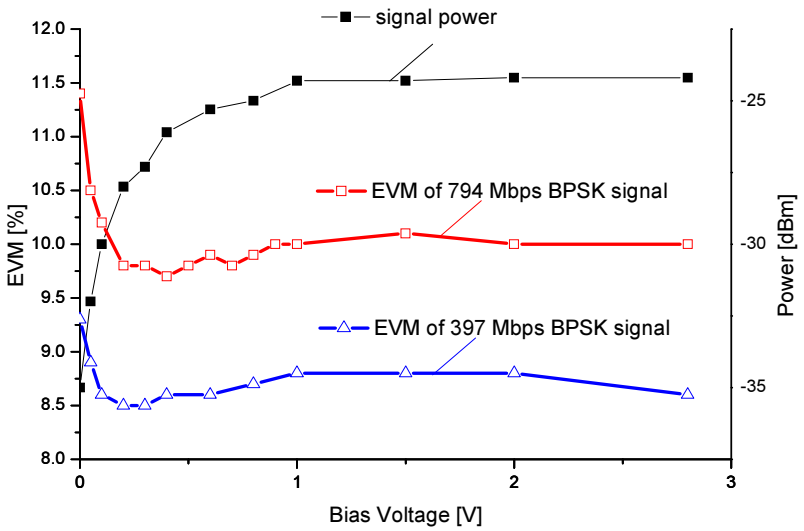

Fig. 4.11. Down-link experimental results for the mixing power and EVM for the generated mmW BPSK at data rates 397 Mbps and 794 Mbps

For V_{PD} higher than 1 V, P_{mmW} remains independent of V_{PD} because the PD works in linear regime. As seen on Fig. 4.11, for V_{PD} from 1 V to 0 V, P_{mmW} decreases due to the decrease of the PD responsivity. P_{mmW} can be expressed as:

$$P_{mmW} = \eta_{PD}^2 m^2 IL_{comb} G_{mmW} P_{PD}^2 \quad (4.4)$$

where IL_{comb} is the insertion loss of the electrical combiner, which is -7 dB, G_{mmW} is the gain of the electrical amplifier, m is the intensity modulation index.

Referring to (4.2), (4.3) and (4.4), we can infer that PD output SNR remains constant as regards V_{PD} when $\sigma^2_{ASE/Signal}$ is dominant over σ^2_{DSO} (for V_{PD}>0.15 V) and decreases when σ^2_{DSO} is the dominant noise (for V_{PD}<0.15 V). EVM being related to the inverse of SNR, this analysis is compliant with the measured EVM results reported on Fig. 4.11. For PD reverse bias voltage of 0.15 V, found to be the optimal bias for the up-link, there is no penalty on the down-link in terms of SNR (or EVM), compared to the use of the PD in linear regime. Nevertheless, there is a penalty on the generated mmW mixing power of about 4 dB compared to the measured mmW power when the PD is used in linear regime, which could be compensated by increasing the gain of an additional mmW broadband amplifier used before radio emission, in order not to penalize the BS radio coverage.

4.5 Conclusion

A new bidirectional mmW BPSK RoF system using a non-linear PD and remote LO delivery is demonstrated. The down-link system, based on optical heterodyning, allows for high data rate mmW generation. For the up-link, an optoelectronic mixing technique, based on the use of a non-linear PD, is presented and experimentally demonstrated: the PD is fed with a mmW BPSK signal through its RF output connector and with an optical remote LO which is delivered by the down-link. Optimal PD bias conditions have been discussed regarding mixing power and noise contributions to optimize SNR. Despite large mixing conversion loss for frequency down-conversion process, EVM remains in the limit of ECMA 387 standard for data rates up to 794 Mbps. For the down-link system, no penalty on SNR has been observed for the generated mmW

BPSK, but a slight decrease of mmW power of 4 dB has been measured compared to the use of the PD in linear regime. This approach uses COTS photodiode without bias switching between up-link and down-link operating modes. Moreover, the PD mixing technique, coupled to an heterodyning down-link scheme, provides the possibility to eliminate broadband electrical frequency mixers and local oscillators in BSs. Then, it is expected to reduce the complexity and cost of bidirectional mmW RoF base stations.

References of chapter 4

[1] T. Shao, *et al.*, "Photonic generation and radio transmission of ECMA 387 signal at 60 GHz using WDM demultiplexer," *Microwave and Optical Technology Letters,* vol. 54, pp. 275-277, 2012.

[2] F. Paresys, *et al.*, "Low cost bidirectionnal QPSK transmission with optical frequency conversion," in *Microwave Photonics, 2009. MWP '09. International Topical Meeting on*, 2009, pp. 1-4.

[3] ECMA387. http://www.ecma-international.org/publications/standards/Ecma-387.htm.

[4] J. Dawidczyk, "Modeling of a nonlinear PIN photodiode responsivity for studying an optical-microwave mixing process - art. no. 61592E," in *Photonics Applications in Astronomy, Communications, Industry, and High-Energy Physics Experiments IV*. vol. 6159, ed Bellingham: Spie-Int Soc Optical Engineering, 2006, pp. E1592-E1592.

[5] S. A. Malyshev and A. L. Chizh, "p-i-n Photodiodes for Frequency Mixing in Radio-Over-Fiber Systems," *Lightwave Technology, Journal of,* vol. 25, pp. 3236-3243, 2007.

[6] J. K. Piotrowski, *et al.*, "Investigation of InGaAs p-i-n photodiode for optical-microwave mixing process," in *Microwaves and Radar, 1998. MIKON '98., 12th International Conference on*, 1998, pp. 171-175 vol.1.

[7] G. Agrawal, *Fiber Optic Communication Systems*: Wiley Intersciences, 2002.

[8] T. S. Flora Parésys, Ghislaine Maury, Yannis Le Guennec and Béatrice Cabon, "Bidirectional Millimeter Wave Radio-over-Fiber System Based on Photodiode Mixing and Optical Heterodyning," *Journal of Optical Communications and Netwroking,* vol. under review.

Conclusions and prospects

This thesis is focused on the convergence of 60 GHz RoF with WDM-PON system, which contains three topics: the investigation of RoF system using WDM Demultiplexer, the study of simultaneous transmission of baseband signal and 60 GHz mmW, and the bidirectional RoF transmission.

In this thesis, different solutions for photonic mmW generation for downlink system and opto-electronic mixing technique for uplink system have been summarized. Moreover different schematics for convergence of RoF and WDM-PON access networks are introduced. Based on the study of different typical RoF systems and converged RoF with WDM-PON access networks, several key issues of the thesis have been proposed and deeply investigated. Firstly, a RoF system using WDM Demultiplexer (DEMUX) is experimentally inquired. A complete phase noise model including optical phase to intensity noise conversion contribution and the phase noise contribution due to the electrical generators is theoretically built up and experimentally demonstrated. Secondly, solutions for converged RoF and WDM-PON access networks are proposed and experimentally investigated. A novel multi-band modulation with parallel phase modulations by a single MZM is applied in the proposed converged RoF and WDM-PON system. Thirdly, bidirectional RoF based on opto-electronic mixing technique, which is compliant with WDM-PON architecture is experimentally demonstrated. The main achievements in the Ph.D thesis can be concluded as follows.

Firstly, a RoF system using WDM DEMUX is proposed and experimentally demonstrated. The RoF system, which is compliant with WDM-PON architecture, can support different standards. 1588Mbps BPSK signal at 58.32 GHz following ECMA 387 standard is generated by the RoF system. A complete phase noise model including optical phase to intensity noise conversion contribution induced by the different optical lengths of different WDM channels and the phase noise contribution due to the

electrical generators is theoretically built up and experimentally demonstrated. Under the condition of equal optical path, a very low mmW phase noise has been measured. Based on the phase noise model, the EVM value as a function of optical time delay due to path difference over coherence time of the optical source (τ_d/τ_{cOP}) is deduced and experiementally demonstrated. Moreover the law of maximum allowed optical path difference is obtained, which would be one key point of WDM DEMUX application on optical mmW generation.

Secondly, we deeply studied the convergence of RoF and WDM-PON access networks. A simple combination of RoF and WDM-PON is proposed. The digital modulations for mmW and baseband signal are implemented by two different optical modulators in two WDM channels. 58.32 GHz 1588 Mbps BPSK signal compliant with ECMA 387 standard and 10 Gbps baseband signal are simultaneously transmitted in the system. To lower the cost of the infrastructure, a novel multi-band modulation with parallel phase modulation technique by a single MZM is proposed. The digital modulations for mmW generation and baseband transmission are implemented by a single MZM. 2.5 Gbps baseband signal and 1588 Mbps BPSK mmW compliant with ECMA 387 standard are simultaneously transmitted by the converged RoF with WDM-PON access networks using parallel phase modulation by a single MZM technique. Moreover the interference between multi-band modulations has been theoretically investigated and experimentally demonstrated. It has been proved that the baseband modulation brings no impact to the mmW generation and the intermediated frequency (IF) modulation for mmW generation brings impact to the baseband signal. The impact factor has been deduced and experimentally demonstrated. Furthermore, different multi-band modulation techniques have been compared based on the theoretical investigation, which shows significant advantage of parallel phase modulation with a single MZM. From the impact factor of the IF modulation to the baseband signal, it can be seen that the IF impact to the baseband signal does not only depend on the power of the IF signal, but also depend on the peak to average power ratio of the IF modulation format. We further concentrated the IF impacts to the baseband signal induced by different IF modulation formats by using

parallel phase modulation with a single MZM. It has been shown that IF impacts to the baseband signal due to typical IF modulation, such as PSK, 16-QAM, are not radical to destroy the error free baseband transmission. However, the IF impact due to high PAPR modulation format as orthogonal frequency division multiplexing (OFDM) signal can significantly degrade the baseband signal transmission. A rule for a low impact of RF modulation to insure the error free baseband transmission is made based on the theoretical model of bit error rate (BER) of baseband signal as a function of PAPR of IF modulation. This is a remarkable achievement for the application of multi-band modulation technique in convergence RoF and WDM-PON access networks.

Thirdly, a bidirectional RoF system, which is compliant with the WDM-PON, is implemented by using optoelectronic mixing technique for the down-conversion in up-link transmission. The principle of optoelectronic mixing technique is presented, it is based on the use of a PD biased in non-linear regime. The uplink RoF system by using optoelectronic mixing technique with p-i-n photodiode for mmW down-conversion is experimentally demonstrated. 397 Mbps and 794 Mbps BPSK 60 GHz uplink signal is down-converted to IF band with the EVM in the range of ECMA 387 standard requirement. The down-link system using typical optical heterodyning scheme for mmW generation with the impact of the non-linear PD is experimentally demonstrated in this chapter. It has been proved that there is no penalty on SNR for the downlink transmission and the generated mmW BPSK, but a slight decrease of mmW power of 4 dB has been measured compared to the use of the PD in linear regime.

Although the converged RoF and WDM-PON system using multiband modulation technique and the bidirectional RoF system using optoelectronic mixing technique have been demonstrated, the bidirectional WDM-RoF system using multiband modulation technique and optoelectronic mixing technique would be a possible extension of the PhD work. Furthermore, in the thesis, only point-to-point transmission is considered. However the WDM-PON architecture should support multiple users. The cross talk between different optical channels could be another important topic to be investigated for practical implementation of converged mmW

and WDM-PON network infrastructures.

Résumé en Français

Récemment, la convergence des techniques radio à 60 GHz sur fibre optique (radio over fiber - RoF) et des réseaux d'accès optiques passifs à multiplexage en longueurs d'ondes (wavelength division multiplexing-WDM) a suscité un très grand intérêt dans la communauté scientifique. En effet, cette convergence permet simultanément de générer un signal large bande à 60 GHz et de réaliser la transmission par fibre d'un signal à plusieurs gigabits par seconde.

L'objectif de cette thèse est d'étudier les solutions pour faire converger les systèmes RoF à 60 GHZ et les réseaux passifs optiques (passive optical network – PON) utilisant le WDM, appelés dans la suite PON-WDM.

Le premier chapitre décrit le contexte des réseaux PON-WDM et les principales technologies utilisées dans les systèmes RoF : l'architecture typique des PON-WDM, les différentes techniques possibles pour générer des signaux millimétriques, les spécificités de la transmission d'un signal à 60 GHz ainsi que les solutions classiques proposées dans la littérature pour réaliser la convergence des systèmes RoF et PON-WDM. Ce chapitre pointe les différents problèmes à étudier pour mettre en place des réseaux RoF basés sur l'infrastructure PON-WDM.

Le deuxième chapitre traite d'un système RoF à 60 GHZ particulier, utilisant un démultiplexeur WDM. L'étude complète du bruit de phase, à la fois théorique et expérimentale, est effectuée : elle inclut la conversion du bruit de phase optique en bruit d'intensité, ainsi que les contributions en bruit de phase des générateurs de signaux électriques. Pour finir, la conversion optique d'un signal numérique large bande respectant le standard ECMA 387 vers les fréquences hautes millimétriques est démontrée expérimentalement.

Le troisième chapitre présente le système que nous proposons pour faire converger un système RoF et un réseau PON-WDM. Ce système permet de réaliser la génération d'un signal numérique large bande ainsi que la transmission par fibre

optique d'un signal à plusieurs gigabits par seconde. La technique de modulation multi-bandes (bande de base et bande RF) utilisant la modulation de phase sur les deux bras d'un unique modulateur de Mach-Zehnder, appelée 'modulation de phase parallèle' est analysée de manière approfondie. Elle permet notamment de diminuer le coût de l'infrastructure du réseau global. Nous avons comparé les différentes techniques de modulation multi-bandes théoriquement. De plus, dans le cas d'utilisation de l'unique modulateur de Mach-Zehnder, nous avons étudié, à la fois théoriquement et expérimentalement, l'interférence des différentes modulations multi-bandes entre elles (effet des signaux en bande de base sur les signaux millimétriques et inversement).

Dans le dernier chapitre, un démonstrateur d'un système RoF bidirectionnel, compatible avec les exigences des réseaux PON-WDM, est présenté. Ce démonstrateur utilise la technique de mélange optoélectronique pour réaliser la conversion basse de fréquence d'un signal millimétrique dans la liaison montante. La faisabilité du mélange optoélectronique permettant cette conversion basse de fréquence, basé sur l'utilisation d'une photodiode p-i-n en régime non linéaire, est prouvée expérimentalement. La liaison descendante utilise le schéma classique d'un système de génération d'un signal millimétrique fondé sur l'hétérodynage optique. L'impact du régime de fonctionnement non linéaire de la photodiode sur les performances de la liaison descendante est étudié à la fin du chapitre.

Les résultats principaux de cette thèse axée sur la technologie des systèmes RoF et l'intégration des systèmes RoF avec les réseaux d'accès PON-WDM sont les suivants :

- Un système RoF utilisant un démultiplexeur WDM, compatible avec les réseaux d'accès PON-WDM, est proposé dans cette thèse.
- Nous avons mené une étude théorique complète du bruit de phase. Elle inclut la contribution des bruits de phase des générateurs de signaux électriques et celle de la conversion de bruit de phase optique en bruit d'intensité. Cette dernière conversion est due à la détection de deux signaux cohérents, retardés l'un par

rapport à l'autre si les longueurs optiques entre les deux canaux optiques se recombinant sont différentes.

- ✓ La densité spectrale de puissance du signal millimétrique généré optiquement est analysée théoriquement et démontrée expérimentalement. Son étude donne une méthode pour compenser un éventuel délai optique $|\tau_d|$.
- ✓ L'amplitude du vecteur d'erreur (error vector magnitude –EVM) est théoriquement calculée et expérimentalement démontrée, en fonction du rapport $|\tau_d|/\tau_{cOP}$ où τ_{cOP} est la durée de cohérence de la source optique utilisée. Cela donne une règle de conception pour insérer le démultiplexeur optique dans le système d'hétérodynage optique.

- Nous avons validé expérimentalement la technique d'hétérodynage optique qui utilise un démultiplexeur pour générer un signal millimétrique respectant le standard ECMA 387.
- Nous avons proposé un système combinant une partie RoF et un réseau PON-WDM, permettant la génération simultanée d'un signal millimétrique respectant le standard ECMA 387 et la transmission d'un signal en bande de base à plusieurs gigabits par seconde. Nous avons réalisé expérimentalement avec succès la transmission simultanée d'un signal à 60 GHZ, modulé avec une modulation BPSK par un signal à 1588 Mbit/s et celle d'un signal en bande de base à 10 Gbit/s.
- Nous avons proposé une nouvelle architecture de réseaux d'accès PON-WDM et RoF qui permet de diminuer le coût global de l'infrastructure, grâce à la technique de modulation multi-bandes.
- Nous avons proposé une nouvelle technique de modulation multi-bandes : la modulation de phase parallèle utilisant un unique modulateur de Mach-Zehnder. Cette technique présente des avantages significatifs comparée à n'importe quelle autre technique de modulation multi-bandes.
  - ✓ Il n'y a aucun impact de la modulation en bande de base sur la génération millimétrique.
  - ✓ L'impact de la modulation RF sur la transmission en bande de base (impact dû à la non-linéarité de la modulation de phase) est limité.

- ✓ Le taux d'erreurs binaires du signal en bande de base intégrant l'effet du signal RF a été théoriquement calculé et expérimentalement validé. Cela donne des règles de conception pour la technique de modulation de phase parallèle avec un unique modulateur de Mach-Zehnder.

- Nous avons proposé une architecture et réalisé un démonstrateur d'un système bas-coût bidirectionnel pour la transmission RoF. Ce système utilise le mélange optoélectronique et la technique d'hétérodynage optique. Nous avons prouvé que :
  - ✓ Des signaux à 60 GHz modulés à 397 Mbit/s et 794 Mbit/s avec une modulation BPSK sont convertis vers la bande basse de fréquence en utilisant la technique de mélange optoélectronique : les contraintes du standard ECMA 387 sont respectées.
  - ✓ Pour la liaison descendante utilisant la technique d'hétérodynage optique, aucune pénalité sur l'EVM n'est causée par le choix du régime non linéaire de la photodiode. Seule une perte de 6 dB de puissance est engendrée, qui peut être compensée en utilisant un amplificateur à faible bruit de gain plus fort après la photodiode.

Bien que cette thèse couvre un grand nombre de problèmes concernant la convergence des systèmes RoF et PON-WDM, il y aurait deux axes à étudier pour la suite de ce travail.

- Il faudrait réaliser le système bidirectionnel complet combinant la partie RoF et PON-WDM, en utilisant la technique de modulation multi-bandes et le mélange optoélectronique.
- Dans cette thèse, nous nous sommes intéressés uniquement à la transmission point à point dans les systèmes RoF-PON-WDM. Or, ces systèmes sont censés supporter plusieurs utilisateurs. La prise en compte d'utilisateurs multiples est une extension importante de ce travail. Il y a principalement deux problèmes à considérer :
  - ✓ la non-linéarité de la fibre optique, due à la forte puissance injectée dans un seul lien optique par de multiples émetteurs,

- ✓ le bilan de liaison du système RoF-PON-WDM, qui est aussi relié à la non-linéarité de la fibre optique et à l'optimisation de la distribution de puissance optique entre les différents canaux optiques.

List of personal publications

International journal papers:

- **Tong Shao**, Flora Paresys, Yannis Le Guennec, Ghislaine Maury, Nicolas Carrao, and Beatrice Cabon, *Photonic Generation and Radio Transmission of ECMA 387 Signal at 60 GHz using WDM Demultiplexer*, Microwave and Optical Technology Letters, vol. 54, Issue 2, pp. 275-277, Feb. 2012.

- **Tong Shao**, Flora Paresys, Ghislaine Maury, Yannis Le Guennec, and Beatrice Cabon, *Investigation on the Phase Noise and EVM of Digitally Modulated Millimeter Wave Signal in WDM Optical Heterodyning System*, IEEE/OSA Journal of Lightwave Technology, vol. 30, Issue 6, pp. 876-885

- **Tong Shao**, Flora Paresys, Yannis Le Guennec, Ghislaine Maury, Nicolas Corrao, and Beatrice Cabon, *Convergence of 60 GHz Radio over Fiber and WDM-PON using Parallel Phase Modulation with a single Mach-Zehnder Modulator*, IEEE/OSA Journal of Lighwave Technology, accepted

International conference paper:

- **Tong Shao**, Flora Paresys, Yannis Le Guennec, Ghislaine Maury, Nicolas Corrao, and Beatrice Cabon, *Simultaneous Transmission of Gigabit Wireline Signal and ECMA 387 mmW over Fiber Using a Single MZM in Multi-Band Modulation*, IEEE Topical Meeting on Microwave Photonics Conference (MWP2011), Oct. 18th - 21st, 2011, Singapore, pp. 149-152.

- **Tong Shao**, Flora Paresys, Yannis Le Guennec, Ghislaine Maury, Jianping Yao, and Beatrice Cabon, *Investigation of Interference between Multi-band Modulations with a single Mach-Zehnder Modulator for Simultaneous 60 GHz Wireless and Wireline Signals Transmission*, IEEE Topical Meeting on Microwave Photonics Conference (MWP2012), Sep. 11th -14th, Noordwijk, Netherland, accepted.

International journal papers under review:

- Flora Paresys, **Tong Shao**, Ghislaine Maury, Yannis Le Guennec, and Beatrice Cabon, *Bidirectional Millimeter Wave Radio over Fiber System based on Photodiode Mixing and Optical Heterodyning*, IEEE/OSA Journal of Optical Communications and Networking, under review.

Title: Study of Converged 60 GHz Radio over Fiber with WDM-PON Access Networks

Abstract： In this thesis, a RoF system using WDM Demultiplexer (DEMUX) is experimentally inquired. A complete phase noise model including optical phase to intensity noise conversion contribution and the phase noise contribution due to the electrical generators is theoretically built up and experimentally demonstrated. Moreover two solutions for converged RoF and WDM-PON access networks are proposed and experimentally investigated. Particularly, a novel multi-band modulation with parallel phase modulations by using a single Mach Zehnder modulator (MZM) is applied in the proposed converged RoF with WDM-PON access networks. The interferences between multi-band modulations with a single optical modulator are theoretically investigated and experimentally demonstrated. Finally, bidirectional RoF based on opto-electronic mixing technique, which is compliant with WDM-PON architecture, is experimentally demonstrated.

Keywords: Radio over Fiber, WDM-PON, ECMA 387, mmW, Multi-band modulation.

Titre : Etude de la Convergence de la Technologie 60 GHz Radio sur Fibre avec les Réseaux d'Accès WDM-PON

Résumé : Dans ce travail de thèse, un système radio-sur-fibre millimétrique, compatible avec les architectures de réseaux d'accès optiques passifs basés sur le multiplexage en longueur d'onde (WDM-PON) est démontré. La génération de signaux millimétriques par voie optique est réalisée expérimentalement en utilisant la technique d'auto-hétérodynage grâce à l'utilisation d'un démultiplexeur en longueur d'onde. Une étude complète sur le bruit de phase de la porteuse millimétrique, générée par voie optique, est menée. Une nouvelle technique de modulation multi-bandes (bande de base et radio), basée sur l'utilisation d'un unique modulateur électrooptique de Mach-Zehnder (MZM), est étudiée théoriquement et démontrée expérimentalement. Enfin, une transmission bi-directionnelle radio-sur-fibre à 60 GHz a été démontrée. Elle utilise le mélange optoélectronique pour le lien montant et est compatible avec l'architecture WDM-PON.

Mots clés: Radio sur Fibre, WDM-PON, ECMA 387, mmW, Modulation multi-bandes

Institut de Microélectronique Electromagnétisme et Photonique et le Laboratoire d'Hyperfréquences et de Caractérisation (IMEP-LAHC), 3, rue Parvis Louis Néel, BP 257, F38016 Grenoble Cedex 1